

MIST AND MICROSTRUCTURE CHARACTERIZATION IN END MILLING AISI 1018
STEEL USING MICROLUBRICATION

Vasim Shaikh, B.E., M.S

Dissertation Prepared for the Degree of

DOCTOR OF PHILOSOPHY

UNIVERSITY OF NORTH TEXAS

August 2013

APPROVED:

Nourredine Boubekri, Major Professor
Thomas W. Scharf, Co-Major Professor
Rajarshi Banerjee, Committee Member
Peter Collins, Committee Member
Marcus Young, Committee Member
Narendra Dahotre, Chair of the Department of
Materials Science and Engineering
Costas Tsatsoulis, Dean of the College of
Engineering
Mark Wardell, Dean of the Toulouse Graduate
School

Shaikh, Vasim. Mist and microstructure characterization in end milling AISI 1018 steel using microlubrication. Doctor of Philosophy (Materials Science and Engineering), August 2013, 129 pp., 90 illustrations, references, 90 titles.

Flood cooling is primarily used to cool and lubricate the cutting tool and workpiece interface during a machining process. But the adverse health effects caused by the use of flood coolants are drawing manufacturers' attention to develop methods for controlling occupational exposure to cutting fluids. Microlubrication serves as an alternative to flood cooling by reducing the volume of cutting fluid used in the machining process. Microlubrication minimizes the exposure of metal working fluids to the machining operators leading to an economical, safer and healthy workplace environment. In this dissertation, a vegetable based lubricant is used to conduct mist, microstructure and wear analyses during end milling AISI 1018 steel using microlubrication. A two-flute solid carbide cutting tool was used with varying cutting speed and feed rate levels with a constant depth of cut. A full factorial experiment with Multivariate Analysis of Variance (MANOVA) was conducted and regression models were generated along with parameter optimization for the flank wear, aerosol mass concentration and the aerosol particle size. MANOVA indicated that the speed and feed variables main effects are significant, but the interaction of (speed*feed) was not significant at 95% confidence level. The model was able to predict 69.44%, 68.06% and 42.90% of the variation in the data for both the flank wear side 1 and 2 and aerosol mass concentration, respectively. An adequate signal-to-noise precision ratio more than 4 was obtained for the models, indicating adequate signal to use the model as a predictor for both the flank wear sides and aerosol mass concentration. The highest average mass concentration of 8.32 mg/m^3 was realized using cutting speed of 80 Surface feet per minute (SFM) and a feed rate of 0.003 Inches per tooth (IPT). The lowest average mass concentration of

5.91 mg/m³ was realized using treatment 120 SFM and 0.005 IPT. The cutting performance under microlubrication is five times better in terms of tool life and two times better in terms of materials removal volume under low cutting speed and feed rate combination as compared to high cutting speed and feed rate combination. Abrasion was the dominant wear mechanism for all the cutting tools under consideration. Other than abrasion, sliding adhesive wear of the workpiece materials was also observed. The scanning electron microscope investigation of the used cutting tools revealed micro-fatigue cracks, welded micro-chips and unusual built-up edges on the cutting tools flank and rake side. Higher tool life was observed in the lowest cutting speed and feed rate combination. Transmission electron microscopy analysis at failure for the treatment 120 SFM and 0.005 IPT helped to quantify the dislocation densities. Electron backscatter diffraction (EBSD) identified 4 to 8 μm grain size growth on the machined surface due to residual stresses that are the driving force for the grain boundaries motion to reduce its overall energy resulting in the slight grain growth. EBSD also showed that (001) textured ferrite grains before machining exhibited randomly orientated grains after machining. The study shows that with a proper selection of the cutting parameters, it is possible to obtain higher tool life in end milling under microlubrication. But more scientific studies are needed to lower the mass concentration of the aerosol particles, below the recommended value of 5 mg/m³ established by Occupational Safety and Health Administration (OSHA).

Copyright 2013

by

Vasim Shaikh

ACKNOWLEDGEMENTS

I would like to express my sincere and deepest gratitude to my advisor, Dr. Nourredine Boubekri, for his invaluable guidance, support and mentorship for this study and throughout my course of study for the masters and Ph.D. program at the University of North Texas. His guidance and inspiration enabled me to successfully complete my dissertation. I feel honored to have had the opportunity to work under his supervision.

I would also like to thank my co-advisor Dr. Thomas W. Scharf, for his suggestions and mentorship without which this study would not have been possible. I am grateful for his helpfulness, cooperation and willingness to answer questions anytime.

I appreciate the kindness of Drs. Rajarshi Banerjee, Peter Collins and Marcus Young for serving on my dissertation committee. Their contributions and suggestions helped to improve this work tremendously. I thank them for giving their valuable time to guide me and review my dissertation. I would also like to appreciate the selfless and generous help of Dr. Junyeon Hwang, Dr. Hamidreza Mohseni, Jon-Erik Mogonye, Douglas Kinkenon, Peyman Samimi, David Brice and Victor Ageh. I would also like to acknowledge the Center for Advanced Research and Technology (CART) and the Manufacturing Engineering Laboratory at the University of North Texas.

I am, as ever, indebted to my parents Mrs. and Mr. Abdul Majid Shaikh for their love and support throughout my life. I would not have come this far without the understanding and support of my wife, Firoza Khan. I thank her from the bottom of my heart to help me achieve my goals.

TABLE OF CONTENTS

	Page
ACKNOWLEDGEMENTS.....	iii
LISTS OF TABLES.....	vii
LISTS OF FIGURES.....	viii
Chapters	
1. INTRODUCTION	1
Background	1
Microlubrication	4
Multivariate Analysis of Variance (MANOVA)	6
Why Use MANOVA	7
Research Objective	7
2. LITERATURE REVIEW	9
Microlubrication Drilling	9
Microlubrication Milling Other than Steel	13
Microlubrication End Milling Steel	18
Fluids not Suggested for Microlubrication	26
Why Use Vegetable Oil	26
Why Use AISI 1018 Steel	27
Summary	28
Conclusion	28
3. EXPERIMENTAL METHODS AND PROCEDURES	30
Design of Experiments	30

Cutting Tool	31
Workpiece Material	32
End milling equipment	36
Metal Working Fluid (MWF)	37
Aerosol Mass Concentration and Aerosol Particle Size Measurements ...	38
Samples Preparation	39
End Milling Procedures	40
Method of Data Analysis for MANOVA	42
MANOVA Assumptions	42
Robustness of MANOVA	43
Hypotheses	44
Tool Flank Wear Measurements	44
Tool-Workpiece Interface Temperature Calculations	46
Vickers Hardness Measurement	49
Bearing Area Curve Measurement	52
Scanning Electron Microscopy (SEM) / Focused Ion Beam (FIB)	53
Electron Backscatter Diffraction (EBSD)	54
Transmission Electron Microscopy (TEM)	54
Dislocation Density Quantification Procedure	55
Assumptions of the Study	58
4. RESULTS AND ANALYSES	59
MANOVA	59
Aerosol Mass Concentration and Aerosol Particle Size Analysis	79

Tool-Workpiece Interface Temperature Analysis	80
Tool Life	85
Wear Mechanisms	87
Cross Sectional Hardness Analysis at Failure	95
Bearing Area Curve Calculations	96
TEM Analysis at Failure	100
EBSD Analysis	108
5. SUMMARY AND CONCLUSIONS	118
Recommendations for Future Work	122
REFERENCES	123

LIST OF TABLES

	Page
1. Permissible exposure limits (PELs)	3
2. Factorial experiment layout of cutting speed and feed rate combinations	30
3. Chemical composition of AISI 1018 steel	33
4. Mechanical properties of AISI 1018 steel	33
5. Mechanical properties of Accu-Lube 6000	38
6. Average and maximum flash temperature formulae for line contacts	48
7. MANOVA test summarized results	67
8. ANOVA test for flank wear side 1	68
9. ANOVA test for flank wear side 2	68
10. ANOVA test for aerosol mass concentration	68
11. ANOVA test for aerosol particle size	68
12. Temperature calculations for different cutting speed and feed rate combinations	84
13. Roughness parameter for different cutting speed and feed rate combinations	100
14. CBED data for thickness determination	104

LISTS OF FIGURES

	Page
1. External spray MQL system	5
2. Solid carbide end mill	32
3. Schematic representation of microstructures for AISI 1018 steel	34
4. SEM image of as-received AISI 1018 steel	35
5. TEM image of pearlite	35
6. Mori Seiki Dura Vertical 5060 machining center	36
7. Kuroda ecosaver KEP3 micro lubrication system	37
8. Thermo scientific DataRam4	39
9. Final sample	40
10. Mitutoyo toolmaker's microscope	45
11. Optical micrograph of tool rake side 1 - Treatment 100 SFM and 0.003 IPT	46
12. Shimadzu dynamic ultra micro hardness tester	50
13. Schematic of vickers hardness measurements	51
14. Bakelite mount	51
15. Nanovea non-contact optical profilometer	52
16. Dual beam Nova 200 NanoLab SEM/FIB	53
17. (a) Tecnai G2 F20 TEM	55
17. (b) Necessary measurements to extract thickness (t) from K-M fringes	56
18. Test for equal covariance for flank wear side 1	60
19. Test for equal covariance for flank wear side 2	60

20.	Test of equal covariance for aerosol mass concentration	61
21.	Test for equal covariance for aerosol particle size	61
22.	Constant variance in data for flank wear side 1	62
23.	Constant variance in data for flank wear Side 2	62
24.	Constant variance in data for aerosol mass concentration	63
25.	Constant variance in data for aerosol particle size	63
26.	Mahalanobis distance for multivariate normality testing for flank wear side 1, side 2, aerosol mass concentration and aerosol particle size	64
27.	Normal plots of residual in data for flank wear side 1	65
28.	Normal plots of residual in data for flank wear side 2	66
29.	Normal plots of residual in data for aerosol mass concentration	66
30.	Normal plots of residual in data for aerosol particle size	67
31.	Down-milling (Climb milling) and Up-milling (Conventional milling)	70
32.	Main effect plot for flank wear side 1	72
33.	Interaction plot for flank wear side 1	72
34.	Main effect plot for flank wear side 2	73
35.	Interaction plot for flank wear side 2	73
36.	Tool run-out	74
37.	Main effect plot for aerosol mass concentration	74
38.	Interaction plot for aerosol mass concentration	75
39.	Desirability plot for flank wear side 1	76
40.	Selected solution plot for flank wear side 1	76
41.	Desirability plot for flank wear side 2	77
42.	Selected solution plot for flank wear side 2	77

43.	Desirability plot for aerosol mass concentration	78
44.	Selected solution plot for aerosol mass concentration	78
45.	Average mass concentration for different cutting speeds and feed rates combinations ...	79
46.	Average particle size for different cutting speeds and feed rates combinations	80
47.	Tool life for different cutting speeds and feed rates combinations at failure	85
48.	Material removal volume for different cutting speeds and feed rates combinations at failure.....	86
49.	Optical micrograph of tool flank wear for treatment (a) 80 SFM and 0.003 IPT (b) 120 SFM and 0.003 IPT (c) 100 SFM and 0.005 IPT (d) 120 SFM and 0.005 IPT (e) 100 SFM and 0.003 IPT	87
50.	Optical micrograph of tool rake for treatment 100 SFM and 0.003 IPT	88
51.	Optical micrograph of tool rake for treatment 80 SFM and 0.005 IPT	89
52.	SEM micrograph of tool rake for treatment 120 SFM and 0.005 IPT showing sliding wear	89
53.	SEM micrograph of tool rake for treatment 120 SFM and 0.005 IPT showing non-uniform micro-abrasion (a) Rake (b) Flank	90
54.	SEM micrograph of tool flank for treatment 80 SFM and 0.003 IPT showing micro-fatigue crack	91
55.	SEM micrograph of tool for treatment 120 SFM and 0.005 IPT showing welded micro-chips (a) Rake (b) Flank	91
56.	SEM micrograph of tool rake for treatment 80 SFM and 0.003 IPT showing sliding wear	92
57.	SEM micrograph of tool for treatment 80 SFM and 0.003 IPT showing non-uniform micro-abrasion (a) Rake (b) Flank	93
58.	SEM micrograph of tool flank for treatment 80 SFM and 0.003 IPT showing adhesion .	93
59.	SEM micrograph of tool rake for treatment 80 SFM and 0.003 IPT showing adhesion and built-up edge (BUE)	94
60.	SEM micrograph of workpiece for treatment 80 SFM and 0.003 IPT showing abrasive wear through plowing mechanism	95

61.	Microhardness depth profile of cross-section for treatment 120 SFM and 0.005 IPT	96
62.	Microhardness depth profile of cross-section for treatment 80 SFM and 0.003 IPT	96
63.	Surface profile at failure for treatment 120 SFM and 0.005 IPT	97
64.	Surface profile at failure for treatment 80 SFM and 0.003 IPT	97
65.	Histogram for treatment 120 SFM and 0.005 IPT	98
66.	Histogram for treatment 80 SFM and 0.003 IPT	98
67.	Bearing area curve at failure for treatment 120 SFM and 0.005 IPT	99
68.	Bearing area curve at failure for treatment 80 SFM and 0.003 IPT	99
69.	Lift-out area 20 μ m from machined edge for treatment 120 SFM and 0.005 IPT	101
70.	TEM image showing dislocations for a depth of 20 μ m from machined edge for treatment 120 SFM and 0.005 IPT	102
71.	(a) and (b) TEM image showing dislocation pile-ups for a depth of 20 μ m from machined edge for treatment 120 SFM and 0.005 IPT	103
72.	TEM image showing fewer dislocations for a depth of 100 μ m from machined edge for treatment 120 SFM and 0.005 IPT	103
73.	Intercept plot to extrapolate foil thickness value	104
74.	(a) TEM micrograph of image 1 used to determine ρ by the line intersection method at a depth of 20 μ m from machined edge for treatment 120 SFM and 0.005 IPT	105
74.	(b) TEM micrograph of image 2 used to determine ρ by the line intersection method at a depth of 20 μ m from machined edge for treatment 120 SFM and 0.005 IPT	106
75.	Dislocation density quantification at a depth of 20 μ m from machined edge for treatment 120 SFM and 0.005 IPT	106
76.	IPF for all phases – As received material	109
77.	IPF for ferrite and iron carbide phase – As received material	109
78.	IPF for all phases – Sample 1 and 2 machined at 80 SFM and 0.003 IPT	110
79.	IPF for ferrite phase – Sample 1 and 2 machined at 80 SFM and 0.003 IPT	110

80.	IPF for iron carbide phase – Sample 1 and 2 machined at 80 SFM and 0.003 IPT	111
81.	IPF for all phases – Sample 1 and 2 machined at 120 SFM and 0.005 IPT	111
82.	IPF for ferrite phase – Sample 1 and 2 machined at 120 SFM and 0.005 IPT	112
83.	IPF for iron carbide phase – Sample 1 and 2 machined at 120 SFM and 0.005 IPT	112
84.	Grain size comparison	113
85.	Grain size distribution plot – As- received material	114
86.	Grain size distribution plot for 80 SFM and 0.003 IPT – Sample 1	115
87.	Grain size distribution plot for 120 SFM and 0.005 IPT – Sample 1	115
88.	Ferrite pole figures – As received material	116
89.	Ferrite pole figures – Sample 1 and 2 machined at 80 SFM and 0.003 IPT	117
90.	Ferrite pole figures – Sample 1 and 2 machined at 120 SFM and 0.005 IPT.....	117

CHAPTER 1

INTRODUCTION

Background

Metal cutting processes have been in practice for many centuries. The process of machining any material is very complicated. It is dependent on many important factors such as the machine tool, the machining conditions, the workpiece materials, the tool material, tool wear and metal working fluid (MWF). Among these the most important controllable factor is the MWF. MWFs are used to cool and lubricate the tool-workpiece interface during machining. MWFs perform several important functions including reducing the friction-heat generation and dissipating generated heat at the tool-workpiece interface which results in the reduction of tool wear. MWFs increase tool life and achieve faster production rates (Clarens et al. 2008). Also, MWFs flush the chips away from the tool and clean the workpiece causing less built-up-edge (BUE). The first appearance of metal cutting fluid in the literature occurred in the mid-19th century (Northcott, 1868). A more comprehensive work on cutting fluids was reported by F. W. Taylor (Taylor, 1906). Since then, metal cutting fluids or MWFs have been used during metal cutting.

The use of MWFs cannot be completely stopped because of their beneficial contributions. But, the metal cutting industry wants to find ways to reduce/eliminate the usage of MWFs; the use of MWFs in machining is thought to be undesirable for economical, health, and environmental reasons. The cost incurred on MWFs range from 7-17% of the total costs of the manufactured work piece (Weinert et al. 2004) and 16-20% of the total product cost (Sreejith & Ngoi, 2000) as compared to the tool cost which is only about 2-4% (Zhang et al. 2012). According to a survey conducted by the European Automobile Industry, the cost incurred by

lubricants comprises nearly 20% of the total manufacturing cost contrasted with the cost of the cutting tool which is only 7.5% of the total cost (Brockhoff & Walter, 1998). More than 100 million gallons of MWFs are used in the United States of America each year and approximately 1.2 million employees are exposed to them and to their potential occupational health hazards (Chalmers, 1999). According to the Federal Office of Economics, more than 78,800 tons of cutting fluids was used in Germany in the year 2002 (Heisel et al. 2009). MWFs in the form of airborne particles often remain suspended in the working environment for an extended period of time and can be inhaled by the workers causing health concerns (Sutherland et al. 2000). U.S. National Institute for Occupational Safety and Health (NIOSH) recommends that the exposure limits (RELs) to MWF aerosols cannot exceed 0.5 mg/m^3 total particulate mass as a time weighted average (TWA) concentration for up to 10 hours per day during a 40 hours work week (NIOSH, 1998) and cannot exceed 10 mg/m^3 as a 15 minutes TWA short-term exposure limit (STEL) (Park, 2012). The Occupational Safety and Health Administration (OSHA) have currently two permissible exposure limits (PELs) applied to MWFs. They are 5 mg/m^3 for an 8 hours TWA for mineral oil mist and 15 mg/m^3 for an 8 hours TWA for particulates not otherwise classified (PNOC) (Sheehan, 1999). The American Conference of Governmental Hygienists (ACGIH) threshold limit value (TLV) and Health Safety Executive, UK, occupational exposure limits (OELs) for mineral oils mist is 5 mg/m^3 for an 8 hours TWA, and 10 mg/m^3 for a 15 minutes STEL (Park, 2012). The Swiss recommendations for PELs is 0.2 mg/m^3 for heavy oil with boiling point greater than 350°C of aerosol and/or 20 mg/m^3 of oil aerosol plus vapor for medium or light oil. The German Institute of Occupational Health (BGIA) standard is 10 mg/m^3 of oil aerosol plus vapor. In France, the National Institute for Research and Safety (INRS) proposes a recommended value of 1 mg/m^3 of aerosol (Huynh et al. 2009).

Table 1: Permissible exposure limits (PELs).

Occupational Safety & Health Agencies	Concentration (mg/m³)
National Institute for Occupational Safety and Health (NIOSH) (10 hrs.-TWA)	0.5
National Institute for Occupational Safety and Health (NIOSH) (15 min-TWA)	10.0
Occupational Safety and Health Administration (OSHA) (Mineral oil) (8 hrs.-TWA)	5.0
Occupational Safety and Health Administration (OSHA) (Not specified) (8 hrs.-TWA)	15.0
American Conference of Governmental Hygienists (ACGIH) (Mineral oil) (8 hrs.-TWA)	5.0
American Conference of Governmental Hygienists (ACGIH) (Mineral oil) (15 min-TWA)	10.0
Health Safety Executive-UK (Mineral oil) – (8 hrs.-TWA)	5.0
Health Safety Executive-UK (Mineral oil) – (15 min-TWA)	10.0
Swiss (Heavy oil) – (@ 350°C)	0.2
Swiss (medium/light oil) – (@ 350°C)	20.0
German Institute of Occupational Health (BGIA)	10.0
National Institute for Research and Safety (INRS)	1.0

The oil mist level in the U.S. automotive parts manufacturing facilities has been estimated to be 20-90 mg/m³ with the use of flood coolant (Bennett & Bennett, 1985). The exposure to such amounts of MWFs may contribute to adverse health effects and safety issues, including toxicity, dermatitis, respiratory disorders and cancer (Boubekri & Shaikh, 2012). Studies among the U.S. automobile workers have also reported increased rates of laryngeal and certain digestive tract cancers in relation to MWF exposures (Greaves et al. 1997). The conventional use of MWFs produces wet chips which in turn need to be dried before recycling incurring cost. The cost related to the filtering, waste removal and the disposal of the MWFs according to the environmental regulations can be more expensive than the cost of tooling (Dhar et al. 2006). Due to these problems related to economical, health and environmental issues, microlubrication has been sought as an alternative to minimize the use of cutting fluids.

Microlubrication

Microlubrication is also known as green machining, minimum quantity lubrication (MQL), near-dry machining, semi-dry machining or spatter lubrication. Microlubrication was introduced by Horkos Corporation - Japan in 1992. Microlubrication consists of atomizing a very small quantity of MWF ranging between 2 to 200 ml/hr directed toward the cutting tool/workpiece interface in the form of an aerosol. In microlubrication technique, the MWF does not recirculate through the lubrication system. It is almost all evaporated at the point of application. Hence no recirculation is required. It is important however to ensure an efficient extraction of aerosol from the machine. In microlubrication, the lubrication is obtained via the MWF, and the cooling is achieved by pressurized air that reaches the cutting tool/workpiece interface. Investigations have shown that microlubrication is effective at reducing cutting tool/workpiece interface temperature, tool wear, thermal distortion and material adhesion to the tool. In some studies using microlubrication the performance was equivalent to or better than flood cooling (Kurgin et al. 2011).

There are two basic types of MQL systems: external spray MQL and through-tool MQL. The external spray MQL system consists of a coolant tank or reservoir which is connected with tubes fitted with one or more nozzles directed towards the tool/workpiece interface. As shown in figure 1, the system has an independent adjustable air and coolant flow control knob which helps to vary the coolant delivery.

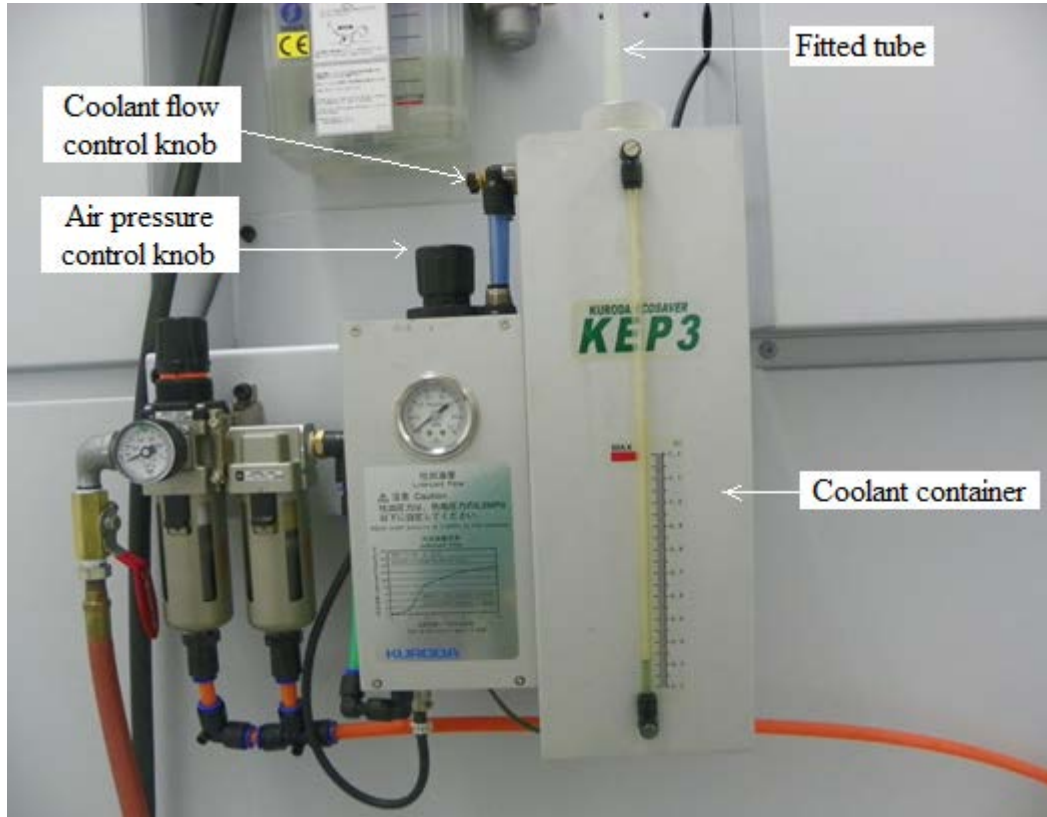


Figure 1: External spray MQL system.

There are two basic types of through-tool MQL systems, based on a method of creating an air-oil mist. The first is the external mixing or one-channel system. In this type, the oil and air are mixed externally, and piped through the spindle and tool to the cutting zone. The second technique is the internal mixing or two channel system. In this type, two parallel tubes are routed through the spindle to bring oil and air to an external mixing device near the tool holder where the mist is created (Filipovic & Stephenson, 2006).

The aerosol during microlubrication can be produced by two mechanisms: atomization and vaporization/condensation. In atomization, aerosol is produced by the disintegration of lubricant jet by the kinetic energy of the lubricant itself, by exposure to high velocity air or as a result of mechanical energy applied externally through a rotating or vibrating device (Adler et al. 2006). Vaporization is produced as a result of heat generated at the tool/workpiece interface.

This heat is transferred to the lubricant and raises its temperature above the saturation temperature resulting in boiling and vapor production at the workpiece/lubricant interface. This vapor condenses spontaneously generating aerosol/mist (Sutherland et al. 2000). In regular machining operations that use a flood coolant supply, cutting fluids have been selected mainly on the basis of their characteristics, i.e., their cutting performance.

In microlubrication however, secondary characteristics of a lubricant are important, such as their safety properties (environment pollution and human contact), biodegradability, oxidation and storage stability. This is important because the lubricant must be compatible with the environment and resistant to long term usage caused by low consumption (Wakabayashi et al. 2006). Further, microlubrication reduces induced thermal shock and helps to increase the workpiece surface integrity in situations of high tool pressure (Attanasio et al. 2006).

Multivariate Analysis of Variance (MANOVA)

MANOVA is also known as multidimensional analysis of variance (Meyveci et al. 2011) or multiple analysis of variance (Chakraborty, 2007). MANOVA is used to study the effects of one or more independent variables on more than one dependent variable/s. MANOVA is a conceptually straightforward extension of analysis of variance (ANOVA). The major distinction is that in ANOVA one evaluates mean differences on a single dependent criterion variable, whereas in MANOVA one evaluates mean differences of independent variables on two or more dependent variables simultaneously (Bray & Maxwell, 1985; Hand & Taylor, 1987). MANOVA is conducted in a two step process. The first step is to test the overall hypothesis of no differences in the means for the different groups of independent variables. If this test is significant, the second step is to conduct follow-up tests to explain the group differences if any.

Unlike ANOVA, there is not just one method (i.e. the F-test) to form a test statistics. Four different tests may be employed in MANOVA; (i) Hotelling's T-squared test (ii) Wilk's lambda (iii) Pillai-Bartlett test and (iv) Roy's greatest character root (GCR) test. The Hotelling's T-squared test is a common traditional test used to compare the mean vectors of two groups formed by the independent variables. The Wilk's lambda test is conducted when there are more than two groups formed by the independent variables. It is also one of the most common and widely used traditional tests. The sum of explained variances of the discriminant variables are given by the Pillai-Bartlett test (Bray & Maxwell, 1985).

Why Use MANOVA

Some of the reasons to use MANOVA in studies investigating mean differences are:

1. MANOVA helps us to evaluate the mean differences on all the dependent variables simultaneously, rather than looking at each of them in isolation.
2. MANOVA gives us the opportunity to learn more about the data by looking at the variables in some combination or pattern rather than looking at them individually.
3. MANOVA examines different dependent variables together, thus, it enhances the interpretation of results and provides a more powerful test than doing separate ANOVAs.

Research Objectives

The primary objective of this research is to investigate the effectiveness of microlubrication during end milling American Iron and Steel Institute (AISI) 1018 steel with a solid carbide cutter under varying cutting speed and feed rate levels and a constant depth of cut using Acculube 6000 vegetable based lubricant. A full factorial experiment and regression

models along with parameter optimization for the aerosol mass concentration, aerosol particle size and tool flank wear are generated. Microstructure and mist characterizations are done for the high cutting speed/high feed rate level and the low cutting speed/low feed rate level.

The following tasks are specifically addressed in the study:

1. Investigate the workpiece subsurface deformation.
2. Investigate the subsurface strengthening taken place due to the dislocation activities.
3. Investigate the effects of each independent variable (i.e. cutting speed and feed rate) on aerosol mass concentration, aerosol particle size and tool flank wear.
4. Develop predicting models for aerosol mass concentration, aerosol particle size and tool flank wear.
5. Investigate the correlation between all dependent variable (i.e. aerosol mass concentration, aerosol particle size and tool flank wear).
6. Estimate the cutting zone temperature for all cutting conditions.
7. Examine the wear process and mechanisms on the tool flank and cause of tool failure.
8. Examine surface texture and grain size evolution before and after machining.

CHAPTER 2

LITERATURE REVIEW

Studies in microlubrication were largely initiated in 1992 by Horkos Corporation in Japan. Since the last decade, microlubrication is realized to address issues pertaining to economical benefits, occupational hazards and environmental pollution. Several materials have been reported using microlubrication including carbon steels, alloy steels, aluminum, nodular cast iron, inconel and titanium. In microlubrication, vegetable oil or synthetic ester oil are mainly used as lubricant instead of mineral oil. Much research has been carried out to study the effects of microlubrication during drilling, milling and turning operations. However, no research is carried out in end milling American Iron and Steel Institute (AISI) 1018 steel using microlubrication. The following section is organized with literature review related to microlubrication with different machining operations.

Microlubrication Drilling

Experiments were carried out to evaluate the effectiveness of microlubrication in achieving higher penetration rate when drilling 1038 steel. Two sets of thru-tool drilling experiments were carried out at a penetration rate of 537 mm/min and 974 mm/min, respectively. A vegetable oil metal working fluid (MWF) (Acculube 6000) was used as the lubricant with a delivery rate of 50 ml/hr at an air pressure of 4.96 bars. Two solid carbide titanium aluminum nitride (TiAlN) coated drills were used to drill 730 holes with a cutting speed of 80 m/min and a feed rate of 0.13 mm/rev for the first set of experiment. Both the drills were analyzed before and after drilling. There was minimal margin and flank wear. The maximum flank wear was 0.13 mm at the outer corner. There was some minimal buildup of material on the margins and near the chisel edge. The spindle power was observed to be constant with the hole depth. For the second set of

experiments, four new drills were used along with one reground and retested, with a cutting speed of 90 m/min and a feed rate of 0.2 mm/rev. The first drill broke on the first hole. The second drill produced sparks and excessive noise after 15 holes due to chipping at the corner of the tool. The third, fourth and the reground tool drilled more than 900 holes. Neither for these tools showed excessive margin or flank wear, although the reground tool showed noticeable build up edge behind the margin. It was concluded that microlubrication can be used for drilling at a much higher penetration rates than gun drilling. Build-up edges (BUE) was observed on the margins and the flanks may be due to excessive hole temperatures. BUE was more common on reground drills than the new ones (Filipovic & Stephenson, 2006).

A study was conducted to report the optimum conditions for ecological deep hole drilling (Murakami & Yamamoto, 2007). The drills having a diameter of 6 mm were specially coated with TiAlN film and a polycrystalline diamond layer. A comparison was done using minimum quantity lubrication (MQL) and emulsion coolant. The work materials used were (S50C/SCM440/FCD700 and carbon steel S48C) to drill a 120 and 106 mm deep hole at a flow rate of 10 cc/min using thru-tool lubrication. The cutting speed of 80 and 60 m/min were used along with a constant feed rate of 0.2 mm/rev. It was observed that both the thrust force and cutting torque obtained under MQL were lower than those under emulsion coolant. The drill life obtained by MQL was 2 times longer than that by emulsion coolant. The carbon steel workpiece was more easily cut by MQL than using emulsion because the workpiece was softened due to the increase in temperature because the cutting was done without a large amount of coolant. The outside nozzle lubrication was also carried out using MQL and emulsion coolant. The workpiece material used was carbon steel S45C. The cutting speeds used were 50, 80, 120, 150 and 180 m/min. The feed rate used was 0.12 mm/min to drill an 18 mm deep hole. MQL was less

effective at high speeds. But, as many as 9283 holes were drilled using MQL at the cutting speed of 120 m/min. While for all the cutting conditions using emulsion cooling, the maximum numbers of holes drilled by were only 4500. It was concluded that MQL was able to lengthen the tool life as compared to emulsion cutting (Murakami & Yamamoto, 2007).

In 2008, a research study was carried out for possible improvements in drilling 319 Al using diamond-like carbon (DLC) coated high-speed steel (HSS) and uncoated HSS tools under external nozzle MQL (Bhowmick & Alpas, 2008). Two types of DLCs (non-hydrogenated and hydrogenated) were considered. The results were compared to drilling using conventional flood coolant and dry drilling. Distilled water spray was used as a minimum quantity lubricant at a flow rate of 30 ml/hr to drill 19 mm deep hole. For flood cooling, water-soluble coolant was used at a flow rate of 30,000 ml/hr. The drilling tests were performed at a cutting speed of 50 m/min using a feed rate of 0.25 mm/rev. It was observed that the torque and thrust force required by MQL drilling were less as compared to dry drilling to a level similar to the performance under the flood condition. In MQL drilling, the mass of Al that adhered to drill bits decreased considerably compared to dry drilling. In addition, a more stable cutting condition was reached as evidenced by the lower number of spikes (sudden jumps due to Al adhesion) in torque and thrust force curves. It was also observed that the smallest BUE formation on the cutting edge of the drill, as well as the Al adhesion to the drill flutes, occurred during MQL drilling with non-hydrogenated DLC, concluding that this type of DLC coating is the preferred coating for drilling 316 Al using a minimum quantity of lubrication (Bhowmick & Alpas, 2008).

Dosbaeva et al. 2008 conducted a research study to improve and evaluate the through-tool MQL conditions. Drills with DLC physically-vapor-deposited (PVD) coatings were again coated with thin perfluoropolyether (PFPE) lubricant films and were compared to traditional

tooling used in wet-machining conditions for the drilling of a cast aluminum-silicon B319 alloy. Approximately 1000 holes were drilled with two types of coatings (DLC; DLC + PFPE) and the progression in flank wear rate, surface finish, tool life and cutting torque were compared. The drilling tests were performed at a cutting speed of 94 m/min using a feed rate of 0.13 mm/rev to drill a 19 mm deep hole. An improvement in the frictional properties of cutting tools prepared with DLC + PFPE coatings was observed for MQL machining conditions. The PFPE surface treatment was found to reduce the cutting torque as well as increase tool life and improve the surface finish of the machined part (Dosbaeva et al. 2008).

In another study, burr analyses were carried out on the drilling process as a function of tool wear and different lubricant-coolant condition (Costa et al. 2009). Dry drilling, use of MQL at a flow rate of 30 ml/hr and fluid applied in conventional way (flood cooling) were compared. The MWFs used were: vegetable oil Accu-Lube-LB-2000 as MQL, mineral oil Shell DMI 410 as MQL and flood coolant, and semi-synthetic oil Shell DMS 250 EP as flood coolant. The trials were carried out at two cutting speeds (45 and 60 m/min) to drill hole having length/diameter (L/D) ratio of 3. The tool used in the tests was the solid twist HSS drill coated with TiAlN, with diameter of 10 mm, to drill the microalloyed steel DIN 38MnS6. The criterion adopted for the end of the test was the catastrophic failure of the drill. It was observed that the MQL system with mineral oil produced the largest average burr heights, while the MQL system with vegetable oil (Acculube LB-2000), along with the dry system, produced the smallest burr heights. The results also showed that the height of the burr increases primarily with the wear of the tool and that this increase is almost exponential after 64% and 84% of drills life, for the speeds of 45 and 60 m/min, respectively. Also, the dry machining tests caused a severe and sudden wear of the

cutting edges of the drill, in such a way that the drill lives were significantly inferior to those of the other systems (Costa et al. 2009).

Shaikh & Boubekri, 2010 investigated the effectiveness of MQL in drilling 1018 steel. Regular HSS tools were used at the cutting speeds of 120, 100 and 80 surface feet per min (SFM) and feed rates of 0.004 and 0.003 inches per revolution (IPR). Acculube 6000 vegetable based lubricant was used as the MWF. The measure of performance was tool life as measured by number of holes drilled and surface finish of the resulting hole. A full factorial experiment was conducted and regression models were generated for both surface finish and hole size. Lower surface roughness and higher tool life were observed in the lowest speed and feed rate combinations. The greatest number of holes was realized using treatment levels of 80 SFM and 0.003 IPR. 880 holes were realized at this treatment. The lowest number of holes was obtained using treatment levels of 120 SFM and 0.004 IPR. Only 280 holes were realized at this treatment. The analysis of variance (ANOVA) clearly indicated that both the cutting speed and feed rate are statistically significant factors based on a 95% confidence level for both the inside diameter deviation and the surface finish analyses (Shaikh & Boubekri, 2010).

Microlubrication Milling Other than Steel

A study was conducted to optimize the cutting parameters using Taguchi method for face milling titanium alloys (Ti6Al4V) with PVD coated inserts using MQL (Hassan & Yao, 2005). An orthogonal array, the signal-to-noise (S/N) ratio and the ANOVA were employed to find the optimal material volume removed and the surface roughness. Sitala (A2407) water-soluble coolant was used at a flow rate of 125 ml/hr. Tool rejection or failure was based on the following ISO standards; (i) maximum flank wear reached 0.7 mm, (ii) notch at the depth of cut reached

1.0 mm, (iii) crater wear depth is more than 0.15 mm, or (iv) flaking or fracture occurs. The tool wear lands were measured using scanning electron microscopy (SEM). The surface finish was measured using a stylus type surface roughometer (JB-3C). The cutting speeds used were 48, 55 and 65 m/min. The feed rates used were 0.10, 0.12 and 0.15 mm/tooth. The depth of cut (DOC) was 1.0, 1.5 and 2.0 mm. It was observed that all the cutting parameters had no significant effect on surface roughness. On the other hand, feed rate was the only significant cutting parameter affecting the material volume removed. The optimum cutting conditions were cutting speed of 48 m/min, feed rate of 0.1 mm/tooth and DOC of 2 mm. Cutting speed and feed rate had no significant effect on material volume removed (Hassan & Yao, 2005).

In 2006, an experimental investigation was done to see the effects of cooling/lubrication on tool wear during high-speed end milling of Ti6Al4V (Su et al. 2006). Dry, flood coolant (Blaser 2000), nitrogen-oil mist, compressed cold nitrogen gas (CCNG) at 0, and -10°C, and compressed cold nitrogen gas and oil mist (CCNGOM) as the cooling/lubrication conditions were studied using cemented carbide tools. For nitrogen-oilmist and CCNGOM, cutting oil was mixed with compressed nitrogen gas at the ambient and lower temperature, respectively. The small amount (120 ml/hr) of cutting oil for the mist requirement was supplied at the pressure of 0.6 MPa by UNILUBE microlubrication system. UNILUB 2032 was used as a mist coolant. SEM analysis was also carried out on the worn tools to determine tool failure modes and wear mechanisms. The objective of this research was to investigate the influence of compressed cold nitrogen gas on tool wear and evaluate its effectiveness in terms of tool life. Cutting speed of 400 m/min, feed rate 0.1 mm/rev, axial depth of cut of 5.0 mm and radial depth of cut 1.0 mm was used. The tool wear rate was examined through toolmakers microscope. The tool was declared failed if (i) average flank wear reached 0.2 mm; (ii) maximum flank wear reached 0.6 mm; (iii)

excessive chipping/flaking or fracture of the cutting edge occurred. It was observed that the tool wear increased rapidly with the cutting time under dry cutting condition. However, the tool wear increased at a lower rate under other cooling/lubrication conditions, especially when using CCNGOM. The smallest flank wear presented by CCNGOM can be attributed to its superior cooling and lubricating performance. The wear progress related to CCNG at 0°C almost coincides with that related to nitrogen-oil-mist, and it was said that the tool wear experienced with CCNG at 0°C was equivalent to that when using nitrogen-oil-mist. Higher tool wear was observed using nitrogen-oil-mist compared to that for CCNG at -10°C. The reason was explained that the lubricating properties of cutting oil diminished due to high cutting temperature at high-speed condition, and the cooling performance of nitrogen-oil-mist was lower than that of CCNG at -10°C. The flank wear when using CCNGOM was much smaller than that with CCNG at -10°C, implying that the small amount of cutting oil performed its lubrication function well under cold nitrogen gas atmosphere and played an important role in reducing tool wear. When the average flank wear reached 0.2 mm, the cutting time for the various cooling/lubrication conditions was 3.639, 5.081, 5.107, 7.195, and 9.792 minutes for dry, nitrogen-oil-mist, CCNG at 0, and -10°C, and CCNGOM, respectively. The tool life using CCNGOM was 2.69 times as much as that under dry cutting condition and 1.93 times as much as that when using nitrogen-oil-mist. It was also concluded that the dominant wear mechanism was diffusion wear under all the cooling/lubrication conditions investigated except for flood coolant. Tool life was the shortest when using flood coolant due to severe thermal fatigue wear. Hence, flood coolant was not suitable for high-speed end milling of Ti6Al4V. The research also stated that further development of compressed cold nitrogen gas was required along with the minimization of hazards of oil mist to the operators (Su et al. 2006).

The effectiveness of MQL as an MWF was carried out in another study related to high-speed machining Ti6Al4V (Zhao et al. 2007). A comparison of MQL machining was done with dry machining. A 25 mm diameter tool with two uncoated cemented carbide inserts were used in this downmilling experiments. A Unilube MQL system using UNILUB 2032 as MWF was used at a flow rate of 9 ml/h. Machining was carried out on Mikron machining center with a cutting speed ranging of 190-300 m/min, a feed rate ranging from 0.05-0.25 mm/tooth, radial depth of cut ranging from 0.5-5.0 mm and axial depth of cut ranging from 1.0-5.0 mm. The cutting force was measured by Kistler 9265B dynamometer. The surface roughness was measured by MAHR-S3P roughmeter. The SEM was done to see the wear mechanism. The tool was declared failed if (i) average flank wear reached 0.3 mm; (ii) maximum flank wear reached 0.6 mm; (iii) excessive chipping/flaking or fracture of the cutting edge occurred. It was observed and concluded that the cutting forces increased with the cutting conditions. Compared to dry machining, MQL brings a significant reduction in cutting forces, and gives rise to a notably prolonged tool life. The tool wear in MQL machining are mainly flank wear and cutting edge wear with a narrow rake face wear. At the same cutting length, the tool wear in MQL machining is far less than that in dry machining. The tool wear mechanisms in MQL were mainly, adhesion, flaking, and abrasion. Some microcracks were found at the flank face near the cutting edge. The surface roughness values in MQL were less than that in dry machining. In both MQL and dry machining, the surface roughness decreases with the increasing cutting speed, feed rate and radial depth of cut. But there seems to be no clear cut relationship between the axial depth of cut and the surface roughness (Zhao et al. 2007).

A face milling test was carried in a comparative way in dry, external and internal MQL conditions on hybrid magnesium and aluminum parts (Sanz et al. 2008). The machining

conditions used for AZ91D/SintD11 (i.e. Case 1) was a cutting speed of 200 m/min, feed rate of 0.25 mm/tooth, axial depth of cut of 0.3 mm and radial depth of cut of 50 mm. The machining conditions used for AZ91D/AlSi18CuNiMg (i.e. Case 2) was a cutting speed of 500 m/min, feed rate of 0.25 mm/tooth, axial depth of cut of 0.5 mm and radial depth of cut of 50 mm. The lubricant used was neat oil based on polyol ester. The flow rate for external MQL was 22 ml/h. The flow rate for internal MQL was 20 and 40 ml/h. The main output considered were surface roughness (Ra), tool wear (VB) and spark generation. The main objective of the test was to analyze and compare the cooling lubrication strategy. In Case 1, machining was carried out for 3.5 m² to detect any possible differences in Ra and VB. It was observed that the external application of MQL offered better surface quality with a value less than 1.5 µm. The internal MQL (20 ml/hr) showed slight improvement concerning flank wear and delaying in obtaining the threshold value of 0.2 mm, for the external MQL the threshold value was reached after machining 0.7 m² and for the internal MQL the threshold value was reached after machining 1.3 m² machining area. Dry machining had the highest surface roughness and flank wear as compared to MQL. Sparks were detected when MQL machining was carried out at a cutting speed of 300 m/min, test were stopped considering fire risks. In Case 2, machining was carried out until the tool wear reached 0.3 mm. It was observed that the behavior was similar to that as in the Case 1. But a slight improvement in the evolution of tool wear was detected using MQL lubrication, reaching the end of tool life at the machined area of 3.9 m² instead of 3.5 m². The external MQL had a 10% improvement in tool life and the internal MQL had a 20% improvement in tool life as compared to dry machining. Overall it was concluded that the application of the MQL systems helps positively, showing a noticeable improvement in tool wear

and productivity. The improvements were more significant with internal MQL supply (Sanz et al. 2008).

Microlubrication End Milling Steel

Iqbal et al. 2008 performed a MQL down-milling experiment to optimize the cutting parameter during machining of hardened cold worked tool steel (62 HRC) using response surface methodology. The experiments (ANOVA) were performed to quantify the effects of cutting speed (V_c), feed rate (f_z), and radial depth of cut (a_e) on tool life and arithmetic average surface roughness. The surface roughness was measured in two directions: along the feed (R_a), and along the pick-feed, R_a (pick). The worn-out tools were analyzed using SEM and energy dispersive spectroscopy (EDS) to determine major mechanism of tool damage. The experiments were performed on Micron vertical milling center using TiAlN coated flat end solid carbide cutters. The cutting speeds used were 175 and 275 m/min. The feed rates used were 0.08 and 0.12 mm/tooth. The depths of cuts used were 0.15 and 0.4 mm. A full factorial, central composite rotational design (CCRD) method was utilized for the design of experiments. The MWF used was UNILUB 2032 at a flow rate of 25 ml/hr with two aerosol ducts kept 160° apart. The tool failure criteria used were either the attainment of a maximum width of flank wear land of 0.2 mm or the occurrence of excessive chipping. All the statistical analyses were done using Design Expert software. It was observed that the effect of cutting speed had a significant effect on tool life and R_a . The effect of feed rate and radial depth of cut had a significant effect on tool life and R_a (pick). It was concluded that tool life could be maximized and surface roughness could be minimized, if MQL hard milling was done at a low values of cutting speed and feed rate. And unexpectedly, the high level of radial depth of cut turned out to be beneficial for the tool life.

Also, an increase in the feed rate accelerated the tool chipping process, while an increase in the cutting speed intensifies the adhesive wear and also initiates the oxidative wear (Iqbal et al. 2008).

An experiment on the effect of the MQL in high-speed end-milling of AISI D2 cold-worked die steel (62 HRC) by coated carbide solid flat end-mills was presented by Kang et al in 2008. The objective of this research was to compare the tool performance of TiAlN and titanium aluminum silicon nitride (TiAlSiN) coated carbides end-mills deposited by hybrid coating method, using flood coolant, dry and MQL conditions. The values of tool wear for coated tools were evaluated using vertical high-speed machining center (Makino, V-55). The x-ray diffraction (XRD) patterns, microstructure, microhardness, and oxidation resistance were investigated. Tool life in terms of the total cutting length was recorded after a tool life criterion of 0.1 mm maximum flank wear had reached. The cutting conditions used were; spindle revolution of 12,000 rpm, feed rate of 0.01 mm/tooth, radial depth of cut of 0.02 mm, and axial depth of cut of 2.0 mm. The MQL flow rate was set at 6 ml/h. It was observed that the Si addition into TiAlN film modified the microstructure of film with grain size refinement. As the Si content increased, the hardness of the TiAlSiN films steeply increased, and reached a maximum value of approximately 48 GPa at a Si content of 8 at.%, and then dropped again with further increase of Si content. The hardness value (~48 GPa) of TiAlSiN film having the Si content of 8 at.% was significantly increased comparing with the hardness value (~30 GPa) for TiAlN film. It was also observed that, as the cutting length increased, the tool wear increased proportionally. In flood cooling, due to the cooling characteristics of the cutting fluid, the tool suffers serious thermal fatigue, and the tool wear rapidly increased compared to the dry and MQL conditions. The wear curve of TiAlSiN coated tool for MQL increased very slightly and showed good cutting

performance. The dry cutting edges of the tool experienced chipping of the bottom and side faces. While the cutting edges of the flood coolant tool experienced catastrophic failure. In case of MQL, both the tool coatings had chipping free edges (Kang et al. 2008).

The primary objective of a finishing process is to minimize the surface roughness and to maximize the tool life. Based on this objective, an investigation was performed to study the effects of materials microstructure, workpiece inclination angle, cutting speed and radial depth of cut on tool life and surface roughness in direction of feed (R_a along) and pick feed (R_a across) (Iqbal et al. 2008). The MQL milling was performed on cold work tool steels (AISI D2 and X210 Cr12) using coated carbide ball-nose end mills. The quantification of the aforementioned effects was done using a new response surface methodology known as the D-optimal method. The SEM and EDS analyses of the worn-out tools were also carried out in order to study the effects of different levels of predictor variables upon the severity of different types of tool wear modes. The experiments were performed on Micron UCP 710 vertical milling center. The flank wear was measured using Tool maker's microscope and the surface roughness was measured using Mahr Perthometer M1. UNILUB 2032 was used as MWF at a flowrate of 25 ml/h, and was applied directly to the tool using two aerosol ducts arranged 160° apart. The axial depth of cut (a_p) was kept 0.3 mm and feed rate (f_z) was fixed to 0.08 mm/tooth for all the experiments. The cutting speed levels used were 38.0, 58.28, 70.7, 76.0, 83.5, and 141.4 m/min. The workpiece inclination angles used were 0°, 22.5°, 28.51° and 45°. The radial depth of cut used were 0.15, 0.27, and 0.35 mm. Down milling was employed as milling orientation. The tool failure criteria used was either the attainment of maximum width of flank wear land of 0.2 mm or occurrence of excessive chipping. The longest tool life obtained was 21,175 mm², while the smallest tool life obtained was 1390.9 mm². The ANOVA was carried out in order to find the reasons for this huge

variation. The ANOVA revealed that the effects of only two parameters, workpiece material and cutting speed are significant upon tool life. It was also observed that the effect of workpiece material was almost 3.5 times more significant than that of cutting speed. It was implied that the chemical composition and hardness of AISI D2 tool steel pose more detrimental effects upon the machinability of the workpiece as compared to X210 Cr12 tool steel. Likewise, the higher values of cutting speed resulted in smaller tool life values, because of the reason that at higher cutting speeds higher temperatures were attained that accelerate the adhesion, diffusion, and oxidation wear modes. The effects of other two parameters, the workpiece's inclination angle and the radial depth of cut, upon tool life, were not significant. The effect of workpiece's inclination angle, upon R_a (along), was extremely significant. The effect of radial depth of cut was also significant but the effects of other two parameters, workpiece material and cutting speed, were insignificant. It was also clear that the high setting of inclination angle and low setting of radial depth of cut provided a surface having small roughness value. On the other hand, for R_a (across), the effect of workpiece's inclination angle was highly significant, followed by that of radial depth of cut. The effects of other two parameters, the workpiece material and the cutting speed, were totally insignificant. AISI D2 had rapid progress of tool wear, while X210 Cr12 tool steel had medium to slow progress of tool wear. It was concluded that the machinability of AISI D2 was poorer than that of X210 Cr12. The high values of cutting speed proved unfavorable for tool life but favorable for surface finish. The workpiece's inclination angle proved to be the most influential parameter for surface roughness. Its higher values provided better surface finish because of avoidance of cutting at the tool's center. The second influential parameter for surface roughness was found to be radial depth of cut. Its higher settings proved harmful for surface finish because of generation of larger cusps at those values. The major tool damage mechanisms

detected were notch wear, adhesion, and chipping. The severity of chipping was relatively smaller as compared to that of adhesion and notch wear (Iqbal et al. 2008).

Another study reported an experimental investigation carried out to evaluate the performance of vegetable oil as an MWF was compared to fatty alcohol (Sharif et al. 2009). MQL machining was compared to dry machining and flood cooling. TiAlN coated four-flute carbide tools were used to machine AISI 420 hardened martensitic stainless steel with tool life and surface roughness as the main responses. The machining trials were performed at cutting speed of 100 m/min and a feed rate of 0.03 mm/tooth. The radial and axial depths of cut were 12 mm and 0.6 mm, respectively. The machining tests were performed on a MAHO 700S computer numerical control (CNC) machining center. Four cooling techniques were employed; dry cutting, flood cooling with 5% concentration of emulsion, MQL with fatty alcohol and MQL with vegetable oil. The MQL cutting fluid was supplied at a flow rate of 17 ml/h. The tool wear was measured at a certain machining interval by using a toolmaker's microscope. The worn tools were also analyzed under high power microscope. A portable surface tester was used to measure the arithmetic surface roughness (R_a) value. The tool rejection or failure was based on the following criteria; (i) average uniform flank wear (VB) ≥ 0.1 mm or (ii) maximum flank wear (VB_{max}) ≥ 0.3 mm or (iii) chipping or catastrophic failure occur. It was observed that flood coolant gave the highest tool wear rate, despite the high quantity of lubricant being used, and the cutting tool posed by flood cooling was unable to penetrate the tool/workpiece interface causing high interfacial temperature. The high wear rate was followed by the occurrence of premature chipping at the flank and was related directly to the shortest tool life of 31 minutes. The MQL gave the lowest wear rate, with fatty acid being the lowest during the initial 60 minutes of cutting time yet it was vegetable-based cutting fluid which assisted the coated carbide tool to last the

longest for 190 minutes. For dry cutting and MQL, the progression of tool wear followed a three-stage pattern in machining, i.e. rapid initial wear, gradual uniform wear, and accelerating wear. The tool life was significantly determined by the gradual uniform stage and it was apparent that MQL contributed in the suppressing the tool wear growth. It was suggested that small amount of lubricant sprayed at the tool/workpiece interface provides a layer of lubrication and this leads to the smoother contact and lowers the cutting temperature. Between the two cutting fluids used for MQL, vegetable-based oil was found to provide better lubrication. Its higher viscosity as compared to the commercial fatty alcohol may be the reason for lower friction at tool/workpiece interface. It was also observed that surface roughness produced by MQL was comparable to the value produced by dry cutting and was better than by flood cutting. The MQL using vegetable oil could even produce surface roughness with a R_a of lower than $0.4\text{ }\mu\text{m}$ during the initial period of cutting time, when the cutting tool was still sharp with only less than 0.05 mm flank wear. The R_a value for flood coolant was between 0.39 and $1.21\text{ }\mu\text{m}$, large amount of cutting fluid was of little effect to the surface roughness. For dry cutting the R_a value was slightly better, in the range of 0.34 and $0.74\text{ }\mu\text{m}$. The R_a value obtained by the MQL with vegetable oil was between 0.23 to $1.0\text{ }\mu\text{m}$ while for MQL with fatty alcohol, the range was between 0.28 to $0.89\text{ }\mu\text{m}$ (Sharif et al. 2009).

Yan et al. 2009 analyzed the cutting performance (i.e. tool wear, surface roughness of the machined workpiece and chip formation) of wet, dry and MQL machining when milling of high strength steel (PCrNi2Mo) using cemented carbide tools under varying cutting speed, feed rate and depth of cut. The main objective of the study was to investigate the machinability using MQL. The MWF used as an MQL was ester oil at a flow rate of 120 ml/h . The cutting speeds used were 50 , 100 , 150 and 200 m/min . The feed rates used were 200 and 300 mm/min . The

depth of cuts used was 0.5 and 0.8 mm. It was observed that the flank wear increased with the increase in cutting speed for all the cutting conditions. The flank wear was the highest under flood cutting condition. The MQL cutting condition provided the lowest flank wear resulting in higher tool life. The surface roughness had a declining trend with the increasing in cutting speed for all the cutting conditions. The improvement in the surface finish can be attributed to the cooling effect which can reduce the friction coefficient between the chip-tool interface. It was also seen that the color of the chips became darker when cutting speed was higher indicating that the cutting temperature increased with the cutting speed under all cutting conditions. Also, the flank wear and surface roughness increased with the increase in feed rate and depth of cut with MQL providing the best results. In case of wet machining, unsatisfactory tool life was observed because of the occurrence of thermal cracks on the cutting edge caused by thermal shocks. Moreover the chip-tool contact was mostly plastic at higher cutting speed and feed rates, so the cutting fluid applied conventionally cannot reduce the chip-tool interface temperature effectively as the fluid cannot penetrate into the interface (Yan et al. 2009).

Another study was undertaken to analyze the burr formation during milling process using internal MQL and comparison was done with dry cutting (Heisel et al. 2009). In milling operation, burrs are formed on entry and exit edges of the workpiece to be machined like in all material removal processes. In the subsequent production these burrs have to be removed. Understanding the influencing factors and burr formation mechanisms can help to avoid/reduce burrs and lower the overall machining cost. The tests were conducted on an EX-CELL-O XHC241 machining centre. A face milling cutter and an angle milling cutter are used as test tools. A single channel unit by the company Lubrix was used as MQL system using Ecocut Mikro Plus 82 as lubricant. This lubricant was developed especially for MQL machining and is

based on special fatty alcohols. The chemical vapor deposited (CVD) indexable inserts coated with TiCN + Al₂O₃ (+ TiN) was used to machine heat-treatable steel C45E. The cutting speed (V_c) used was 225 m/min for the comparative tests, and the feed per tooth (f_z) was 0.11 mm/rev. For the further tests the cutting speed was varied in the range from 150 to 225 m/min, and the feed per tooth was varied in the range between 0.05 to 0.11 mm/rev. The tests were performed with a constant depth of cut (a_p) 3 mm. In addition, the width of cut (a_e) was varied. Concerning the face milling cutter, the milling was conducted in the middle of the workpiece with a width of cut of 12.5, 25 and 37.5 mm. Regarding the angle milling cutter, widths of cut (a_e) was 6.25, 12.5, 18.75 and 23.5 mm. In the initial test, the lubricant flow rate was varied from 0 to 15, with 0 corresponding to dry cutting and 15 corresponding to max flow rate of MQL. The burr value decreases with growing MQL. The greatest difference in burr value was detected for the variants MQL 0 (dry) and MQL 5 (minimum quantity). For this reason the tests with the settings MQL 0 and MQL 5 of the Lubrix system were continued. One parameter was varied at a time keeping the other parameter constant. It was observed that varying cutting speed had little to no effect on the burr size. When the feed rate was varied it was observed that when the machining with MQL, the burr value drops at first and then rises again from a feed of 0.07 mm up, before its course remains nearly constant from feed of 0.09 mm up. In dry machining the burr behaves in exactly the opposite way. The burr value here increased slightly at first, dropped when feed is 0.07 mm to 0.09 mm and then increased moderately with growing feed. Also, the tendency to burr formation gets lower for as width of cut was increased. The burr value with MQL was less than in dry machining from a width of cut of 12.5 mm and up. The external MQL was also tested. The spray positions of 90° and 180° proved to be favorable with regard to a lower burr formation. The internal supply and dry machining, however, provided better results. Regarding angle

milling cutters, investigations into the influence of corner radius revealed that the burr value increased with growing corner radius. In face milling, it was detected that the burr value decreased with increasing corner radius (Heisel et al. 2009).

Fluids not Suggested for Microlubrication (Khan et al. 2009)

1. Water mixed cooling lubricants and their concentrates because they promote rusting of the workpiece and do not properly lubricate the tool/workpiece interface.
2. Lubricants with organic chlorine or zinc containing additives.
3. Lubricants that have to be marked according to the decree on hazardous materials, and
4. Products based on mineral base oils in the cooling lubricant which have 3 ppm (parts per million) benzpyrene.

Why Use Vegetable Oil

From the viewpoints of performance, cost, health, safety and environment, vegetable oils are considered as viable alternative to other metalworking cutting fluids (Khan & Dhar, 2006):

1. The molecules of vegetable oil are long, heavy, and dipolar in nature, they create a dense homogeneous and strong lubricating film that gives the vegetable oil a greater capacity to absorb pressure.
2. The lubricating film layer provided by vegetable oils is intrinsically strong and lubricious which improves workpiece quality and overall process productivity reducing friction and heat generation.
3. The vegetable oils have a higher flash point which yields an opportunity to increase the metal removal rate resulting in the reduction of smoke formation and fire hazard.

4. The higher boiling point and greater molecular weight of vegetable oil result in considerably less loss from vaporization and misting.
5. Since high temperatures ($>100^{\circ}\text{C}$) are not operative in end milling, the thermal and oxidative degradation of vegetable oils is a non-issue as it is in engine tribology.
6. Vegetable oils are nontoxic to the environment and biologically inert and do not produce significant organic disease and toxic effect.
7. No sign and symptom of acute and chronic exposure to vegetable oil mist have been reported in human (ACGIH, 2001).
8. The vegetable oils are highly viscous basic oil which are recommended for better atomization (Rahman et al. 2002).

Why Use AISI 1018 Steel

1. It has better machinability rating (i.e. 78%) as compared to other low carbon steel (e.g., AISI 1020 steel has a machinability rating of 72%) (ASM International, 1990).
2. It has good weldability (i.e. less weld cracks, higher toughness, less heat affected zone) as compared to medium and high-carbon steel (ASM International, 1990).
3. It is good carburizing steel (ASM International, 1990).
4. AISI 1018 steel find applications in manufacturing of axles, bolts, shafts, machinery parts, gears, pinions worms, king pins and ratchet (Dhiman et al.2008).
5. It is cheaper as compared to other materials ($\approx \$1.45/\text{lb}$) (Lokey Metals, Fort Worth, Texas).

Summary

From the literature review we can summarize that machining using microlubrication can almost eliminate the use of cutting fluid without compromising the surface integrity and tool life. Microlubrication eliminates the drawback of dry cutting and incorporates in itself the merits of flood cutting without using thousands of liters of cutting fluids every year. We also came to know that cost incurred in the use of MWF are not only the procurement and disposal costs, but also costs resulting from additional investments such as containers, pipes, pumps, filtration facilities as well as the personnel costs of monitoring, upkeep and cleaning of the cutting fluid (Heisel et al. 2009). The literature review revealed that microlubrication has been carried out on many different machining operations including drilling and milling. The thru-tool application of microlubrication had more benefit when drilling. Many studies reviewed different types of MWF like vegetable oil, synthetic esters, fatty alcohol and mineral oils. But among these cutting oils, vegetable-based oil was considered as the most ecofriendly cutting oil. Vegetable-based oil was also found to provide better lubrication. One study also showed that drilling under microlubrication with vegetable oil (Bluebe LB-20/Acculube 6000) had higher penetration rate upto 974 mm/min. This study was conducted on 1038 steel with solid carbide TiAlN-coated drills. In order to improve the machining process using microlubrication, apart from presenting the regular study to optimize the machining parameter and the cutting fluids, more research is needed to determine the mist characterization and the microstructure characterization.

Conclusion

All previous studies mainly concentrated on comparing microlubrication as a machining process with other cutting processes like dry cutting and flood cutting. There has not been any

research to identify and investigate the effect of vegetable oil as a MWF on the workpiece microstructural evolution and workplace environment. Limited studies have been performed to determine the quality of mist produced while under microlubrication. Lastly, no study has been reported to date on end milling 1018 steel under microlubrication and the resultant microstructural deformation.

CHAPTER 3

EXPERIMENTAL METHODS AND PROCEDURES

This chapter includes the experimental methods and procedures used to conduct this study. This includes the proposed design of experiment (DOE) study, the cutting condition used, the cutting tools, the end-milling equipment, the workpiece material and its phases and composition, the end-milling procedure and the tool failure criteria. Also, the aerosol mass concentration and aerosol particle size measurements, the tool wear measurements, the vickers hardness measurements, dislocation density quantification, tool/workpiece interface temperature measurement, and grain size and texture measurements have been studied and are presented here in detail. Additionally, the method of data analysis for multivariate analysis of variance (MANOVA) is also explained.

Design of Experiment

The study was conducted using a full-factorial design to effectively investigate the main effects as well as the interaction among the independent variables. Table 2 shows the factorial experiment layout. The independent variables were cutting speed and feed rate. The axial depth of cut and the radial depth of cut were constant at 0.125 and 0.25 inch, respectively. The four dependent variables were flank wear side 1, flank wear side 2, aerosol mass concentration and aerosol particle size. The cutting speed and the feed rate are expressed in surface feet per minute, (SFM) and inches per tooth (IPT), respectively.

Table 2: Factorial experiment layout of cutting speed and feed rate combination.

Solid Carbide End Mill 1 inch diameter		Cutting Speeds (SFM)		
		80	100	120
Feed Rates (IPT)	0.003	80, 0.003	100, 0.003	120, 0.003
	0.005	80, 0.005	100, 0.005	120, 0.005

The experiment was fully randomized. The process of randomization of data involves randomly allocating the experimental units across the treatment groups. As shown in Table 2, there are six combinations of cutting speed and feed rate. Hence, six experiments were performed each consisting of one of the six combinations. At the start of every experiment, one combination of cutting speed and feed rate was selected at random and manually inserted into the machine through a computer numerical control (CNC) program. After tool failure, one combination was again selected at random and inserted into the CNC program replacing the earlier combination. This procedure of randomly selecting the cutting speed and feed rate combination was followed until all six experiments were completed.

Cutting Tool

The cutting tool used for this experiment was a square-end solid carbide end mill having two-flutes. The tools were ordered in a batch of 8, assuming that all the tools used in the experiments were of the same make without any differences. The tools were manufactured by Guhring Inc. with the following specifications (Guhring Inc, 2012):

- Series: UNI PRO End Mills 3146
- Standard/Type: Guhring/N
- Tool material: Solid carbide (Tungsten carbide – 90% and Cobalt – 10%)
- Surface finish: Bright oxide
- Number of flutes: 2
- Diameter: 1.0 inch
- Total length: 4 inch
- Flute length: 1.5 inch

- Helix angle: 30°

Figure 2 shows the end mill used in this experiment with clearly marked side 1 and 2. The end mill was mounted on a tapered shank tool holder before being inserted into the tool magazine.



Figure 2: Solid carbide end mill.

Workpiece Material

American Iron and Steel Institute (AISI) 1018 hypoeutectoid steel was used as workpiece material supplied by Lokey Metals located in Fort Worth, Texas. The material is available in round, square, rectangle, hexagonal and plate shapes. The material was cold-rolled with an approximate hardness of 170 HV. Table 3 shows the chemical composition of AISI 1018 steel as given by the material supplier. Table 4 shows the mechanical properties of AISI 1018 steel.

Table 3: Chemical composition of AISI 1018 steel.

Element	Weight %
Carbon (C)	0.190
Manganese (Mn)	0.690
Phosphorus (P)	0.019
Sulphur (S)	0.019
Silicon (Si)	0.240
Copper (Cu)	0.280
Nickel (Ni)	0.100
Chromium (Cr)	0.200
Molybdenum (Mo)	0.040
Vanadium (V)	0.004
Tin (Sn)	0.013
Niobium (Nb)	0.002
Aluminum (Al)	0.022
Titanium (Ti)	0.001

(Source: Lokey Metals, Fort Worth, Texas).

Table 4: Mechanical properties of AISI 1018 steel.

Mechanical Properties	Metric	English
Hardness, Vickers	170	170
Ultimate tensile strength	440 MPa	63800 psi
Yield strength	370 MPa	53700 psi
Modulus of Elasticity	205 GPa	29700 ksi
Bulk Modulus	140 GPa	20300 ksi
Shear Modulus	80 GPa	11600 ksi
Machinability	78%	78%

(Source: www.matweb.com; ASM International, 1990).

Figure 3 shows the schematic representations of the microstructures for hypoeutectoid steel as it is cooled from within the austenitic phase region to below the eutectoid temperature. Cooling an alloy of this composition is represented by moving down the vertical line yy' . At about 875°C , i.e., point c, the microstructure will consist entirely of grains of the γ -austenite phase. In cooling to point d, at about 775°C , the α -ferrite + γ -austenite phases will coexist. Cooling from point d to e, just above the eutectoid but still in the α -ferrite + γ -austenite region, will produce an increased fraction of the α -ferrite phase and a microstructure similar to that also shown in the figure 3 consisting of larger grown particles (Callister, 2007).

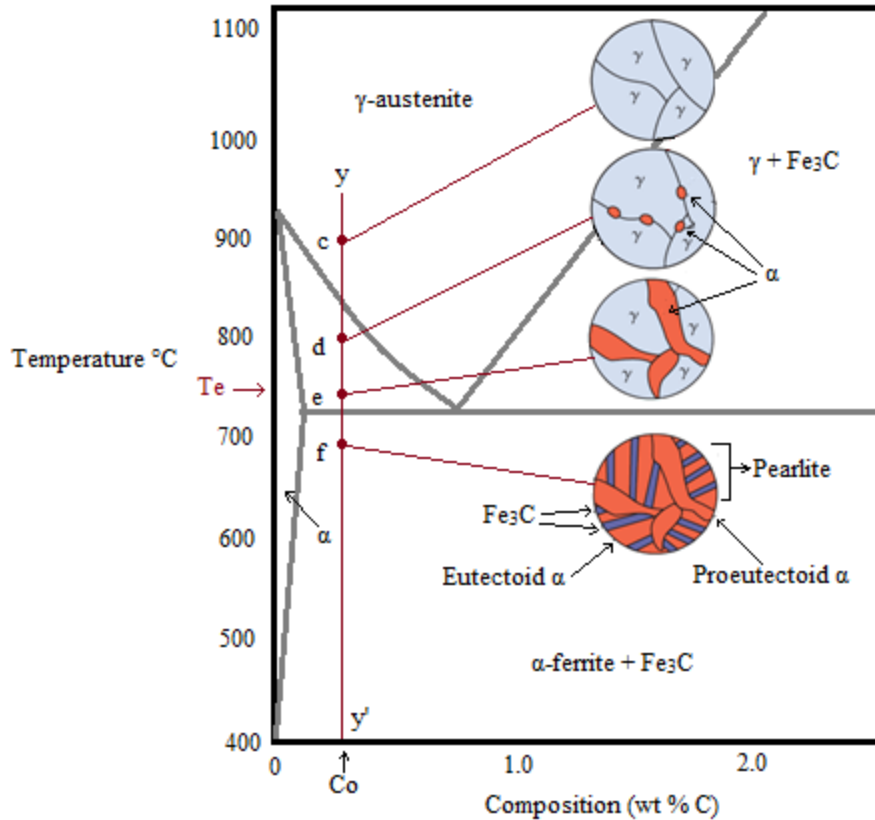


Figure 3: Schematic representation of microstructures for AISI 1018 steel.

As the temperature is lowered just below the eutectoid, to point f, all the γ -austenite phase will transform to pearlite. There will be no change in the α -ferrite phase; it will be present in the form of continuous matrix phase surrounding the isolated pearlite colonies. The ferrite phase will be present both in the pearlite and also as the phase that formed while cooling through α -ferrite + γ -austenite phase region. The ferrite that is present in the pearlite is called eutectoid ferrite, whereas the other, that was formed before eutectoid is termed as proeutectoid ferrite (Callister, 2007). The pearlite has a lamellar structure which consists of α -ferrite and Fe_3C .

Figure 4 shows a SEM image of as-received AISI 1018 steel, with clearly marked proeutectoid ferrite and pearlite. A magnified image of the iron carbide showing the lamellar structure is also shown in figure 4. Figure 5 gives us a much clear picture of the pearlite with a

clear distinction of the α -ferrite and Fe_3C (Iron carbide/Cementite).

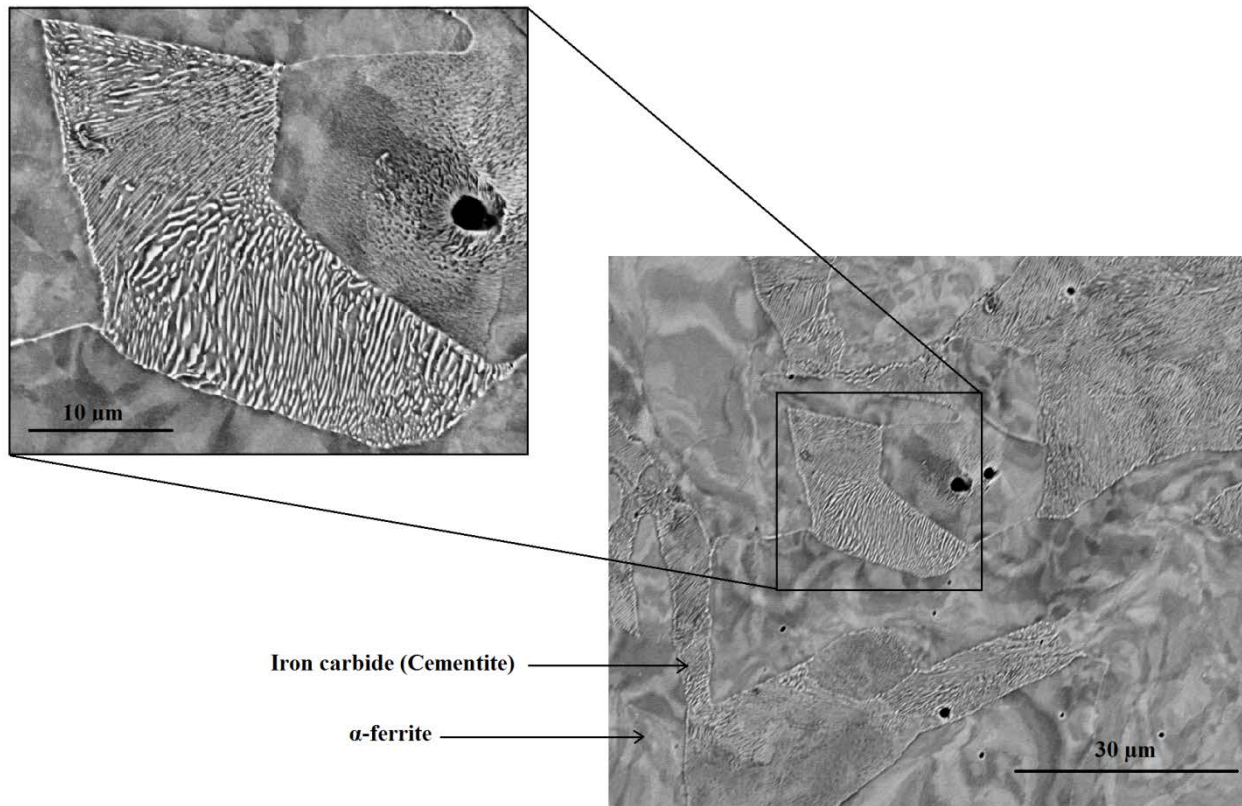


Figure 4: SEM image of as-received AISI 1018 steel.

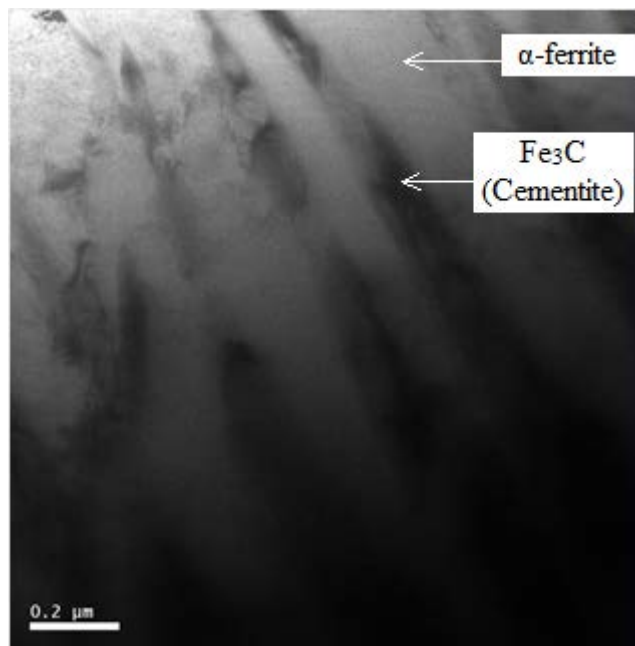


Figure 5: TEM image of pearlite.

End Milling Equipment

A CNC Mori Seiki Dura Vertical 5060 machining center was used to perform the end milling operation for this study. Figure 6 shows the machine in idle condition.

The following are the specifications of the machining center:

- Manufacturer: Mori Seiki
- Machine type: Vertical milling machine
- NC controller: Fanuc MSX-504 III
- Maximum power: 15 HP
- Maximum spindle speed: 10000 RPM
- Travel range in X x Y x Z-axis: 23.600 x 20.900 x 20.100 inches

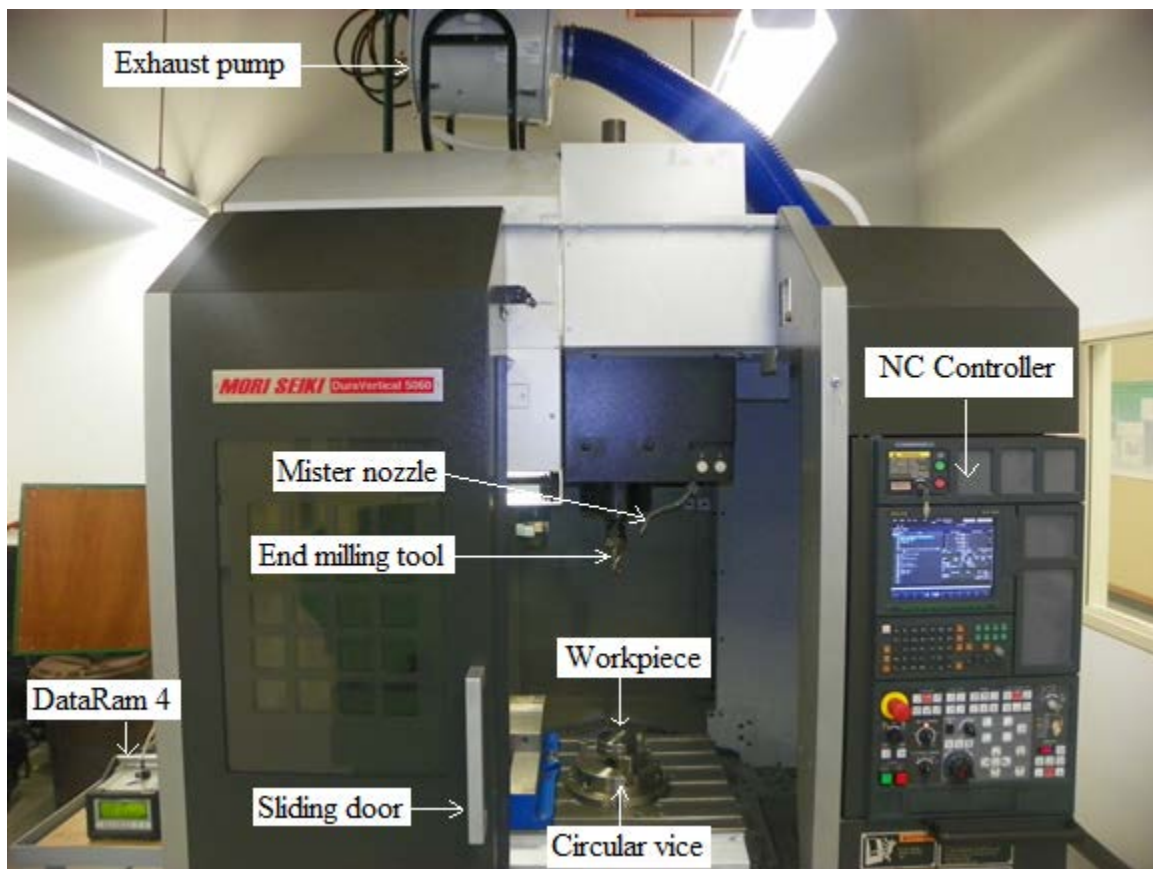


Figure 6: Mori Seiki Dura Vertical 5060 machining center.

The machining center was equipped with an exhaust pump as shown in figure 6. The exhaust pump was a Darwin 2000M model, manufactured by Losma, Inc. The machining center was also equipped with a single nozzle Kuroda Ecosaver KEP3 micro lubrication system as shown in figure 7. The lubricant flow rate was maintained at 12 ml/h at an air pressure of 0.1 MPa.



Figure 7: Kuroda Ecosaver KEP3 micro lubrication system.

The machining center was equipped with a tool magazine with a maximum storage capacity of 30 tools. The machining area was fully enclosed when in operation.

Metal Working Fluid (MWF)

Accu-Lube 6000 vegetable-based lubricant was used as a metal working fluid. It is manufactured by ITW ROCOL North America. The lubricant was specially recommended for micro lubrication of ferrous and non-ferrous materials. It is manufactured using renewable raw

materials and is non-toxic and biodegradable. It is not diluted in water before use. The physical properties of Accu-Lube 6000 are listed below:

Table 5: Mechanical properties of Accu-Lube 6000.

Mechanical Properties	Values
Appearance	Blue
Specific gravity	0.92
Viscosity at 40°C	8.9 cSt
Flash point	418°F (214°C)
Pour point	-40°F (-40°C)
Pin & Vee block	1250 lbs
Sulphur	None
Chlorine	None
Silicon	None
VOC	Nil
Mineral oil	0%
Water solubility	Insoluble

(Source: ITW Rocol North America, 2012).

Aerosol Mass Concentration and Aerosol Particle Size Measurements

The aerosol mass concentration and aerosol particle size measurements were done using the Thermo Scientific DataRam4. The DataRam 4 is a portable, high-sensitivity, two-wavelength nephelometric monitor with a light scattering sensing configuration that has been optimized for the measurement of the fine particle fraction of airborne dust, smoke, fumes, and mists in ambient, atmospheric, industrial, research, and indoor environments. The DataRam 4 provides direct and continuous readout as well as electronic recording of the information gathered (Thermo Scientific, 2012). The DataRam4 has an aerosol mass concentration measuring range of 0.0001 to 400 mg/m³. The DataRam4 is capable of storing 50,000 data points which include individual point averages and detecting the median particle size of up to 0.05 µm. Figure 8 shows the DataRam 4 attached with a non-electrostatic Tygon tube to measure the aerosol mass concentration and the aerosol particle size produced during the end milling experiments.

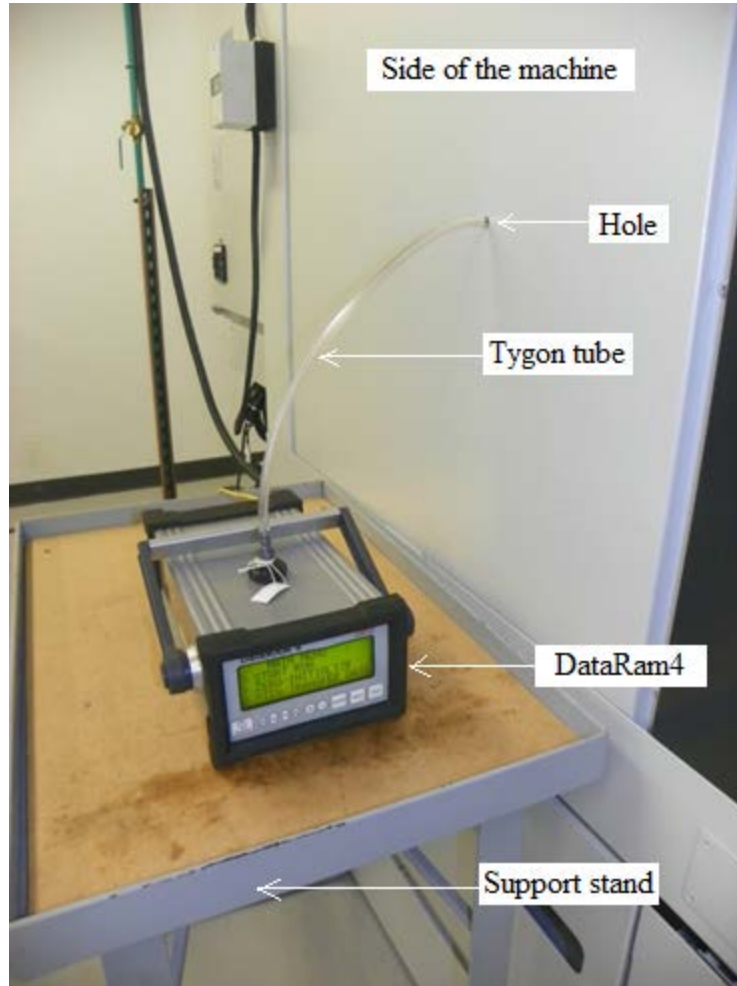


Figure 8: Thermo scientific DataRam4.

A hole was made on the side of the machine to insert the tygon tube near the machining area. A rubber grommet was used to seal the hole near the tygon tube. The position of the DataRam4 and the tygon tube was adjusted properly to minimize the turbulence produced by the mist during machine operating condition.

Samples Preparation

AISI 1018 steel samples were available in the form of circular blocks of 4 inch diameter and 1.5 inch thickness. The samples were previously cut from a 10 feet long AISI 1018 steel bar stock for a drilling study. One side of the circular block already had 1 inch deep drilled holes on

it from the earlier experiment. The other side was used for the end milling experiment. The idea of using the previously drilled workpieces saved a lot of time and money for the study. The final sample ready for doing end milling experiments is shown in figure 9.



Figure 9: Final sample.

End Milling Procedures

A CNC program was written and inserted into the machining center using the Fanuc NC controller. Dry runs were conducted to test the program. The Kuroda microlubrication system was filled with the required coolant (i.e. Accu-Lube 6000) and was set to the flow rate of 12 ml/hr and the air pressure of 0.1 MPa. The nozzle was positioned properly to spray exactly on the tool-workpiece interface. The tool was inserted in the tool magazine. Before the start of the end milling process, it was ensured that the workpiece was tightly held in the circular vice and the machine sliding door was closed. The DataRam4 was also turned 'ON'. The workpiece to be drilled were kept randomly on the pallet so that when any sample was selected for the

experiments that sample would be a random sample. There should not be any bias in the experiment.

The end milling procedure is as follows:

1. Select at random a combination of cutting speed and feed rate from table 1.
2. Turn 'ON' the machining center (Mori Seiki, Dura vertical 5060).
3. Insert the selected cutting speed and feed rate into the machine through the NC controller.
4. Turn 'ON' the exhaust pump.
5. Press the green 'Cycle Start' button on the numerical control (NC) controller.
6. Press the 'Start Run' button on the DataRam4.
7. After the machining cycle is complete, press the 'Terminate Run' button on the DataRam4.
8. Turn 'OFF' the exhaust pump.
9. Open the sliding door.
10. Remove the workpiece from the circular vice.
11. Remove the cutting tool and measure its flank wear by toolmaker's microscope.
12. If the flank wear is less than the failure criteria load the cutting tool in the tool magazine.
13. Load a new workpiece and repeat Step 4 to 12 until the tool fails.

The tool was declared failed, if the flank wear of any one of the two flanks went above 0.5 mm (ASM International, 1989). If the cutting tool fails, load a new cutting tool in the tool magazine. Do the tool length compensation for the cutting tool and follow the same end milling procedure again. Before loading the next component in the circular vice, ensure that the vice is thoroughly cleaned of chips and coolant. At the end of each day, save all the readings from the DataRam4 into the computer. All data collected should be saved on a spreadsheet.

Method of Data Analysis for MANOVA

MANOVA was conducted to investigate the main and the interaction effects of the independent variables (namely, cutting speed and feed rate) on all the dependent variables namely flank wear side 1, flank wear side 2, aerosol mass concentration and aerosol particle size. Minitab 16 statistical software was used for the data analysis.

The following steps were taken in the MANOVA analysis:

1. Organize and input the data obtained from tool flank wear measurement and the DataRam4.
2. Verify the MANOVA assumptions by analyzing the 'Normal plots of residuals', 'Residuals versus the fitted values' and 'Equality of covariance'.
3. Conduct data transformation if required.
4. Perform the significant test of the independent variables at 95% confidence level.
5. Plot graphs to aid in analyses.

MANOVA Assumptions

1. Data should be randomly sampled from the populations of interest.
2. Observations should be independent of one another.
3. The dependent variables should have a multivariate normal distribution within each group. The dependent variables should also meet univariate normality assumptions.
4. Equality of covariance matrices of all groups of dependent variables. This assumption is two-folds:
 - (i) The ANOVA homogeneity of variance assumption must be met for each dependent variables;

- (ii) The correlation between any two dependent variables must be the same in all groups (Bray & Maxwell, 1985).

Robustness of MANOVA

Although the MANOVA assumptions are mathematical requirements for MANOVA, in practice it is unlikely that all of the assumptions will be met precisely. Under many conditions in MANOVA, violating the assumptions does not necessarily invalidate the results. In other words, MANOVA is relatively robust to violations of the assumptions in many circumstances. However, MANOVA is not robust to violations of either of the first two assumptions. Departures from multivariate normality generally have only very slight effects on the Type I error rates of the four statistics. The sole known exception to this rule is that Roy's greatest characteristic root test may lead to much Type I errors when only one of several groups has a distribution with high positive kurtosis. Departures from normality may reduce statistical power. One possible solution to this problem is to employ transformations of the data to achieve normality (or at least approximate it more closely), in much the same manner as ANOVA.

The effects of failing to meet the equality of covariance matrices assumption are more complicated. When sample sizes are unequal, none of the four test statistics is robust. Depending on the relationship between the sample sizes and the covariance matrices, either too many or too few Type I errors will result. When sample sizes are equal, all of the test statistics tend to be robust unless sample sizes are small, or the number of variables is large, and the difference in matrices is quite large. However, Olson 1974, has found that the Pillai-Bartlett trace is much more robust across a wide range of population configurations than any of the other three statistics (Bray & Maxwell, 1985).

Hypotheses

1. Null Hypothesis:

There is no significant difference between the responses (i.e. flank wear side 1 & 2, aerosol mass concentration and aerosol particle size) obtained by varying the individual input variables (i.e. cutting speed and feed rate).

2. Alternate Hypothesis:

There is a significant difference between the responses (i.e. flank wear side 1 & 2, aerosol mass concentration and aerosol particle size) obtained by varying the individual input variables (i.e. cutting speed and feed rate).

Tool Flank Wear Measurements

The cutting tools flank wear measurements were done by Mitutoyo toolmaker's microscope. The microscope and a magnified inset image of the tool flank face showing the flank wear as seen from the microscope is shown in figure 10. The microscope has a maximum magnification of 40X. The cutting tool was set on the XY-stage with its flank aligned with the Y-axis as seen from the eyepiece. The microscope has a contour illumination from the bottom suited for measurement and inspection of specimen contour and a surface illuminator for observation and inspection of specimen surfaces. A digital micrometer head was attached to the X and Y-axis and was set to zero. The micrometer was equipped with digital data display which gave live readings. The Y-Axis was carefully moved in +Y-directions and was aligned with the maximum flank wear valley as seen on the tool from the eyepiece. Reading from the micrometer was then collected and recorded in MS-Excel manually.

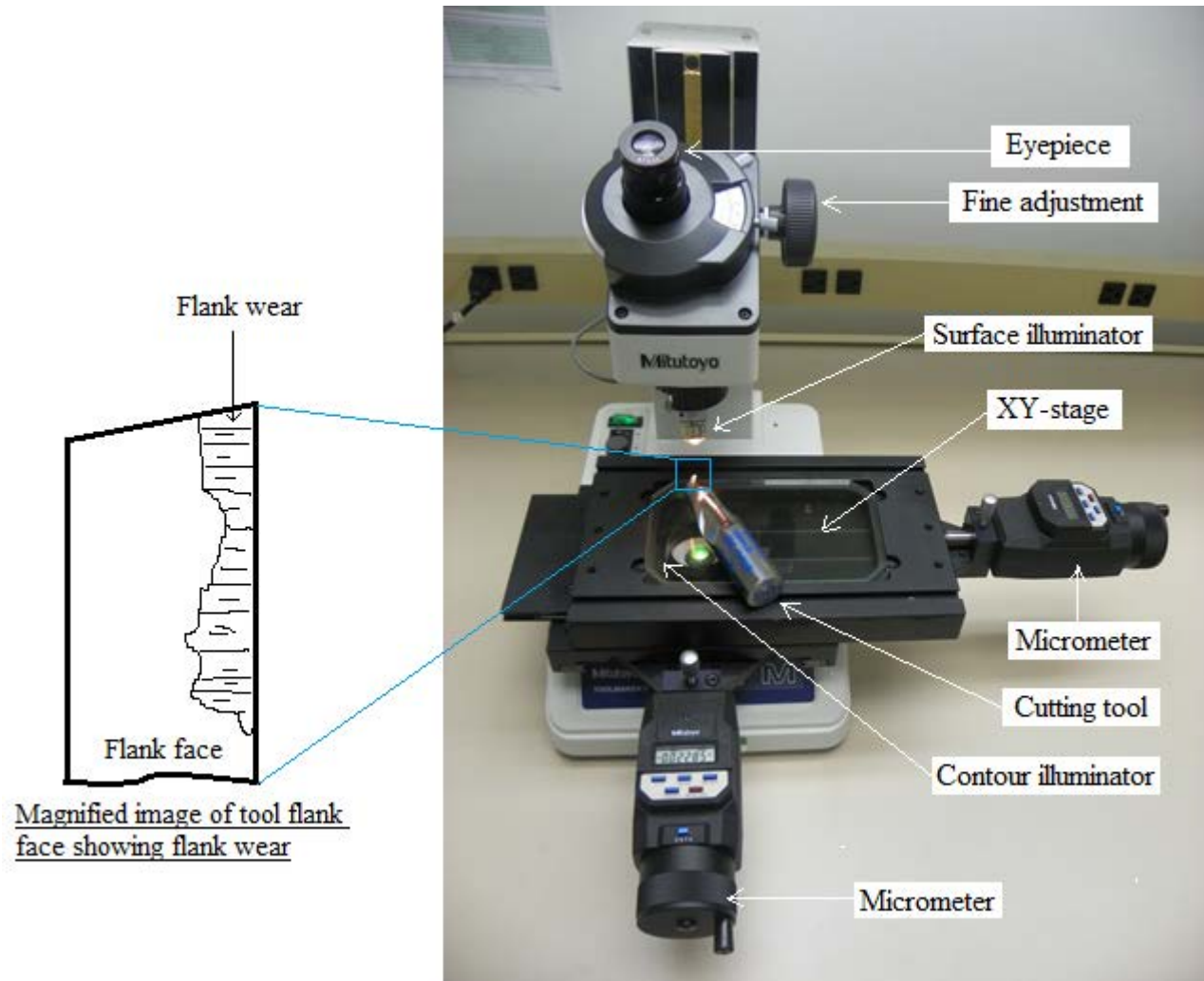


Figure 10: Mitutoyo toolmaker's microscope.

The toolmaker's microscope was also equipped with a camera to take pictures of the specimen. The camera can be fixed on the eyepiece. A picture taken from the camera is shown in figure 11 with the cutting tool rake face of side 2 for treatment 100 SFM and 0.003 IPT.

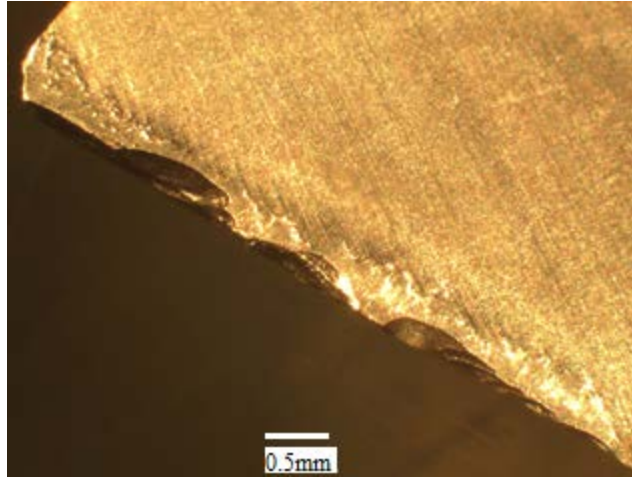


Figure 11: Optical micrograph of tool rake side 1 - Treatment 100 SFM and 0.003 IPT.

Tool-Workpiece Interface Temperature Calculations

The interface temperature between the cutting tool and the workpiece was calculated using Peclet numbers. When the cutting tool and the workpiece are in contact the interface experiences a rise in temperature. The mechanical energy which is required to overcome the frictional resistance during machining is dissipated through a conversion into thermal energy and is responsible for the tool-workpiece interface temperature rise. This increase in temperature can sometime even lead to cutting tool failure. The temperature rise is of very short durations and is called 'flash temperature'. The presence of the lubricant in the tool-workpiece interface will affect the temperature rise. Some part of the heat will be convected away by the lubricant, resulting in the cooling of the interface. Therefore, an accurate value of the coefficient of friction is very difficult to obtain; however, in most lubricated contacts the coefficient of friction is <0.1 (Stachowiak & Batchelor, 2005).

There is no single algebraic equation giving the flash temperature for the whole range of surface velocities and contact geometries. A non-dimensional measure of the speed at which the

two surface moves across each other called the ‘Peclet number’ is used as a criterion allowing the differentiation between various speed regimes and contact geometries.

The peclet number (Stachowiak & Batchelor, 2005) is defined as:

$$Pe \text{ (Peclet \#)} = Ua/2\chi$$

where:

Pe = peclet number;

U = velocity of solid (workpiece or tool) [m/s];

a = contact dimension [m], (i.e. contact radius for circular contacts, half width of the contact square for square contacts and the half width of the rectangle for linear

contacts); here $a = \left(\frac{4WR'}{L\pi E'} \right)^2$ where:

W = normal load, here = mg;

R' = reduced area of curvature, here = $(1/R_{\text{tool}}) + (1/R_{\text{workpiece}})$

E' = reduced young's modulus, here = $\{(1-\nu_{\text{tool}}^2)/E_{\text{tool}}\} + \{(1-\nu_{\text{workpiece}}^2)/E_{\text{workpiece}}\}$

E = young's modulus

χ = thermal diffusivity [m²/s]. i.e., $\chi = \kappa/\rho\sigma$, where:

κ = thermal conductivity [W/mK];

ρ = density [kg/m³];

σ = specific heat [J/kgK].

Peclet number is the ratio of speed of the surface to the rate of thermal diffusion into the solid. It is an indicator of the heat penetration into the bulk of the contacting solid, i.e., it describes whether there is sufficient time for the surface temperature distribution of the contact to diffuse into the stationary solid. A higher Peclet number indicates a higher surface velocity for constant materials characteristics.

The heat transfer effects vary with the Peclet number. The following velocity ranges, defined by their Peclet number, are considered in flash temperature analysis (Stachowiak & Batchelor, 2005):

$Pe < 0.1$ one surface moves very slowly with respect to the other. There is enough time for the temperature distribution of the contact to be established in the stationary body, i.e., steady state conduction.

$0.1 < Pe < 5$ intermediate region one surface moves fast with respect to other, and a slowly moving heat source model is assumed.

$Pe > 5$ one surface moves fast with respect to other and is modeled by a fast moving heat source. There is insufficient time for temperature distribution of the contact to be established in the stationary body. The depth to which the heat penetrates into the stationary body is very small compared to the contact dimensions.

The heat partition or proportion of heat (η) in the workpiece and the tool can be calculated by,

$$\eta_{\text{workpiece}} = 1 / (1 + (\kappa_{\text{tool}} \times \sqrt{Pe_{\text{tool}}} / \kappa_{\text{workpiece}} \times \sqrt{Pe_{\text{workpiece}}}))$$

Note that the Pe can be dropped from the equation if the value of Pe is very low.

Table 6: Average and maximum flash temperature formulae for line contacts (Stachowiak & Batchelor, 2005).

Peclet number	Average flash temperature Tf_a	Maximum flash temperature Tf_{\max}
$L < 0.1$	$0.318 \times \frac{\mu W (U_a - U_b)}{Kl} \times \frac{\chi}{U_b}$ $\times (-2.303 L \log_{10} 2 Pe + 1.616 Pe)$	$0.318 \times \frac{\mu W (U_a - U_b)}{Kl} \times \frac{\chi}{U_b}$ $\times (-2.303 L \log_{10} Pe + 1.616 Pe)$
$0.1 < L < 5$	$0.159 C_3 \times \frac{\mu W (U_a - U_b)}{Kl} \times \frac{\chi}{U_b}$ (where $C_3 = 1.1$)	$0.159 C_4 \times \frac{\mu W (U_a - U_b)}{Kl} \times \frac{\chi}{U_b}$ (where $C_4 = 1.3$)
$L > 5$	$0.266 \times \frac{\mu W (U_a - U_b)}{Kl} \times (\frac{\chi}{U_b})^{0.5}$	$0.399 \times \frac{\mu W (U_a - U_b)}{Kl} \times (\frac{\chi}{U_b})^{0.5}$

Flash temperature formulae for line contacts for various velocity ranges are summarized in table 6.

where:

μ = coefficient of friction;

U_a, U_b = surface velocities of solid 'A' (i.e. workpiece) and solid 'B' (i.e. tool);

l = half length of the line contact [m]

Flash temperature equations are given in terms of the heat supply over the contact area, the velocity and the thermal properties of the materials. They are derived based on the assumption that the proportion of the total heat flowing into each contacting body is that the average temperature over the contact area is the same for both bodies.

The next step is to calculate the true flash temperature rise and maximum flash temperature rise. The true flash temperature rise must be the same for both the solids in contact and is calculated from:

$$1/T_f = 1/T_{f_{\text{workpiece}}} + 1/T_{f_{\text{tool}}}$$

The maximum temperature rise is calculated by the formulae:

$$1/T_{f_{\text{max}}} = 1/(T_{f_{\text{max}}})_{\text{workpiece}} + 1/(T_{f_{\text{max}}})_{\text{tool}}$$

Vickers Hardness Measurement

The hardness measurements were carried out using Shimadzu dynamic ultra micro hardness tester model # DUH-211S as shown in figure 12. The hardness tester is equipped with an optical microscope and a X and Y-axis micrometer. The hardness tester uses a standard type 115° standard pyramid indenter. Electromagnetic force is used to press the indenter against a specimen. The pressing force is increased at a constant rate, from 0 to the preset test force. The

indentation depth is automatically measured as the indenter is pressed against the specimen. This allows dynamic measurement of changes that occur in the specimen's resistance to deformation during the indentation process. The hardness tester measures dynamic hardness and evaluates the hardness that corresponds to both plastic and elastic deformation (Shimadzu, 2012). Readings were taken along the cross-section from the edge of the machined surface.

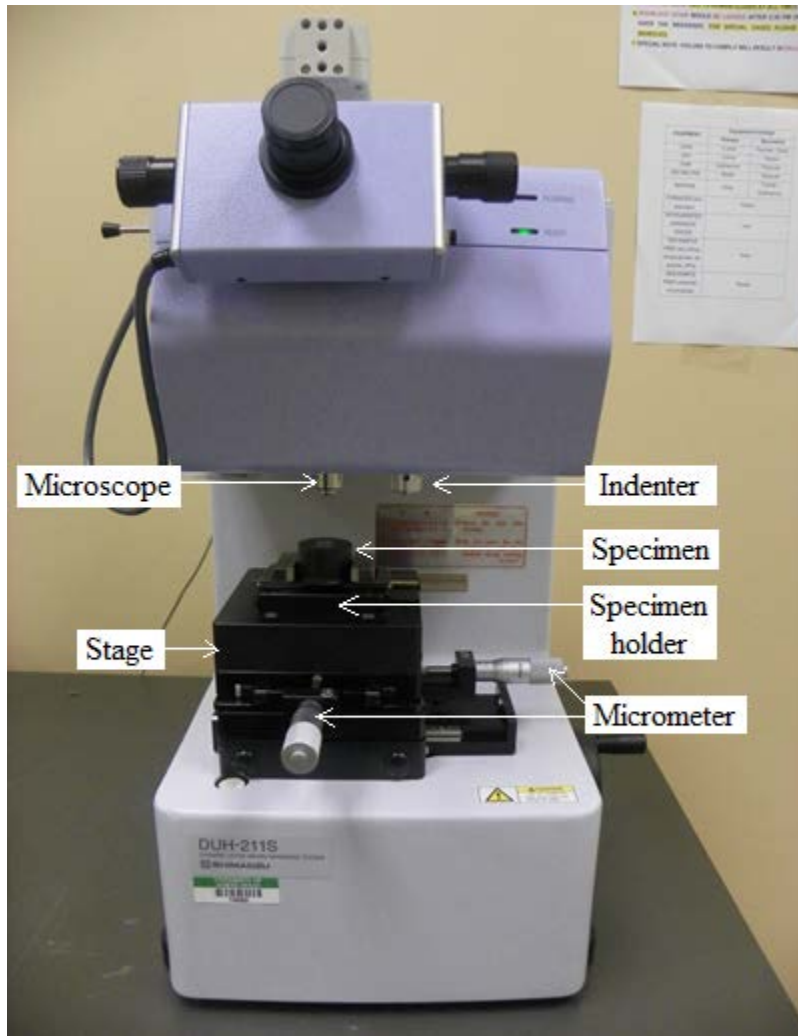


Figure 12: Shimadzu dynamic ultra micro hardness tester.

Indents were made at an increment of $10\ \mu\text{m}$ upto the bulk of the material as shown in figure 13. Adequate spacing of $50\ \mu\text{m}$ was kept between two indents to avoid any possible

alteration in readings due to the deformation caused by the earlier indent. Gradient in the hardness values was reported.

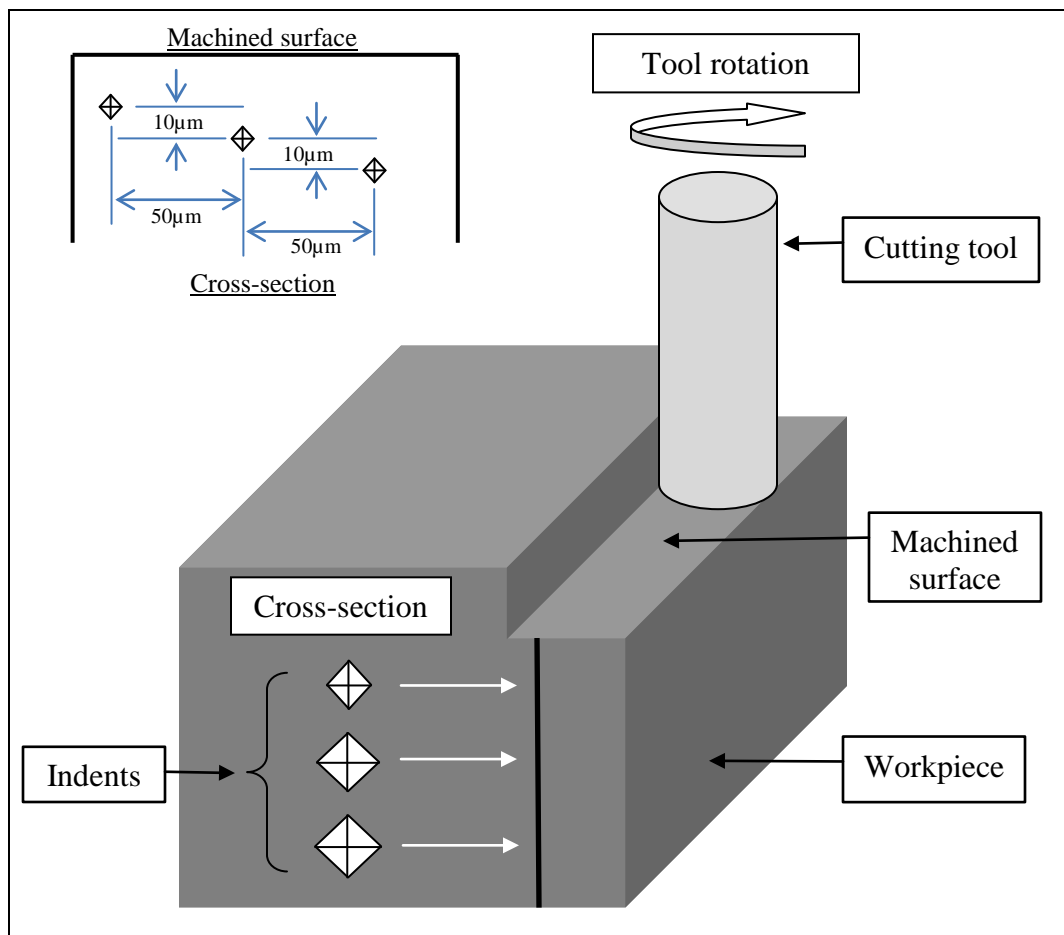


Figure 13: Schematic of vickers hardness measurements.

Bakelite mounts as shown in figure 14, were made to make sure that the material does not bulge out while taking the readings near to the edge of the cross-sectional machined surface.

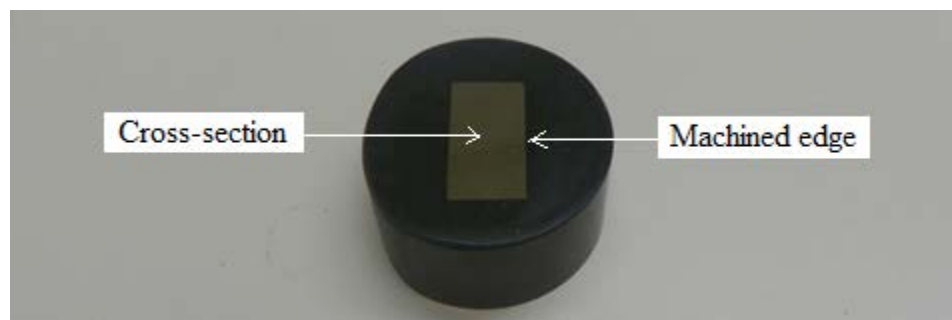


Figure 14: Bakelite mount.

Bearing Area Curve Measurement

A Nanovea non-contact optical profilometer was used to get the bearing area curve (BAC). The optical profilometer is shown in figure 15. BAC is a statistical method to represent the machined surface topography. It was introduced by Abbott and Firestone in 1933. Hence, it is also called as ‘Abbott Curve’. The BAC can approximate the real contact area obtained from the surface profile. It is compiled by considering the fraction of surface profile intersected by an infinitesimally thin plane positioned above a datum plane. The intersect length with material along the plane is measured, summed together and plotted as a proportion of the total length. The obtained curve is an integral of the height probability density function and if the height distribution is Gaussian, then this curve is nothing else than the cumulative probability distribution function (CDF) (Stachowiak & Batchelor, 2005).

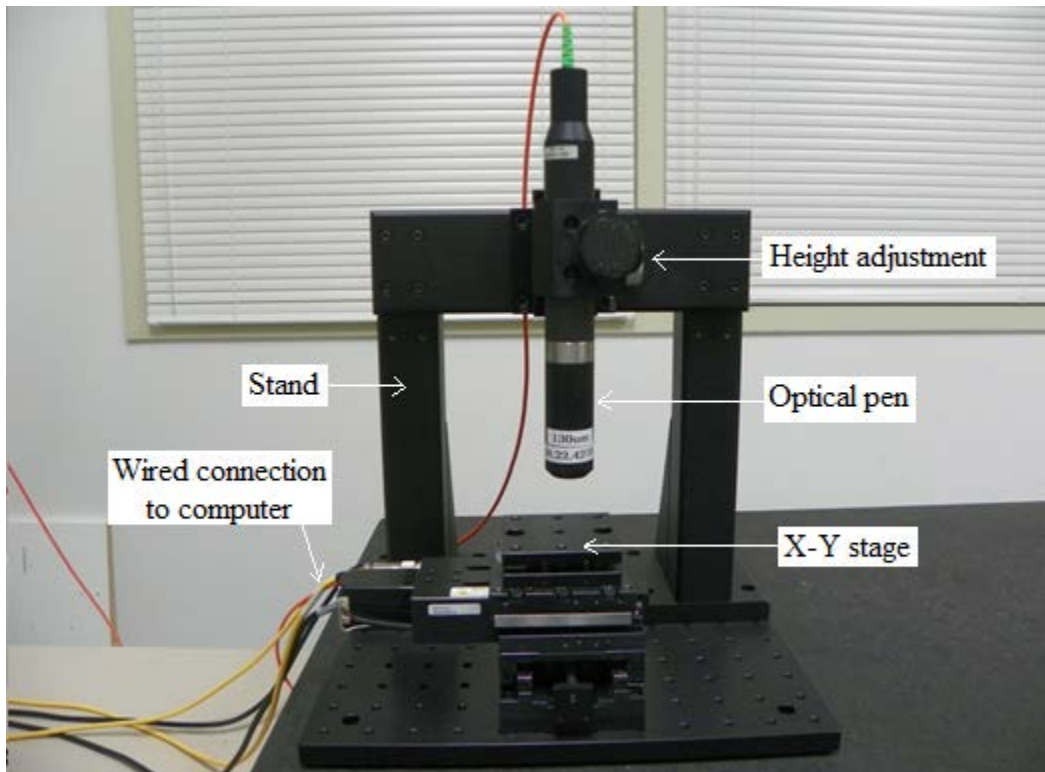


Figure 15: Nanovea non-contact optical profilometer.

The height distribution is constructed by plotting the number or proportion of surface heights lying between two specific heights as a function of the height.

Scanning Electron Microscopy (SEM) / Focused Ion Beam (FIB)

A dual beam Nova 200 NanoLab SEM/FIB was used to conduct the wear analysis of the cutting tool. It was also used to produce lift-outs of the cross-sectional machined area for further microstructural characterization to be done using transmission electron microscopy (TEM). The SEM/FIB is shown in figure 16. Quanta environmental SEM (ESEM) was used to do the wear analysis of the workpiece. The nova NanoSEM 230 was used to do the texture analysis.



Figure 16: Dual beam Nova 200 NanoLab SEM/FIB.

Electron Backscatter Diffraction (EBSD)

EBSD technique was carried out in the NanoSEM 230. EBSD is a SEM based microstructural crystallographic technique. In EBSD, an electron beam strikes a predetermined location on a tilted sample and the diffracted electrons form a pattern on a fluorescent screen. This pattern is characteristic of the crystal structure and orientation of the sample region from which it is generated. It provides the crystal orientation with sub-micron resolution down to ~ 50 nm (Oxford Instruments, 2013). The EBSD analysis was done to measure the grain size, phase mapping and potential grain texture. Electropolishing was done before mounting the samples for EBSD analysis. A solution containing 90% acetic acid and 10% perchloric acid was used for etching the surface for 300 seconds. Samples were then cleaned in an ultrasonicator and mounted on an SEM sample stub for EBSD analysis.

Transmission Electron Microscopy (TEM)

A Tecnai G² F20 TEM was used to do the subsurface deformation structural evolution analyses of the machined cross-sectional area. The TEM is shown in figure 17 (a). Electron transparent samples were made in SEM/FIB after attaching them on a Cu grid. The Cu grid are inserted into the TEM sample holder. High energy electrons are transmitted having very small wavelength (i.e., 0.025Å) through the sample to image the microstructure of the material with high resolution. Line defects, interfaces, grain boundaries, morphologies, crystallographic phases and defects can be observed using TEM.



Figure 17 (a): Tecnai G² F20 TEM.

Dislocation Density Quantification Procedure

The dislocation density was calculated by the line intersection method (Roy et al. 2006) which was based on the superimposition of the grid consisting of the horizontal and vertical lines on a TEM micrograph containing dislocations. The magnitude of the total length of the horizontal ($\sum L_h$) and vertical ($\sum L_v$) test lines were determined from the test grid, while the thickness (t) of the TEM specimen was determined by the convergent beam electron diffraction (CBED) method (Williams & Carter, 2009). When exactly on a two-beam condition, the transmitted undiffracted beam (000) - disc usually contains concentric diffuse fringes known as Kossel-Mollenstedt (K-M) fringes. The number of fringes increases by one every time the

thickness increases by one extinction distance. The thickness measurements are not made under the zone axis but under two beam conditions with only one strongly excited (hkl) reflection. The CBED will contain parallel instead of concentric intensity oscillations (Liao, 2006) as shown in figure 17 (b).

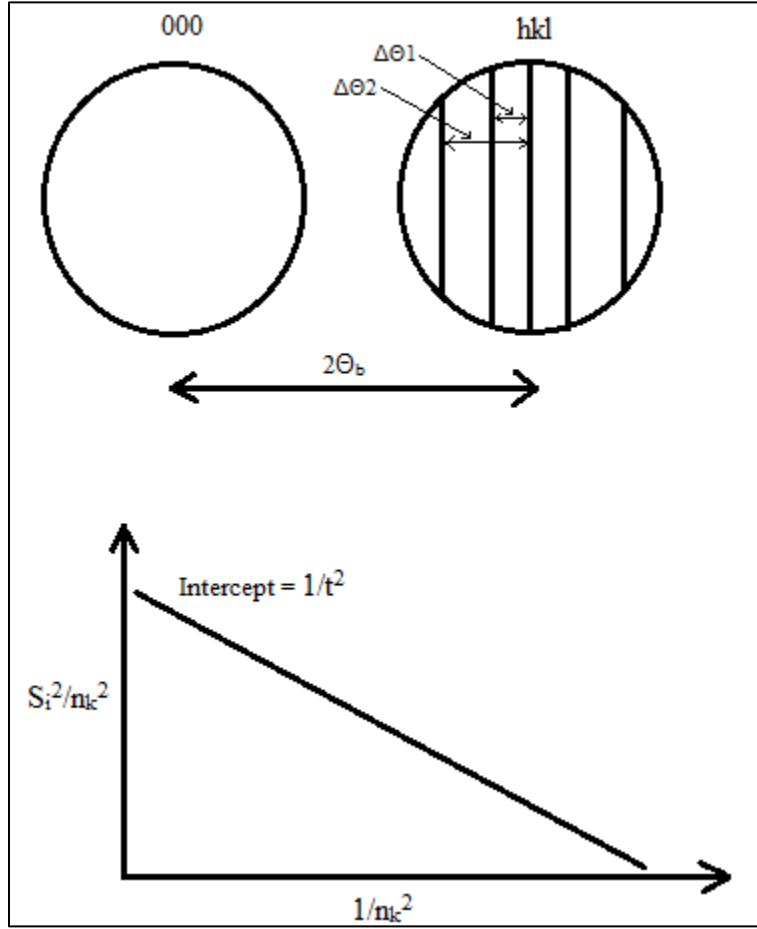


Figure 17 (b): Necessary measurements to extract thickness (t) from K-M fringes.

The central bright fringe is in exact Bragg condition. The fringe spacing corresponds to angle $\Delta\Theta_i$ and from this spacing the deviation s_i for i^{th} fringe can be determined using Eq. 1.

$$s_i = \lambda \frac{\Delta\Theta_i}{2\Theta_b d^2} \quad (1)$$

where,

λ = wavelength of the incident electron

Θ_b = the Bragg angle for the diffracting (hkl) plane

d = the (hkl) interplanar spacing

If the extinction distance ξ_g is known, the foil thickness (t) can be determined according to Eq. 2,

$$\frac{s_i^2}{n_k^2} + \frac{1}{\xi_g^2 n_k^2} = \frac{1}{t^2} \quad (2)$$

where,

n_k = integer

If the extinction distance is not known, then a graphical method is used to plot the measurements for several fringes as follows (Williams & Carter, 2009):

- Arbitrarily assign the integer $n = 1$ to the first fringe to an excitation error s_i .
- Then assign $n = 2$ to the second fringe, s_2 , etc.
- Plot $(s_i/n_k)^2$ versus $(1/n_k)^2$. If the result is a straight line, the arbitrary assignment was good.
- If the plot is a curve, then repeat the procedure by re-assigning $n = 2$ to the first fringe.
- Continue to iterate until you find a straight line as shown in figure 17 (b)

After calculating the foil thickness, the dislocation density (ρ) was calculated by using Eq. 3.

$$\rho = \frac{1}{t} \left(\frac{\sum n_v}{\sum L_v} + \frac{\sum n_h}{\sum L_h} \right) \quad (3)$$

where,

$\sum n_v$ = number of intersections of vertical test lines with the dislocations

$\sum n_h$ = number of intersections of horizontal test lines with the dislocations

$\sum L_v$ = total length of vertical test lines

$\sum L_h$ = total length of horizontal test lines

Assumptions of the Study

1. Any lack of rigidity in the machine tool and set up did not affect the data in the study.
2. Position of the mister nozzle and the flow rate was consistently same throughout the study.
3. Use of the toolmaker's microscope, DataRam4 and the vickers hardness tester was consistent throughout the study.
4. Tool flank wear was an appropriate indicator of tool life.
5. MANOVA was the appropriate statistical technique used for the analysis.
6. All the cutting tools and coatings used in the study were identical in composition.
7. The as-received workpiece material composition was homogeneous.

CHAPTER 4

RESULTS AND ANALYSES

This chapter includes the results of multivariate analysis of variance (MANOVA), tool-workpiece interface temperature analysis, tool life, wear mechanisms, cross-sectional hardness analysis at failure, transmission electron microscopy (TEM) analysis at failure, dislocation density quantification and electron backscattered diffraction (EBSD) analysis.

MANOVA

Minitab 16 statistical software was used for the MANOVA analysis. The flank wear side 1, side 2, aerosol mass concentration and aerosol particle size data was first checked for the MANOVA assumptions. The homogeneity of covariance was determined using Bartlett's test and Levene's test at 95% confidence level. The results are shown in Figures 18, 19, 20 and 21 for flank wear side 1, side 2, aerosol mass concentration and aerosol particle size, respectively. The p-values of Bartlett and Levene's test for all the dependent variables are significant indicating that they meet the equality of covariance assumption. Figures 22, 23, 24 and 25, show plots of residual versus fitted values which were used to test the assumption of constant variance for flank wear side 1, side 2, aerosol mass concentration and aerosol particle size. To fulfill the test, these plots should be a random scatter. The constant variance in the data demonstrates that the data does not follow a particular pattern, indicating constant variance.

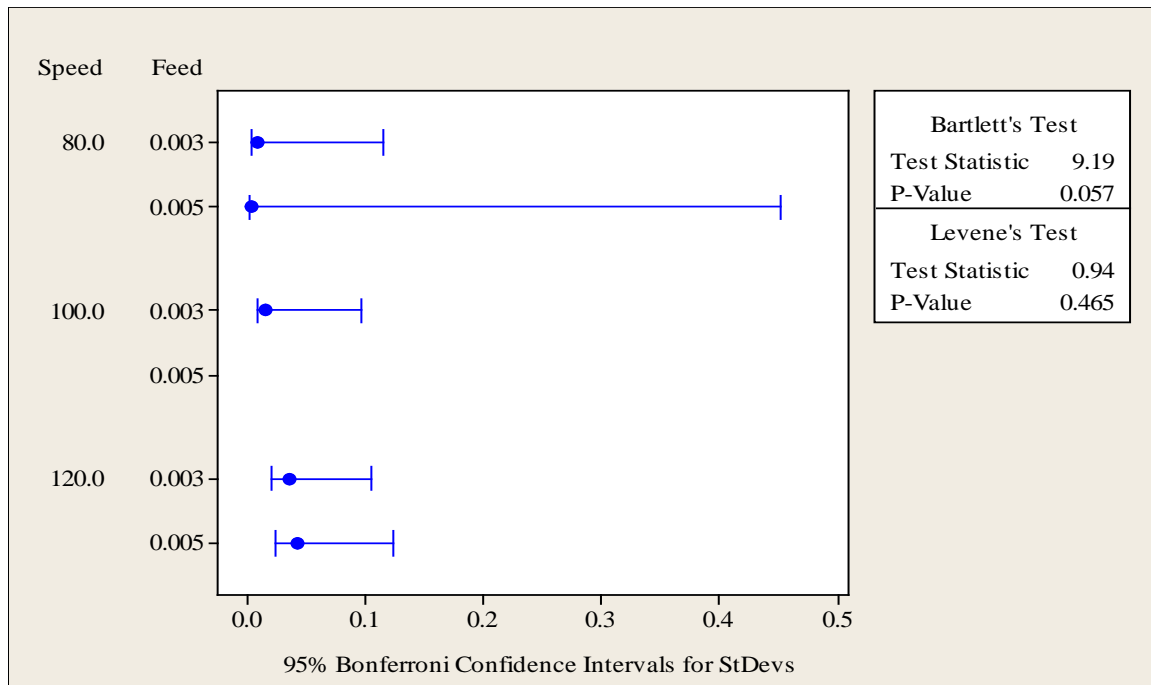


Figure 18: Test for equal covariance for flank wear side 1.

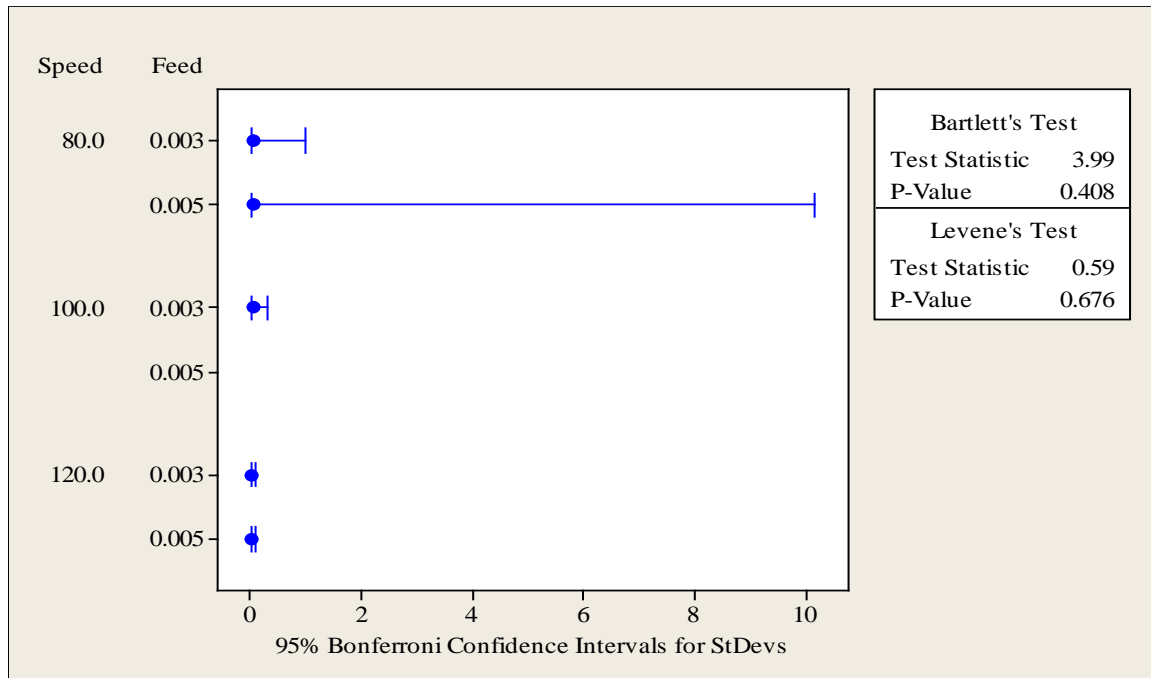


Figure 19: Test for equal covariance for flank wear side 2.

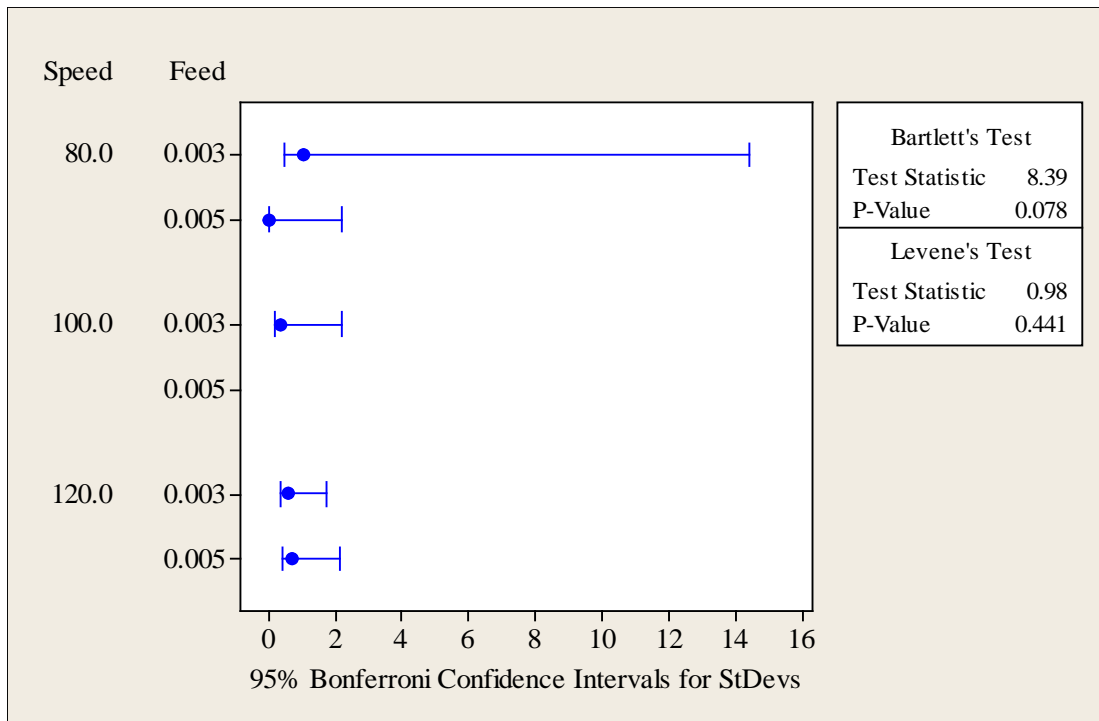


Figure 20: Test for equal covariance for aerosol mass concentration.

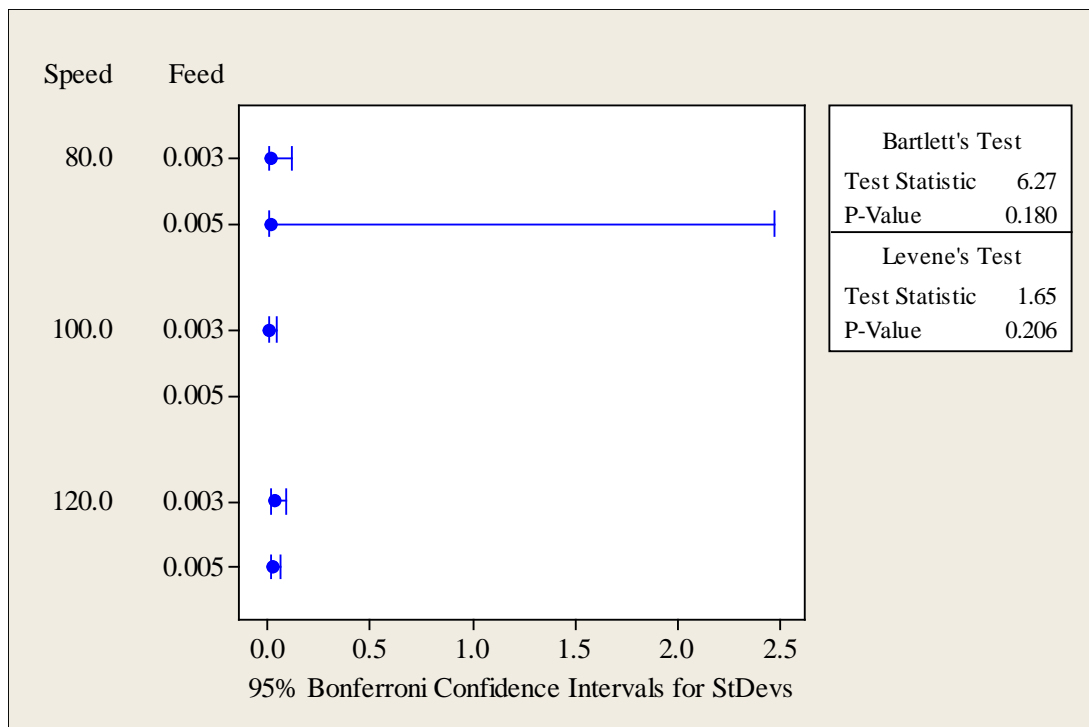


Figure 21: Test for equal covariance for aerosol particle size.

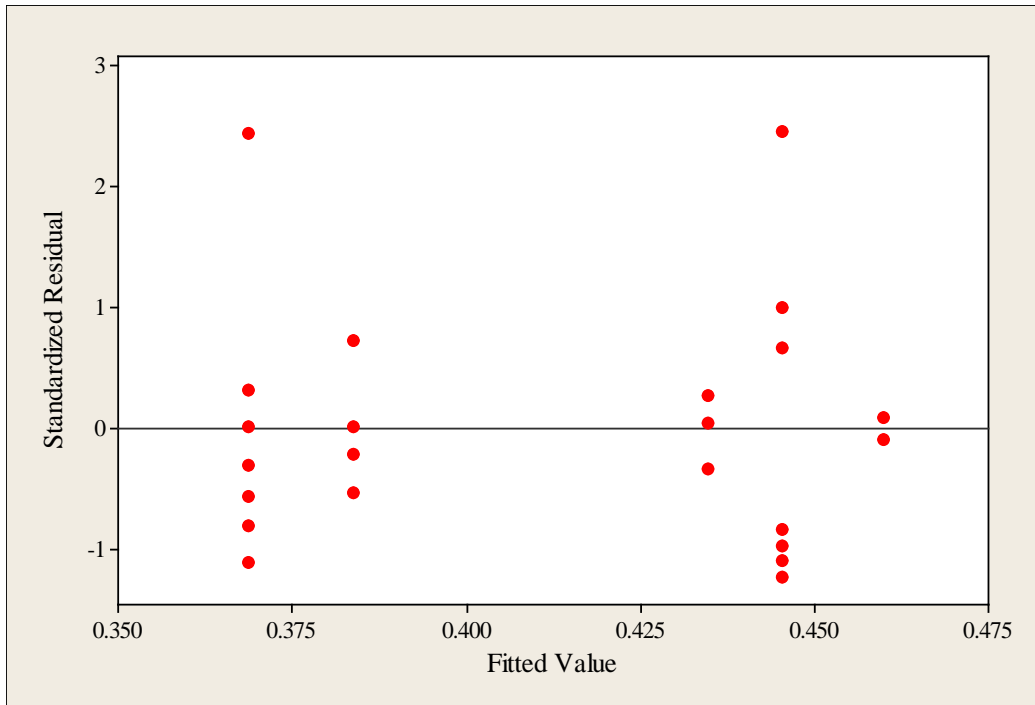


Figure 22: Constant variance in data for flank wear side 1.

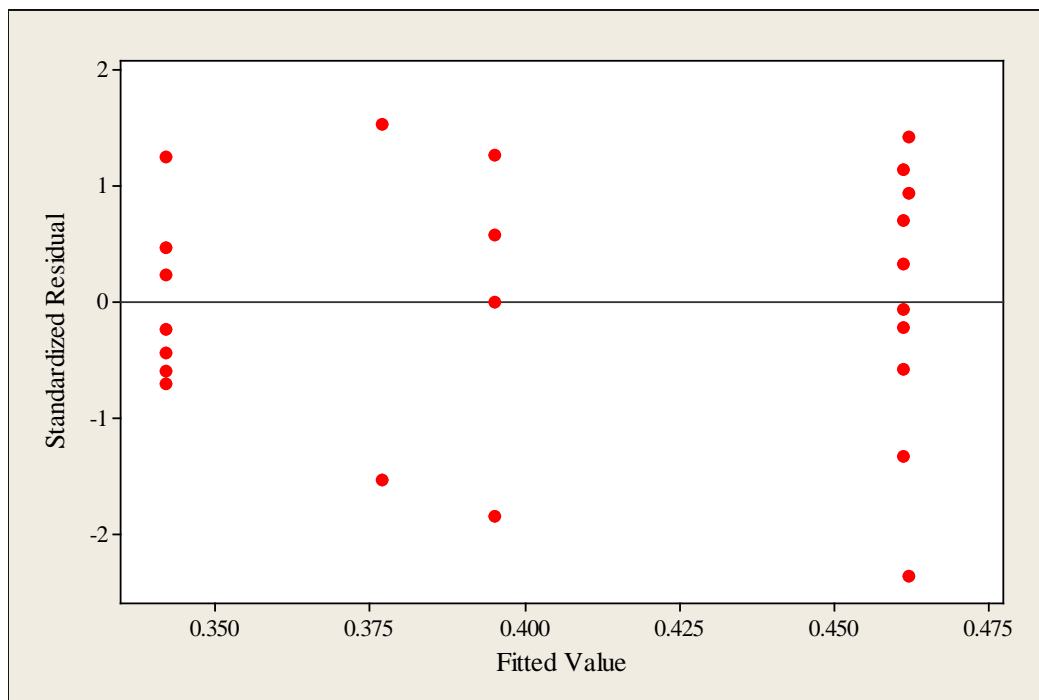


Figure 23: Constant variance in data for flank wear side 2.

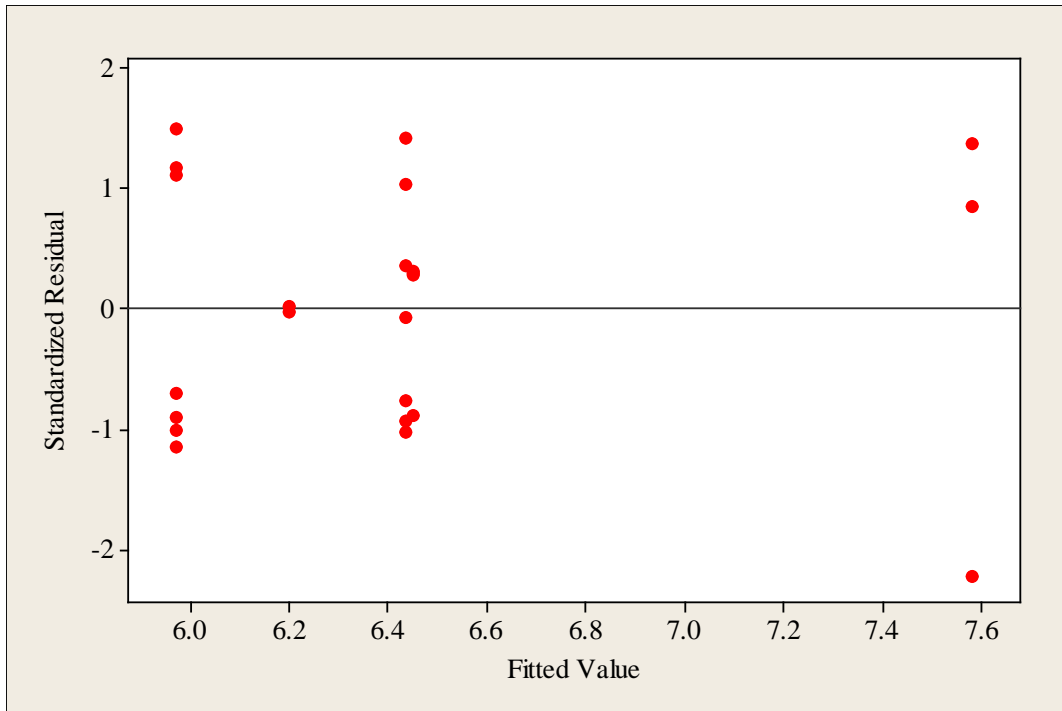


Figure 24: Constant variance in data for aerosol mass concentration.

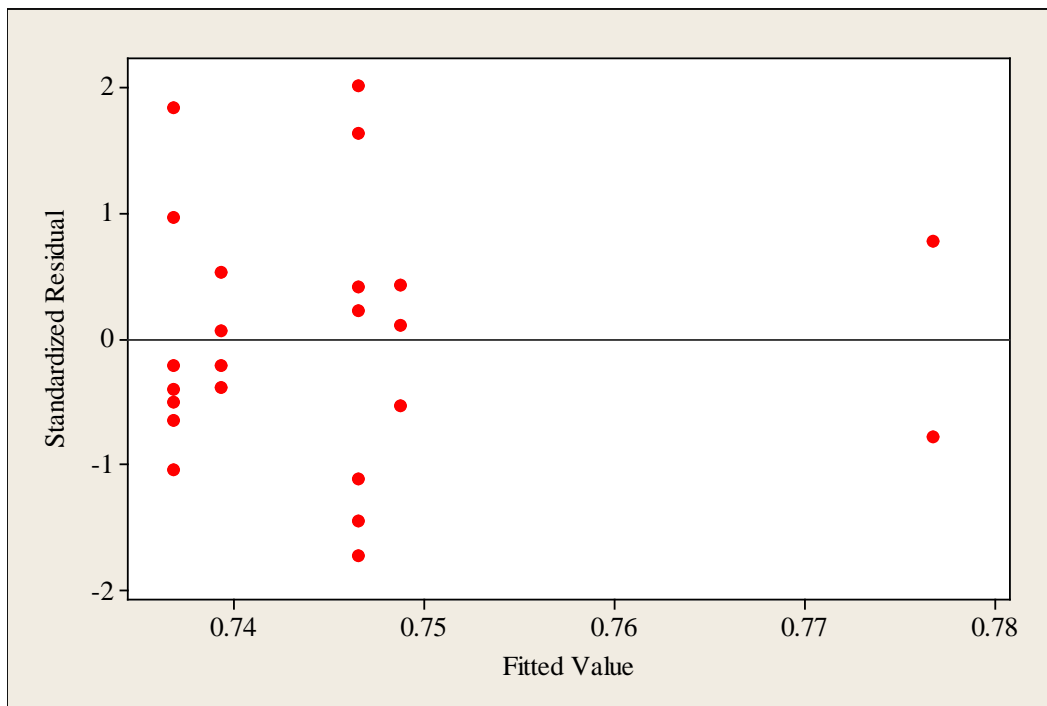


Figure 25: Constant variance in data for aerosol particle size.

Mahalanobis distance was used to test the data for multivariate normality. An observation is classified into a group if its Mahalanobis distance is the minimum. The outlier plot, as shown in figure 26 displays Mahalanobis distances for each observation. Points that fall above the y-axis reference line are outliers. There do not appear to be any outliers in the data.

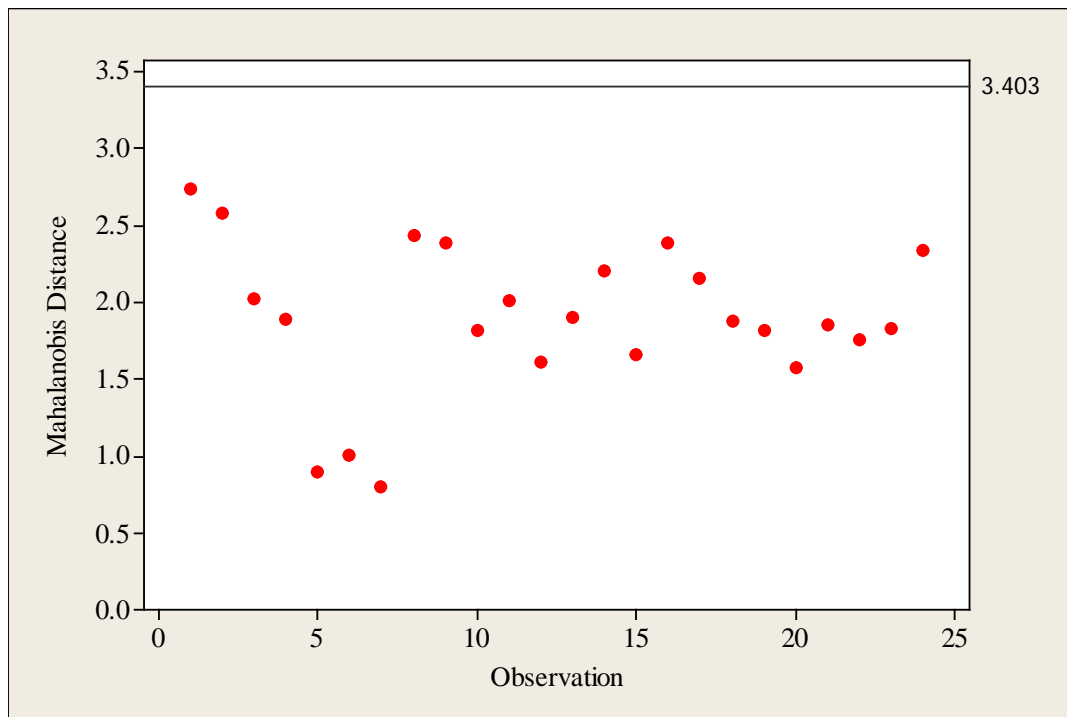


Figure 26: Mahalanobis distance for multivariate normality testing for flank wear side 1, side 2, aerosol mass concentration and aerosol particle size.

Data was also examined for univariate normality assumption for analysis of variances (ANOVA). A normal probability plot was used to determine if the distribution of data approximates a normal distribution. In the ANOVA, the normal probability plot is usually more effective and straightforward when it is done with residuals. The normal probability plot of residuals for flank wear side 1, side 2, aerosol mass concentration and aerosol particle size is shown in figures 27, 28, 29 and 30. The residual is the difference between the actual and predicted response values. The normal probability plot with a general straight line pattern indicates that the residuals follow a normal distribution. The far points which are slightly

scattered do not follow any significant pattern. The ANOVA is said to be robust for the normality assumption.

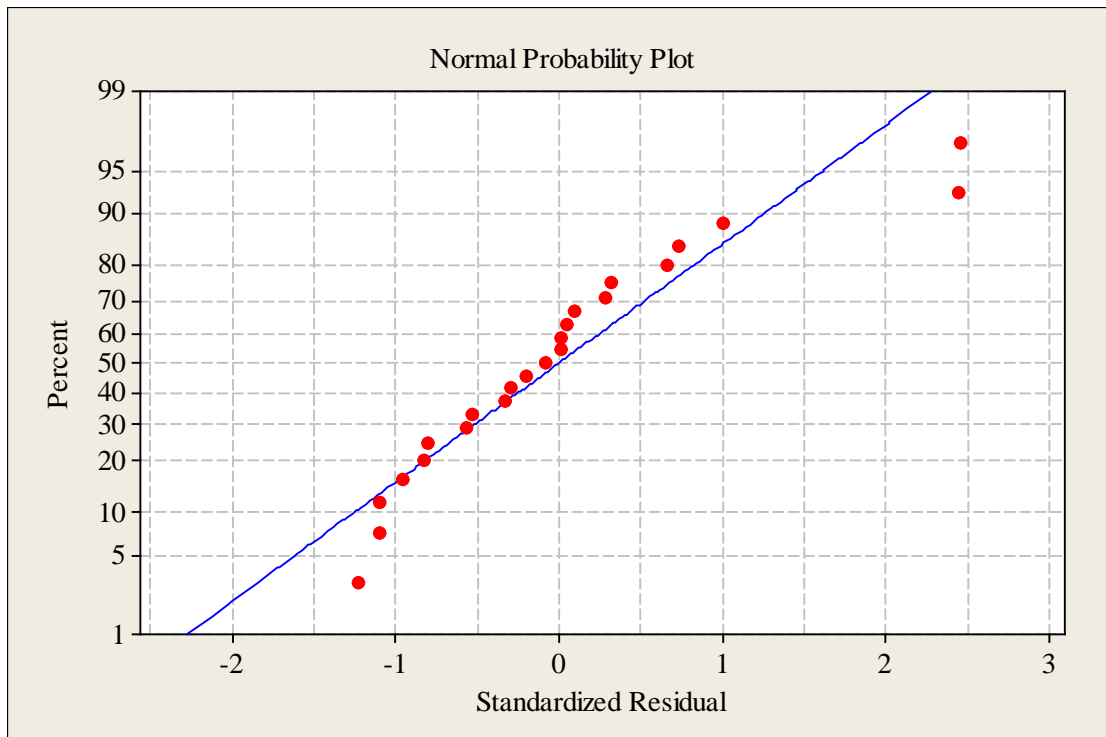


Figure 27: Normal plots of residual in data for flank wear side 1.

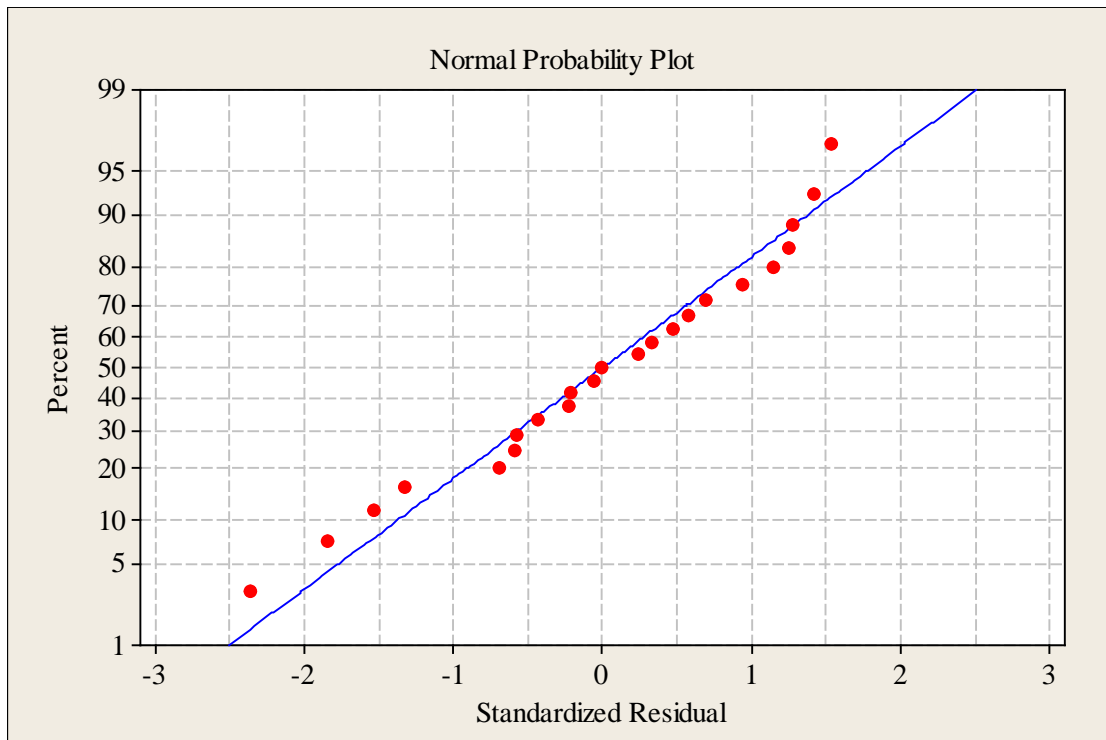


Figure 28: Normal plots of residual in data for flank wear side 2.

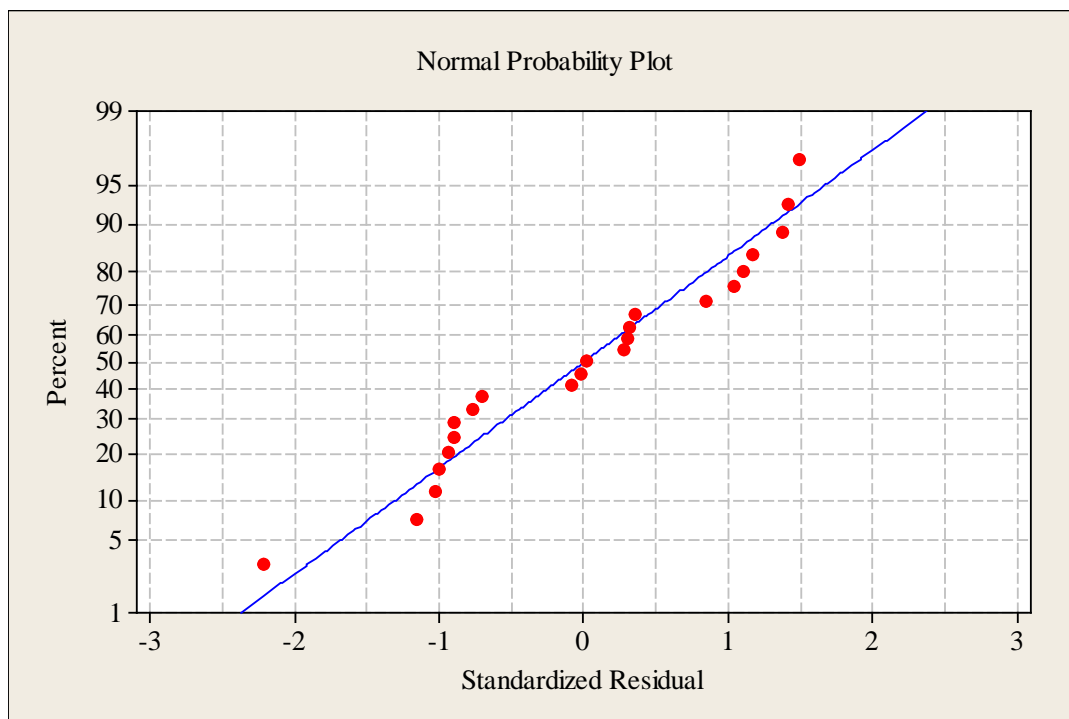


Figure 29: Normal plots of residual in data for aerosol mass concentration.

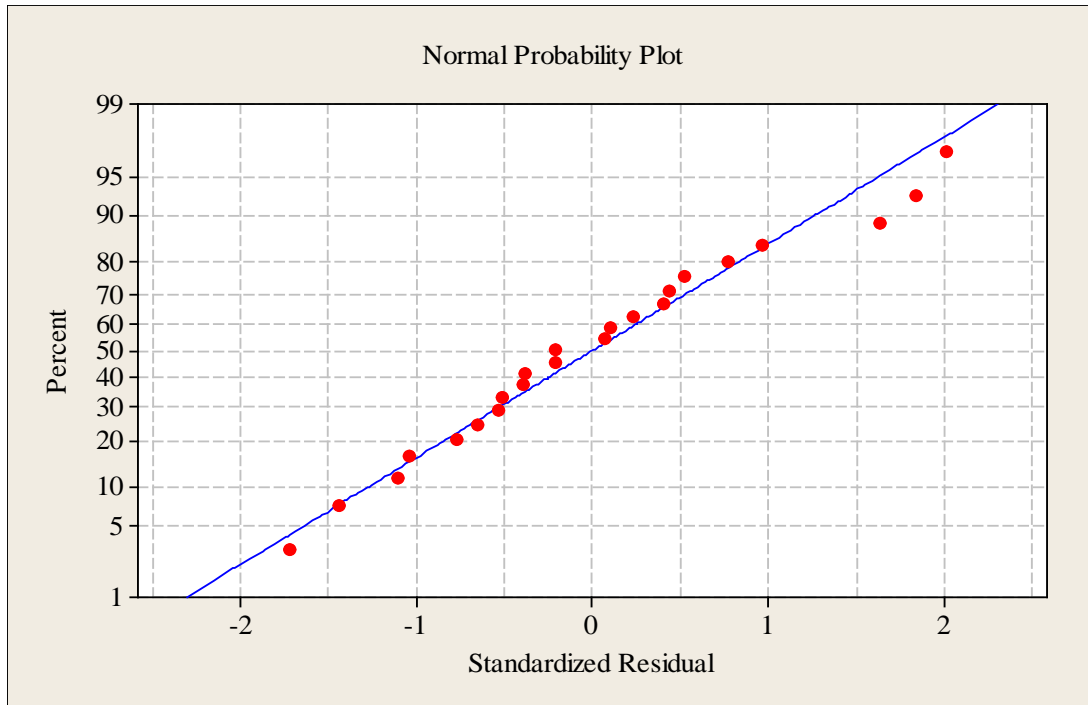


Figure 30: Normal plots of residual in data for aerosol particle size.

The MANOVA results are shown in table 7. The MANOVA model selected gave the main factors effects and the 2-way interaction effects.

Table 7: MANOVA test summarized results.

General Linear Model (MANOVA)							
Source	Criterion	Test Statistics	F Value	Numerator DF	Denominator DF	p-value	Result
Speed	Pillai's	0.90714	3.320	8	30	0.007	Significant
Feed	Pillai's	0.89738	32.793	4	15	0.000	Significant
Speed*Feed	Pillai's	0.55631	1.541	8	32	0.182	Not Significant

The model gave an F-value of 3.32, 32.79 and 1.54 for speed, feed and the interaction of (speed*feed), respectively. A significant effect is one that has a probability of occurrence (i.e. p-value) less than or equal to 0.05. Table 7 indicates that the speed and feed variables main effects are significant at 95% confidence level. But, the interaction of (speed*feed) was not significant at 95% confidence level. Univariate ANOVA was performed to determine which of the dependent variables were significantly affected by the independent variable. Tables 8, 9, 10 and

11 shows ANOVA for flank wear side 1, side 2, aerosol mass concentration and aerosol particle size, respectively. The prediction equations in the ANOVA are interpolative.

Table 8: ANOVA test for flank wear side 1.

Source	DF	Seq SS	Adj SS	Adj MS	F-value	P-value	
A-Speed	2	0.005377	0.009149	0.004574	4.47	0.026	Significant
B-Feed	1	0.030370	0.024171	0.024171	23.64	0.000	Significant
Speed*Feed	2	0.006068	0.006068	0.003034	2.97	0.077	Not Significant
Error	18	0.018407	0.018407	0.001023			
Total	23	0.060222					
Regression Equation: Flank Wear Side 1 = $0.5858 - (0.0029 \times A) - (12.1741 \times B) + (0.4530 \times A \times B)$							

Table 9: ANOVA test for flank wear side 2.

Source	DF	Seq SS	Adj SS	Adj MS	F-value	P-value	
A-Speed	2	0.004997	0.005418	0.002709	1.57	0.235	Not Significant
B-Feed	1	0.058103	0.028873	0.028873	16.76	0.001	Significant
Speed*Feed	2	0.002991	0.002991	0.001496	0.87	0.437	Not Significant
Error	18	0.031014	0.031014	0.001723			
Total	23	0.097105					
Regression Equation: Flank Wear Side 2 = $0.3448 + (0.0022 \times A) + (18.2723 \times B) - (0.6013 \times A \times B)$							

Table 10: ANOVA test for aerosol mass concentration.

Source	DF	Seq SS	Adj SS	Adj MS	F-value	P-value	
A-Speed	2	2.5050	1.6952	0.8476	2.04	0.159	Not Significant
B-Feed	1	2.2500	1.9248	1.9248	4.63	0.045	Significant
Speed*Feed	2	0.8685	0.8685	0.4343	1.04	0.372	Not Significant
Error	18	7.4843	7.4843	0.4158			
Total	23	13.1078					
Regression Equation: Aerosol mass concentration = $+19.71738 - (0.35725 \times A) - (51.57076 \times B) + (1.32848 \times A \times B)$							

Table 11: ANOVA test for aerosol particle size.

Source	DF	Seq SS	Adj SS	Adj MS	F-value	P-value	
A-Speed	2	0.0014795	0.0018448	0.0009224	2.30	0.129	Not Significant
B-Feed	1	0.0000021	0.0000878	0.0000878	0.22	0.646	Not Significant
Speed*Feed	2	0.0012818	0.0012818	0.0006409	1.60	0.230	Not Significant
Error	18	0.0072299	0.0072299	0.0004017			
Total	23	0.0099932					

The ANOVA for flank wear side 1 shown in table 8 indicates that the speed and feed variables main effects are statistically significant at 95% confidence level while the interaction of (speed*feed) is not statistically significant at 95% confidence level. The resulting model gave an R-squared value of 0.6944 indicating that it is able to predict 69.44% of the variation in the data. The remaining percent is considered noise and may not be predicted by this model. The sources of which may be manual variations while taking flank wear readings, machine vibrations, variations within the tools and workpiece materials.

The ANOVA for flank wear side 2 shown in table 9 indicates that the feed variable main effects is statistically significant at 95% confidence level while the speed variables main effect and the interaction of (speed*feed) are not statistically significant at 95% confidence level. The resulting model gave an R-squared value of 0.6806 indicating that it is able to predict 68.06% of the variation in the data. The remaining percent is considered noise and may not be predicted by this model. The sources of which may be the same as given for flank wear side 1. The units of the prediction equations for both the flank wear side 1 and 2 are in millimeters (mm).

It was observed that the cutting speed variable main effect for flank wear side 1 was statistically significant, while the cutting speed variable main effect for flank wear side 2 was statistically not significant. The reason behind these results is hypothesized to be the alternate use of up-milling and down-milling cut. As shown in the figure 31, it is always more favorable to apply down-milling rather than up-milling. When the cutting edge goes into contact in down-milling, the chip thickness has its maximum value, in up-milling the chip thickness is zero. The tool life is generally shorter in up-milling due to the fact that there is considerably more heat generated due to the rubbing action that takes place on the entry. The radial forces are also considerably higher in up-milling (Sandvik Coromant, 2007).

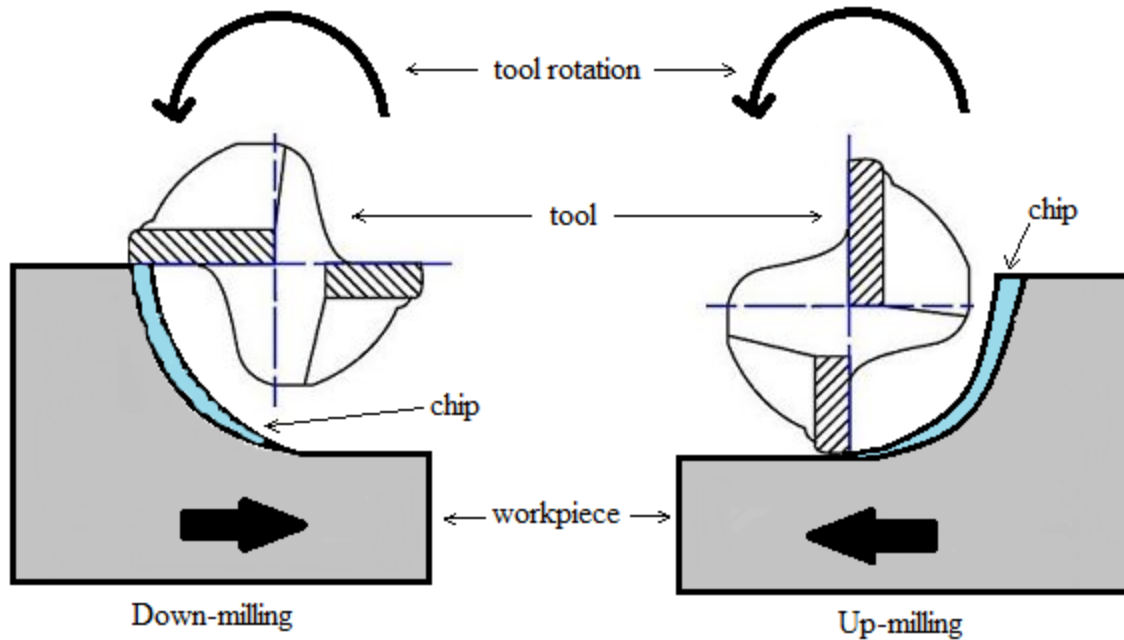


Figure 31: Down-milling (Climb milling) and Up-milling (Conventional milling).

The ANOVA for aerosol mass concentration shown in table 10 indicates that the feed variables main effects is statistically significant at 95% confidence level while the speed and the interaction of (speed*feed) is not statistically significant at 95% confidence level. The resulting model gave an R-squared value of 0.4290 indicating that it is able to predict 42.90% of the variation in the data. The remaining percent is considered noise and may not be predicted by this model. The sources of which may be length of the tygon tube, turbulence in aerosol flow due to unavoidable bends in the tygon tube, type of lubricant, lubricant delivery method, aerosol flow rate and/or nozzle position. Some of the other reasons may include logging time difference due to manually turning ON/OFF the exhaust pump and/or DataRam4 particulate monitor, and the slight difference in positioning of the tygon tube before starting each experiment. The ANOVA for aerosol particle size shown in table 11 indicates that the speed, feed variable main effects and the interaction of (speed*feed) are not statistically significant at 95% confidence level. The unit of the prediction equation for the aerosol mass concentration is in mg/m^3 .

Main effects plot and interaction plots were plotted from the results of the MANOVA and ANOVA analyses. Figures 32 and 33 show the main effects and the interaction plot for flank wear side 1. It was observed that the flank wear of side 1 decrease with the increase in speed and increase with the increase in feed. High speed of 120 surface feet per minute (SFM) and a low feed of 0.003 inches per tooth (IPT) were recommended to reduce flank wear of side 1. Figures 34 and 35 show the main effects and the interaction plot for flank wear side 2. It was observed that the flank wear of side 2 decrease with the increase in speed and feed. High speed of 120 SFM and a high feed of 0.005 IPT were recommended to reduce flank wear of side 2. It can be seen that the flank wear side 1 increased with the increase in feed rate. But the flank wear side 2 decreased with the increase in feed rate. The reason can be hypothesized that one flank wear side worn out faster than the other one. If the end mill was manufactured according to correct specifications and composition, flank wear should be similar on both the sides. The possible reason for uneven wear can be tool run-out. This can be caused by the holder and/or spindle. Tool run-out as shown in figure 36 is the result of a misalignment between the rotational axis of the cutting tool and the central axis of the collet/spindle system. The causes include poorly aligned central collet bore, improper alignment of the cutting tool in the tool holder, worn spindle taper, worn tool holder, and debris between the collet and spindle bore tapers (Ryu et al. 2006). These issues can be eliminated by measuring the tool run-out before starting each experiment using dial gauge. Excessive tool run-out results in chip load variation, tool deflection, cutting load changes, and uneven surface texture and flank wear. Sometimes higher depth of cut can also result in the deflection of cutting tool and uneven flank wear. Therefore, it is important to use a tool with a maximum core diameter and minimum cutting length to have higher bending stiffness.

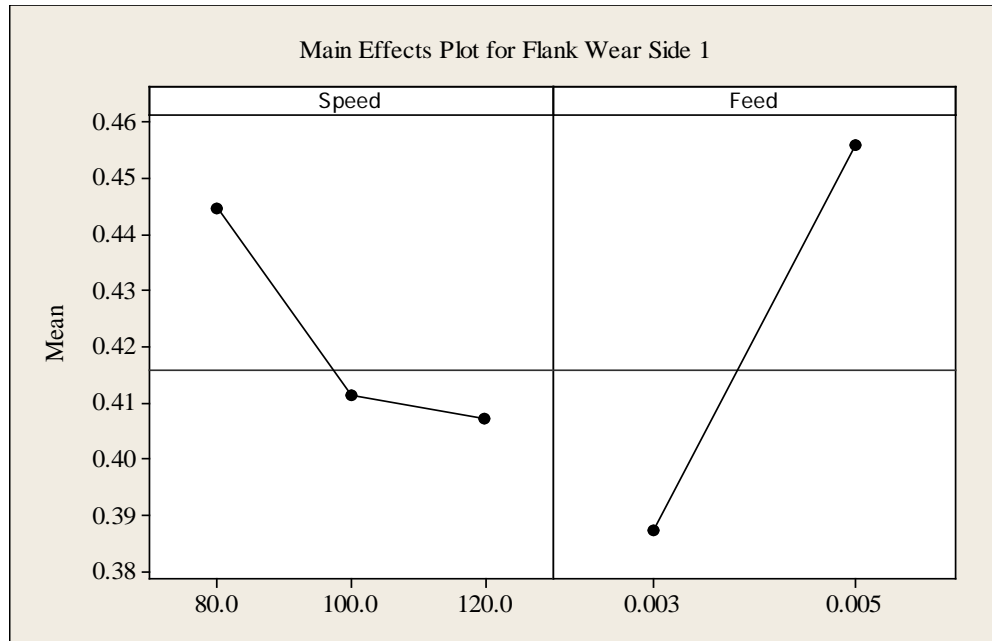


Figure 32: Main effect plot for flank wear side 1.

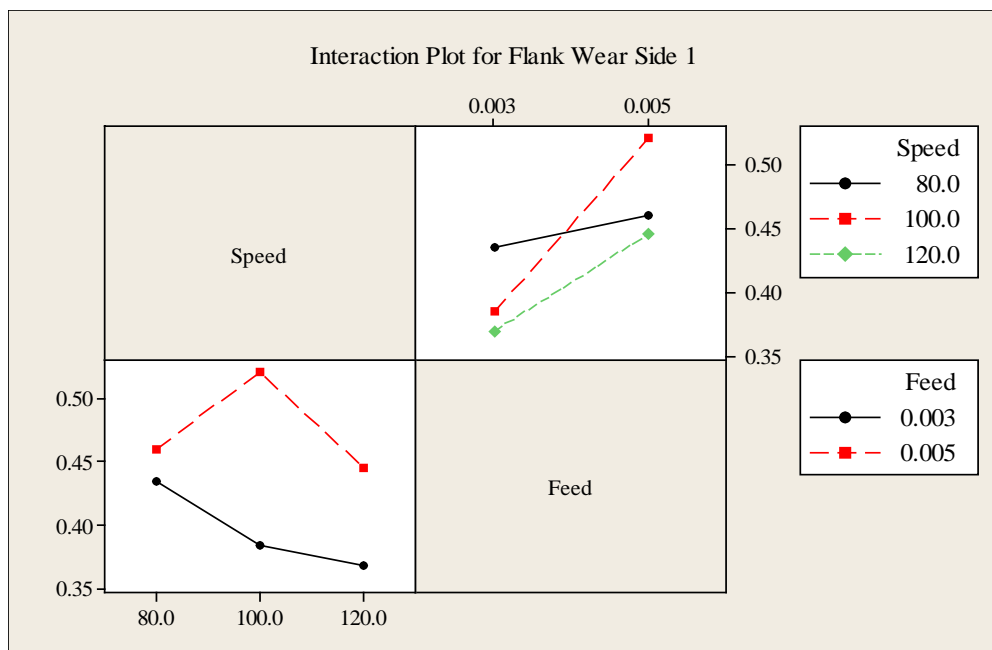


Figure 33: Interaction plot for flank wear side 1.

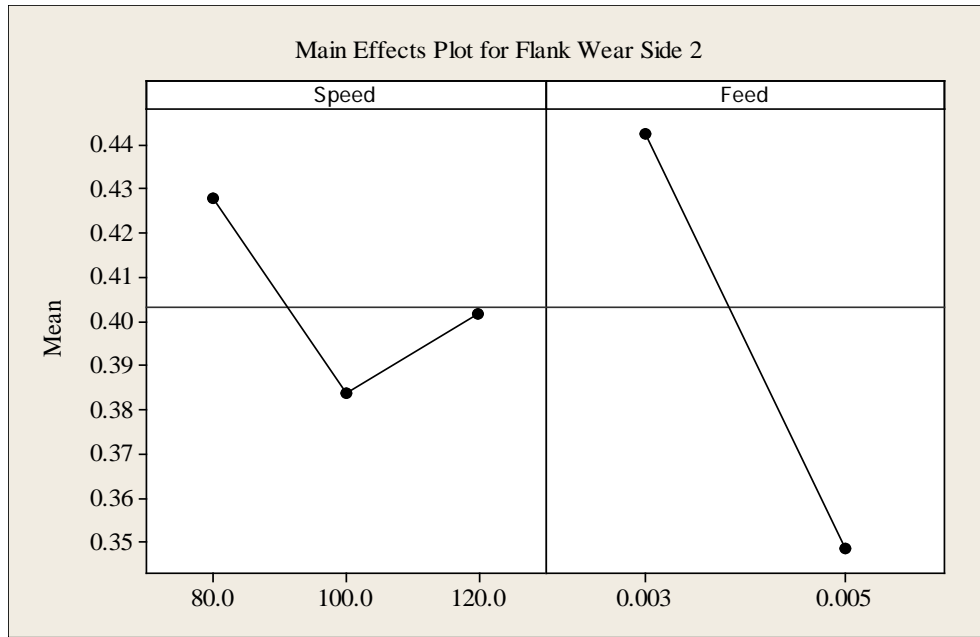


Figure 34: Main effect plot for flank wear side 2.

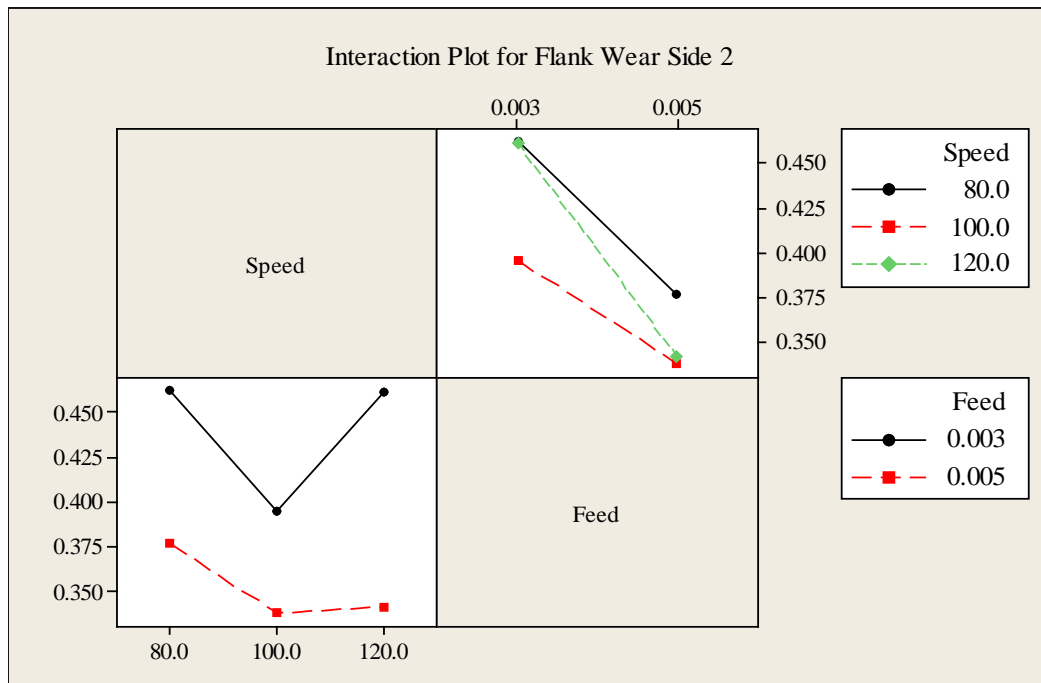


Figure 35: Interaction plot for flank wear side 2.

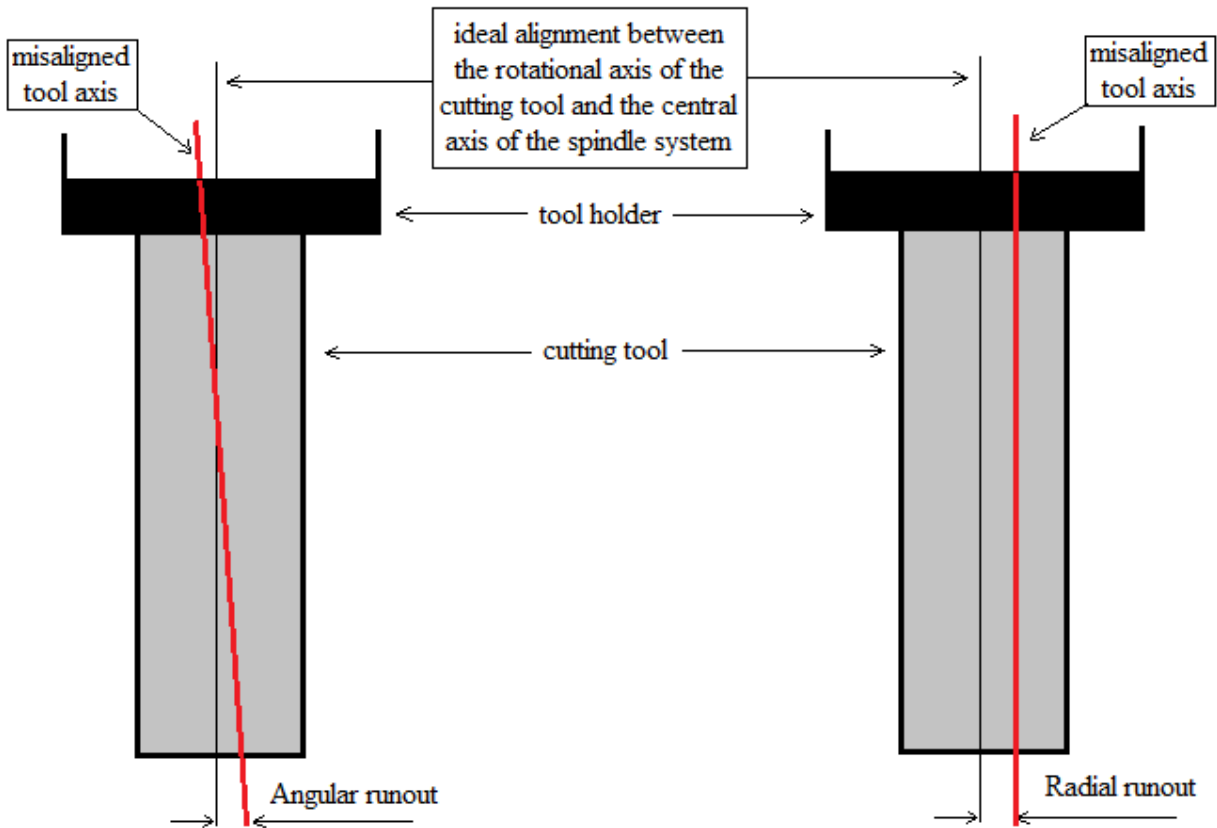


Figure 36: Tool run-out.

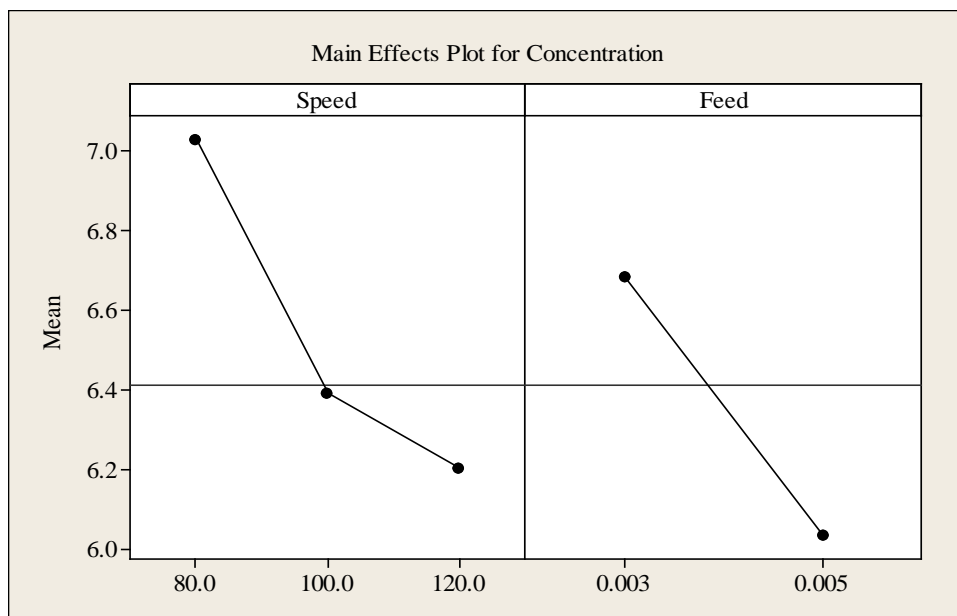


Figure 37: Main effect plot for aerosol mass concentration.

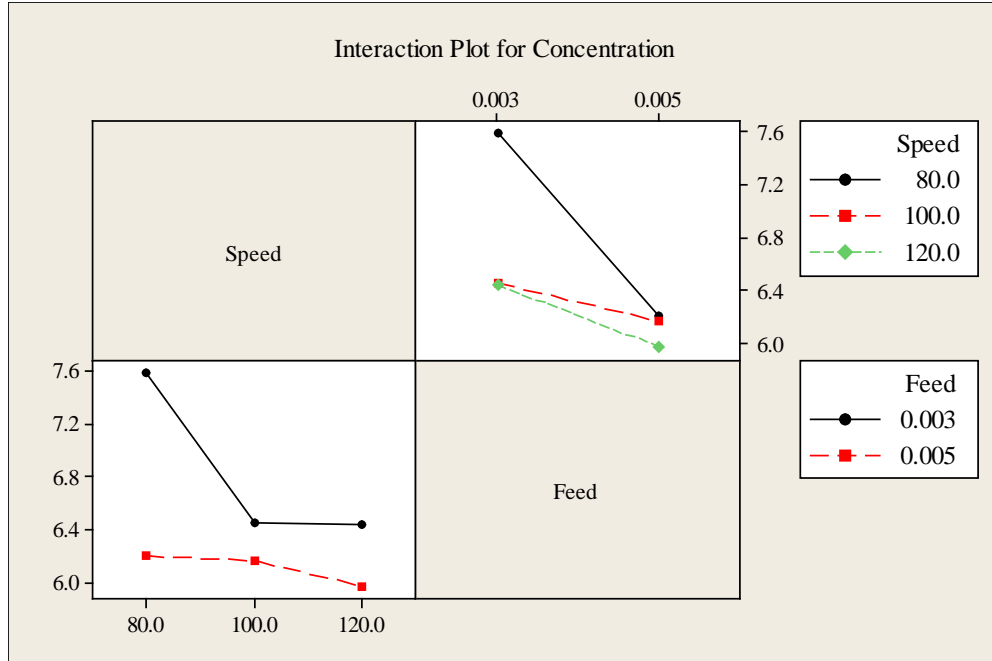


Figure 38: Interaction plot for aerosol mass concentration.

Figures 37 and 38 show the main effects and the interaction plot for aerosol mass concentration. It was observed that the aerosol mass concentration decreases with the increase in speed and feed. High speed of 120 SFM and a high feed of 0.005 IPT were recommended to reduce the aerosol mass concentration.

The parameter optimization was done by setting the goal to minimize flank wear side 1, side 2 and aerosol mass concentration. Design Expert 8 software was used to do the parameter optimization. Figures 39 and 40, show that there is 84.2% desirability to achieve a flank wear side 1 of 0.365 mm using a cutting speed of 120 SFM and a feed rate of 0.003 IPT. Figures 41 and 42, show that there is 60.7% desirability to achieve a flank wear side 2 of 0.380 mm using a cutting speed of 120 SFM and 0.0041 IPT. All the figures with optimization parameter show International System of Units (SI units).

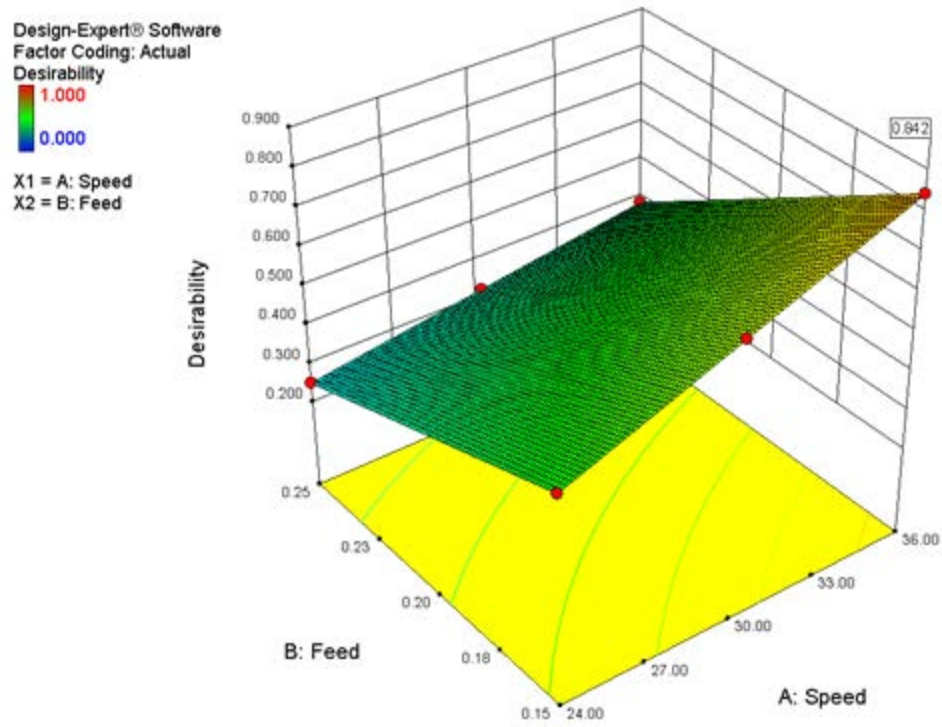


Figure 39: Desirability plot for flank wear side 1.

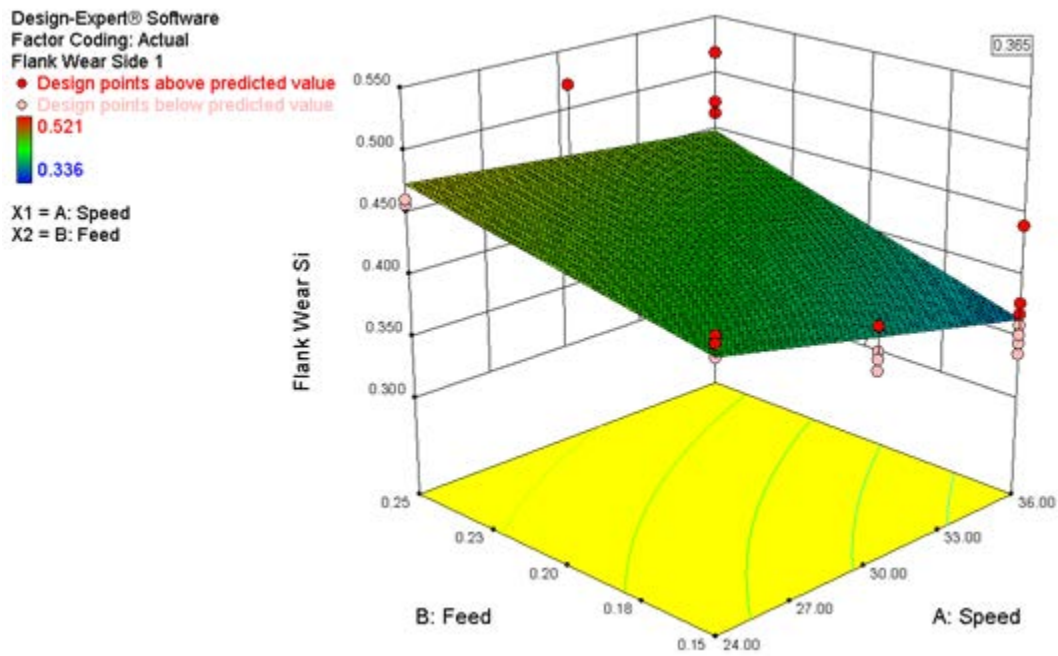


Figure 40: Selected solution plot for flank wear side 1.

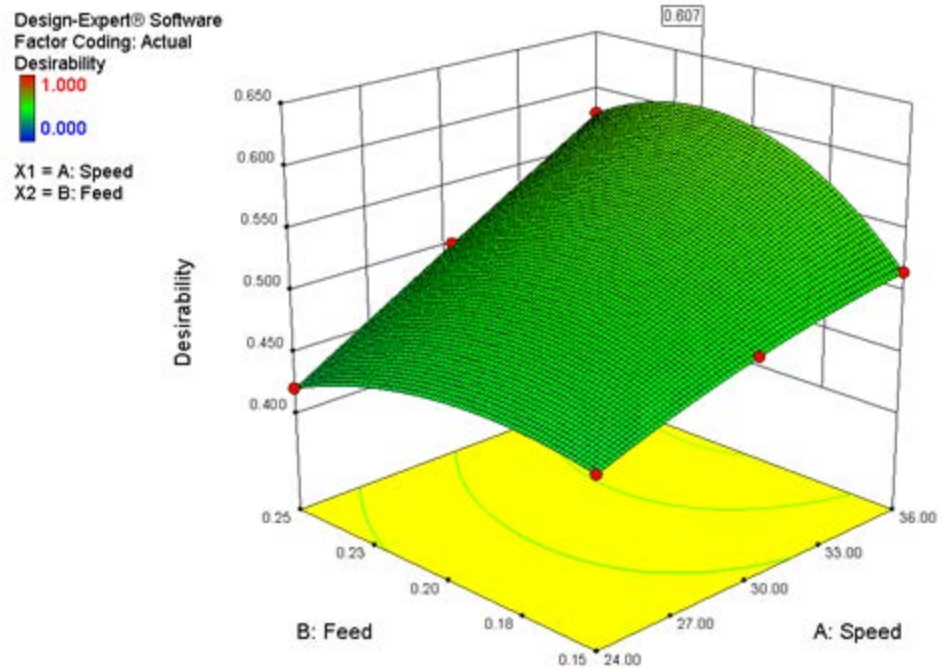


Figure 41: Desirability plot for flank wear side 2.

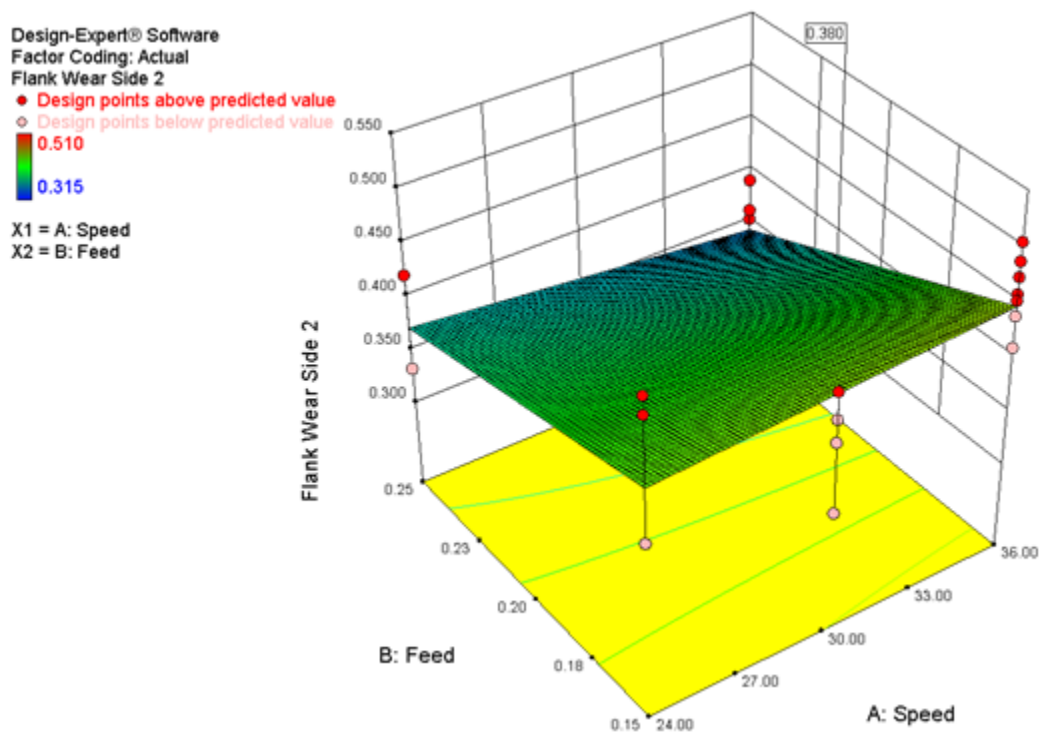


Figure 42: Selected solution plot for flank wear side 2.

Figures 43 and 44 show that there is 84.0% desirability to achieve a concentration of 5.91 mg/m³ using a cutting speed of 120 SFM and a feed rate of 0.005 IPT.

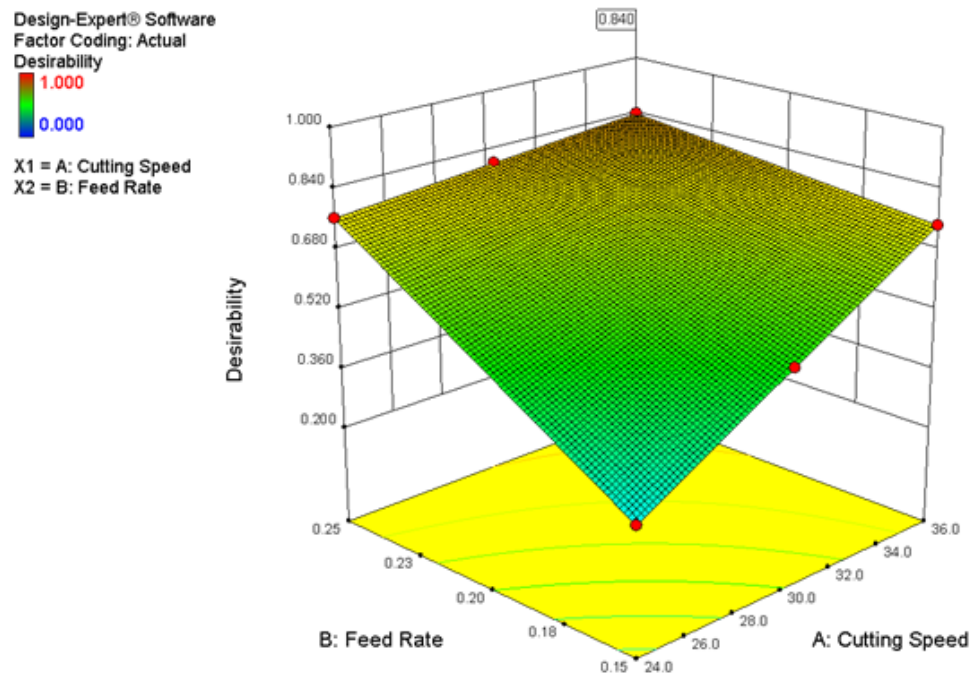


Figure 43: Desirability plot for aerosol mass concentration.

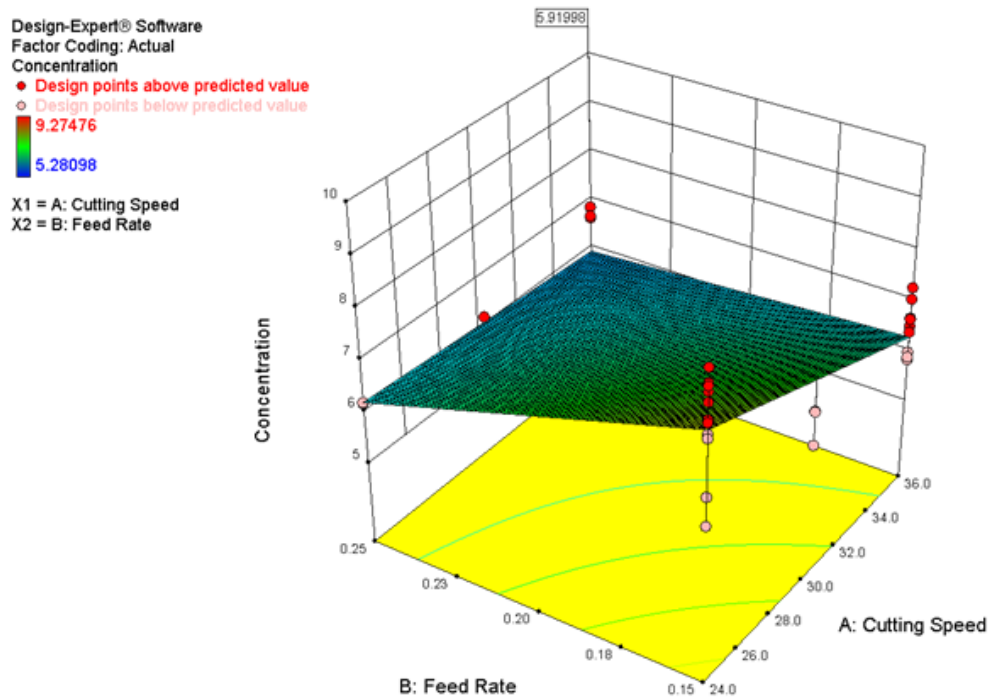


Figure 44: Selected solution plot for aerosol mass concentration.

Aerosol Mass Concentration and Aerosol Particle Size Analysis

Figures 45 and 46 show the average mass concentration and the average particle size, respectively, for different cutting speed and feed rate combinations. Machining with lower speed and feed rate combinations (i.e. 80 SFM and 0.003 IPT) resulted in the higher average mass concentration and machining with higher speed and feed rate combinations (i.e. 120 SFM and 0.005 mm/rev) resulted in the lower average mass concentration. The highest average mass concentration of 8.32 mg/m^3 was realized using treatment 80 SFM and 0.003 IPT. At low speed and feed rates it is hypothesized that atomization is dominant and plays a larger role in aerosol generation during the cutting process. The particles are less scattered resulting in higher mass concentration (Jayal et al. 2004). At low speeds and feeds, the resulting mist particles have less tendency to split, hence resulting in larger size particles as shown in figure 46. The lowest average mass concentration of 5.91 mg/m^3 was realized using treatment 120 SFM and 0.005 IPT. At high speed and feed rate it is hypothesized that vaporization/condensation are the dominant mechanisms for the generation of mist. At high speed and feed rate levels the resulting heat is partially transferred to the lubricant which vaporizes some of the mist particles. Hence a lower average mass concentration (Sutherland et al. 2000).

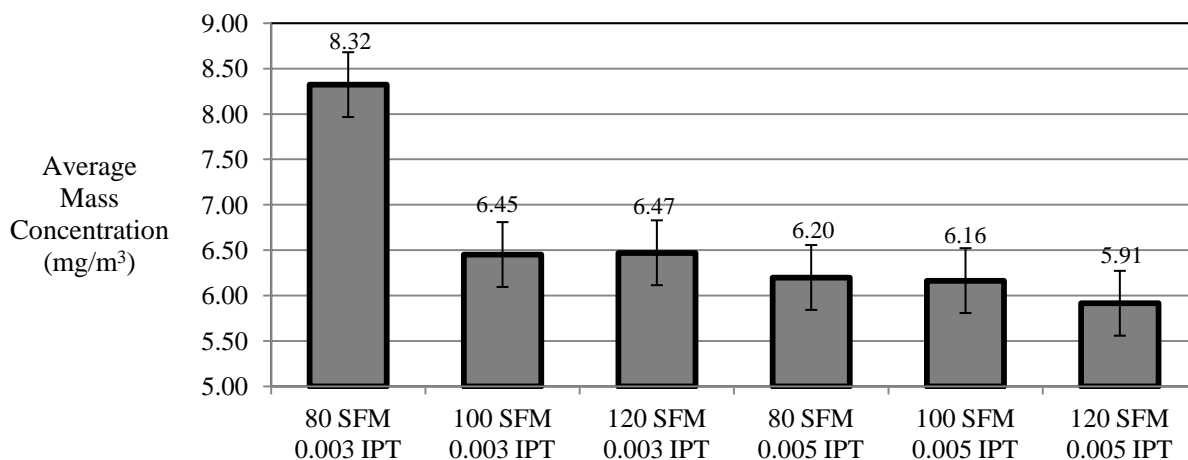


Figure 45: Average mass concentration for different cutting speeds and feed rates combinations.

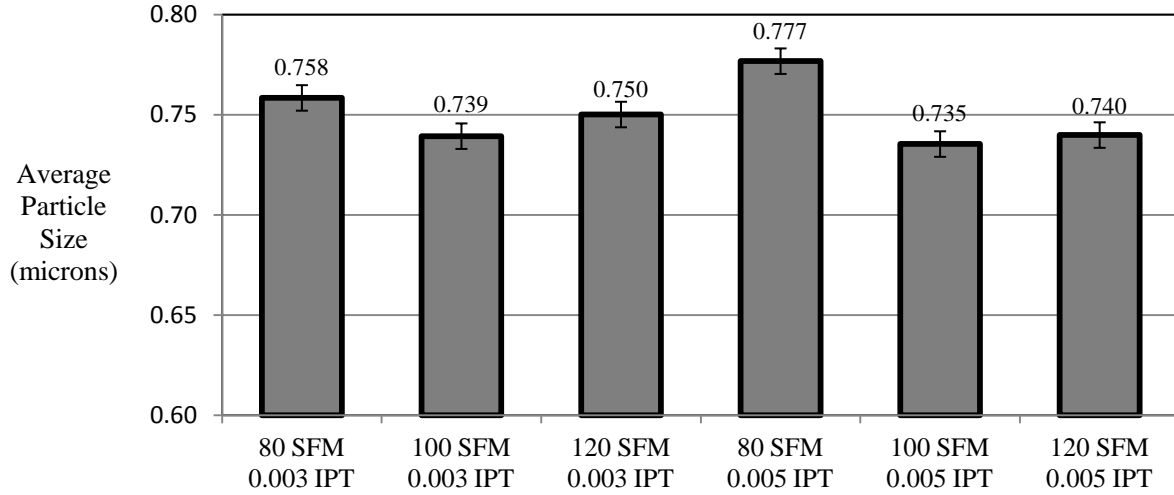


Figure 46: Average particle size for different cutting speeds and feed rates combinations

Tool-Workpiece Interface Temperature Analysis

The interface temperature between the cutting tool and the workpiece was calculated using Peclet numbers as described in chapter 3.

First, low cutting speed (i.e. 80 SFM) and low feed rate (i.e. 0.003 IPT) combination is considered. We will start our calculation by finding the values of R' , E' , a , $\chi_{\text{workpiece}}$ and χ_{tool} .

So,

$$R' = 1 / \{ (1/R_{\text{tool}}) + (1/R_{\text{workpiece}}) \}$$

here, $R_{\text{tool}} = 0.0254 \text{ m}$ and

$$R_{\text{workpiece}} = 0.1016 \text{ m}$$

$$\therefore R' = 1 / \{ (1/0.0254) + (1/0.1016) \}$$

$$\therefore \underline{R' = 0.02032 \text{ m}}$$

Also,

$$E' = 1 / \{ (1 - \nu_{\text{tool}}^2) / E_{\text{tool}} \} + \{ (1 - \nu_{\text{workpiece}}^2) / E_{\text{workpiece}} \}$$

here, $\nu_{\text{tool}} = 0.26$ $E_{\text{tool}} = 620 \text{ GPa}$

$$v_{\text{workpiece}} = 0.29 \quad E_{\text{workpiece}} = 205 \text{ GPa}$$

$$\therefore E' = 1 / \{ (1-0.26^2) / 620 \} + \{ (1-0.29^2) / 205 \}$$

$$\therefore \underline{E' = 1.6745 \times 10^{11} \text{ Pa}}$$

Also,

$$a = \left(\frac{4 W R'}{L \pi E'} \right)^2$$

$$\text{here,} \quad W = 5.6956 \text{ N} \quad L = 0.003175 \text{ m}$$

$$\therefore a = \left(\frac{4 * 5.6956 * 0.02032}{0.003175 * \pi * 1.6745 \times 10^{11}} \right)^2$$

$$\therefore \underline{a = 0.000016648 \text{ m}}$$

Also,

$$\chi_{\text{workpiece}} = \kappa / \rho \sigma$$

$$\text{here,} \quad \kappa_{\text{workpiece}} = 51.9 \text{ W/mK} \quad \rho_{\text{workpiece}} = 7870 \text{ kg/m}^3 \quad \sigma_{\text{workpiece}} = 486 \text{ J/kgK}$$

$$\therefore \chi_{\text{workpiece}} = 51.9 / 7870 * 486$$

$$\therefore \underline{\chi_{\text{workpiece}} = 1.356 \times 10^{-5} \text{ m}^2/\text{s}}$$

Also,

$$\chi_{\text{tool}} = \kappa / \rho \sigma$$

$$\text{here,} \quad \kappa_{\text{tool}} = 112 \text{ W/mK} \quad \rho_{\text{tool}} = 14600 \text{ kg/m}^3 \quad \sigma_{\text{tool}} = 340 \text{ J/kgK}$$

$$\therefore \chi_{\text{tool}} = 112 / 14600 * 340$$

$$\therefore \underline{\chi_{\text{tool}} = 2.256 \times 10^{-5} \text{ m}^2/\text{s}}$$

Now, the Peclet numbers for both workpiece and cutting tool is calculated.

$$Pe_{\text{workpiece}} = Ua / 2\chi$$

$$\text{here,} \quad U_{\text{workpiece}} = 0.000776 \text{ m/s}$$

$$\therefore Pe_{\text{workpiece}} = 0.000776 * 0.000016648 / 2 * 1.356 \times 10^{-5}$$

$$\therefore \underline{Pe_{\text{workpiece}} = 0.000286 \text{ (negligible)}}$$

$$\therefore Pe_{\text{workpiece}} < 0.1 \text{ (One surface moves slowly with respect to other)}$$

Also,

$$Pe_{\text{tool}} = Ua/2\chi$$

$$\text{here, } U_{\text{tool}} = 0.4 \text{ m/s}$$

$$\therefore Pe_{\text{tool}} = 0.4 * 0.000016648 / 2 * 2.256 \times 10^{-5}$$

$$\therefore \underline{Pe_{\text{tool}} = 0.245}$$

$$\therefore 0.1 < Pe_{\text{tool}} < 5 \text{ (Intermediate region i.e. one surface moves fast with respect to other although on the side of a slow moving heat source)}$$

Now, the proportion of heat (η) in the workpiece and the tool is calculated.

$$\eta_{\text{workpiece}} = 1 / 1 + (\kappa_{\text{tool}} \times \sqrt{Pe_{\text{tool}}} / \kappa_{\text{workpiece}} \times \sqrt{Pe_{\text{workpiece}}})$$

Note: Pe is dropped from the equation because of its very low value.

$$\therefore \eta_{\text{workpiece}} = 1 / 1 + (112 / 51.9)$$

$$\therefore \eta_{\text{workpiece}} = 0.316$$

$$\therefore \underline{\eta_{\text{workpiece}} = 31.6\%}$$

$$\therefore \eta_{\text{tool}} = 1 - \eta_{\text{workpiece}} = 0.684 = 68.4\%$$

\therefore 31.6% of the heat generated goes in the workpiece and the remaining 68.4% of the heat goes in the cutting tool.

Finally, the average flash temperature for workpiece and cutting tool is calculated.

$$T_{\text{fa}_{\text{workpiece}}} = 0.159 C_3 \times \frac{\mu W (U_{\text{workpiece}} - U_{\text{tool}})}{Kl} \times \frac{\chi}{U_b} \dots \dots \text{(From Table 5)}$$

here, $C_3 = 1.1$ $\mu = 0.15$ $b = 0.0015875$ m

$$\therefore T_{fa_{workpiece}} = 0.159 \times 1.1 \times \frac{0.15 \times 5.6956(0.000776)}{51.9 \times 0.000016648} \times \frac{1.356 \times 10^{-5}}{0.000776 \times 0.0015875}$$

$$\therefore T_{fa_{workpiece}} = 1.477^\circ\text{C} + 25^\circ\text{C}$$

$$\therefore \underline{T_{fa_{workpiece}} = 26.52^\circ\text{C}}$$

Also,

$$T_{fa_{tool}} = 0.318 \times \frac{\mu W (U_{workpiece} - U_{tool})}{Kl} \times \frac{\chi}{ub} \times (-2.303 L \log_{10} 2 Pe + 1.616 Pe)$$

..... (From Table 5)

$$\therefore T_{fa_{tool}} = 0.318 \times \frac{0.15 \times 5.6956(0.4)}{51.9 \times 0.000016648} \times \frac{2.256 \times 10^{-5}}{0.4 \times 0.0015875} \times (-2.303 \times 0.000286 \times \log_{10} 2 \times 0.000286 + 1.616 \times 0.000286)$$

$$\therefore T_{fa_{tool}} = 0.0053^\circ\text{C} + 25^\circ\text{C}$$

$$\therefore \underline{T_{fa_{tool}} = 25.0053^\circ\text{C}}$$

Now, the maximum flash temperature for workpiece and cutting tool is calculated.

$$T_{fmax_{workpiece}} = 0.159 C_4 \times \frac{\mu W (U_a - U_b)}{Kl} \times \frac{\chi}{ub}$$

here, $C_4 = 1.3$

$$\therefore T_{fmax_{workpiece}} = 0.159 \times 1.3 \times \frac{0.15 \times 5.6956(0.000776)}{51.9 \times 0.000016648} \times \frac{1.356 \times 10^{-5}}{0.000776 \times 0.0015875}$$

$$\therefore T_{fmax_{workpiece}} = 1.8129^\circ\text{C} + 25^\circ\text{C}$$

$$\therefore \underline{T_{fmax_{workpiece}} = 26.8129^\circ\text{C}}$$

Also,

$$T_{fmax_{tool}} = 0.318 \times \frac{\mu W (U_{workpiece} - U_{tool})}{Kl} \times \frac{\chi}{U_b} \times (-2.303 L \log_{10} Pe + 1.616 Pe)$$

..... (From Table 5)

$$\therefore T_{fmax_{tool}} = 0.318 \times \frac{0.15 \times 5.6956(0.4)}{51.9 \times 0.000016648} \times \frac{2.256 \times 10^{-5}}{0.4 \times 0.0015875} \times (-2.303 \times 0.000286 \times \log_{10}^* 0.000286 + 1.616 \times 0.000286)$$

$$\therefore T_{fmax_{tool}} = 0.005789 \text{ } ^\circ\text{C} + 25 \text{ } ^\circ\text{C}$$

$$\therefore \underline{T_{fmax_{tool}} = 25.005789 \text{ } ^\circ\text{C}}$$

Similarly, all the remaining machining combinations were considered and the cutting tool/workpiece interface temperatures were calculated. The results are given in table 12 below:

Table 12: Temperature calculations for different cutting speeds and feed rates combinations.

Speed (SFM) Feed (IPT) Combination	Peclet # Work	Peclet # Tool	Tfa (Work) °C	Tfa (Tool) °C	Tfmax (Work) °C	Tfmax (Tool) °C
80 - 0.003	0.24	0.00	1.47	0.00	1.80	0.00
100 - 0.003	0.30	0.00	1.47	0.00	1.80	0.00
120 - 0.003	0.37	0.00	1.47	0.00	1.80	0.00
80 - 0.005	0.24	0.00	1.47	0.00	1.80	0.00
100 - 0.005	0.30	0.00	1.47	0.01	1.80	0.01
120 - 0.005	0.37	0.00	1.47	0.01	1.80	0.01

Note: Work = Workpiece

Based on the values in table 12, the interfacial flash temperatures are very low indicating that heat generated via heat conduction during end milling is minimal. Thus, phenomena like recrystallization of the steel during end milling are non-operative. These values are not surprising since the loads and speed are relatively low during end milling. Furthermore, the lubricant will further dissipate heat in the tool-workpiece contact.

Tool Life

Figures 47 and 48, shows the tool life in minutes and material removal volume (MRV) in mm^3 for different cutting speed and feed rate combinations, respectively. Cutting with lower feed rate resulted in prolonged tool life and highest MRV whereas cutting with higher feed rates decreased the tool life and MRV significantly. Lower cutting speed produces lower revolution per minutes (RPM) of the spindle. Lower spindle RPM combined with lower feed rates produces more chips and higher MRV and vice-versa.

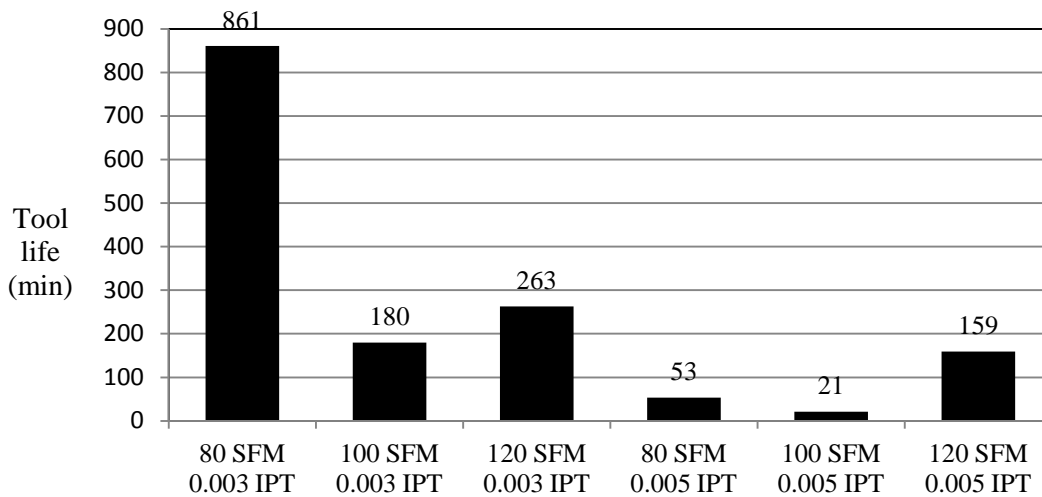


Figure 47: Tool life for different cutting speeds and feed rates combinations at failure.

The highest tool life was realized using treatment 80 SFM and 0.003 IPT. The tool failed after 861 minutes of machining at this treatment. Due to the lower cutting speed and feed rate (Childs et al. 2000), it is hypothesized that the aerosol particle produced by microlubrication easily penetrated through to the tool/workpiece interface (Min et al. 2005) and lubrication occurs by diffusion through the workpiece, and the cutting fluid reacts to form a boundary layer of solid-film lubricant (Adler et al. 2006). This led to the cooling of the cutting tool and simultaneously the lubrication of the tool/workpiece interface. At low cutting speed, the cutting temperature is also expected to be low as compared to the other cutting speed and feed rate

combinations (ASM International, 1989; Shaw et al. 1951). This also contributes to the increase in tool life.

But it was also observed that the MRV for cutting speed of 120 SFM was identical for both the feed rates of 0.003 and 0.005 IPT, used in the study. This is because feed rate is more significant parameter than the cutting speed in controlling the MRV (Yanda et al. 2010). Also, high spindle speed in combination with high feed rate can cause evaporative cooling and enhances the cutting tool performance resulting in higher MRV (Jayal & Balaji, 2009). One other fact to consider is that both the cutting combinations machined exactly the same number of workpieces. But, the feed rate of 0.003 IPT being slower gave a higher tool life in minutes than at 0.005 IPT.

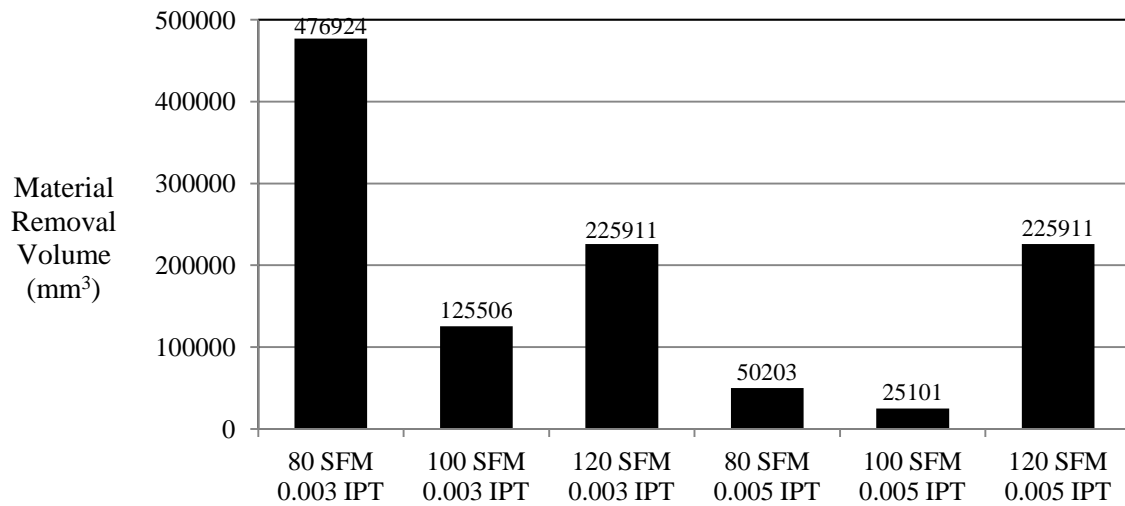


Figure 48: Material removal volume for different cutting speeds and feed rates combinations at failure.

The lowest tool life was realized using treatment 100 SFM and 0.005 IPT. The tool failed only after 21 minutes of machining. Several reasons are hypothesized to have contributed to the lower tool life. Due to high feed rate, the cutting fluid cannot effectively cool and lubricate the cutting zone leading to higher temperatures. The tip of the tool is highly sensitive at high

temperature (Dhar et al. 2006). Also under high feed rate, the subsurface of the workpiece is harder due in part to work hardening resulting in earlier tool failure (Jayal et al. 2010).

Wear Mechanisms

All the cutting tools under consideration failed with gradual abrasive wear except for treatment 80 SFM and 0.005 IPT, which underwent a catastrophic failure.

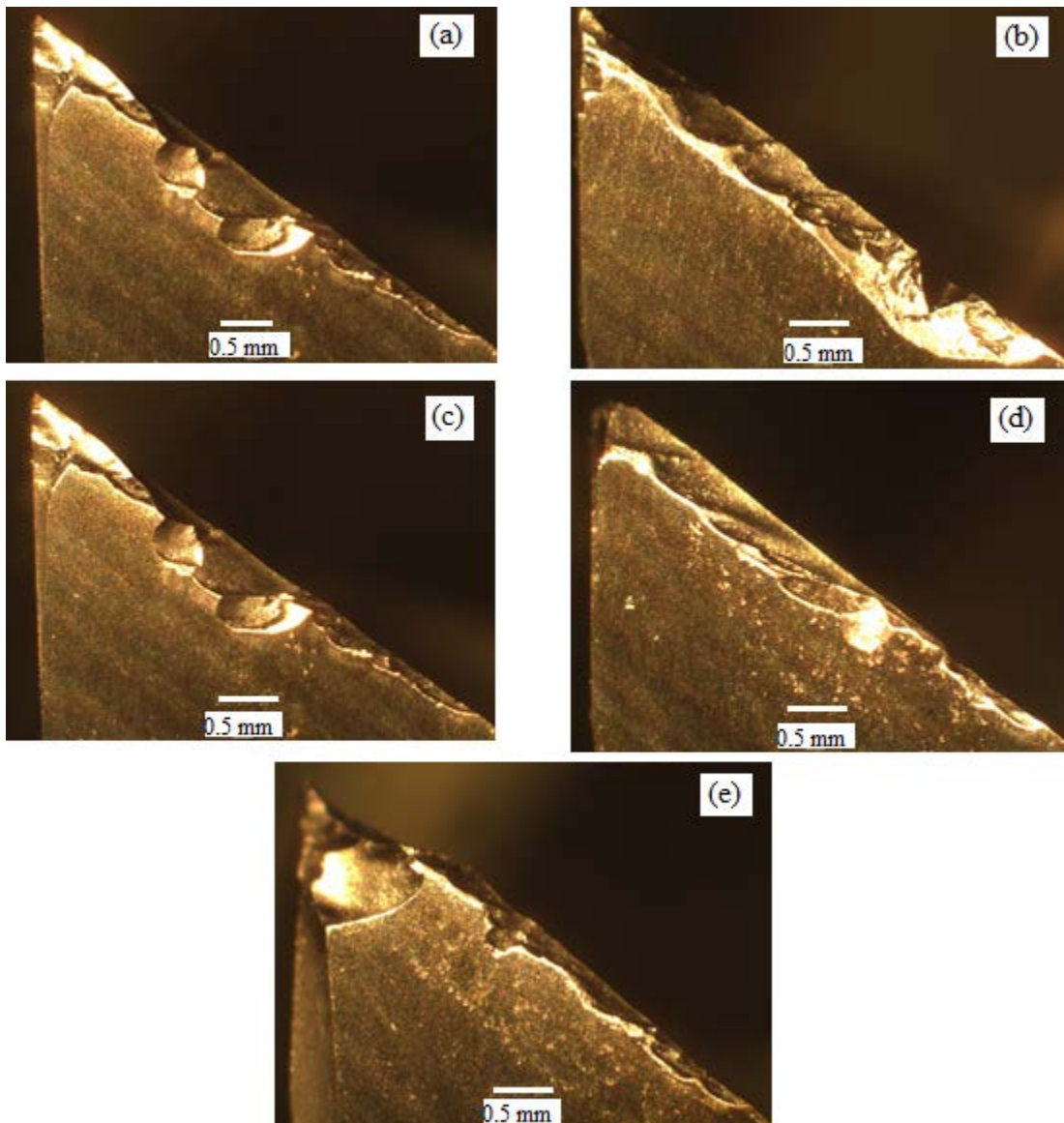


Figure 49: Optical micrograph of tool flank wear for treatment (a) 80 SFM and 0.003 IPT (b) 120 SFM and 0.003 IPT (c) 100 SFM and 0.005 IPT (d) 120 SFM and 0.005 IPT (e) 100 SFM and 0.003 IPT.

Figures 49(a) – 49(e), show the cutting tool at failure for all the treatments. Based on scanning electron microscopy (SEM) observations, two-body abrasion wear mode is likely dominant. In addition, chips form a foreign body and slide between the tool flank wear and the workpiece activating sliding wear as shown in figure 52, causing the tool tip to gradually wear out at the contact zone. In low carbon steel, the softer ferrite phase coexists with patches of pearlite. These pearlite patches as a whole work as an abrasive and “break off” abrading the tool surface (Kwon, 2000). Figure 50, shows that for treatment 100 SFM and 0.003 IPT, the tool had gone through chipping before it underwent failure.

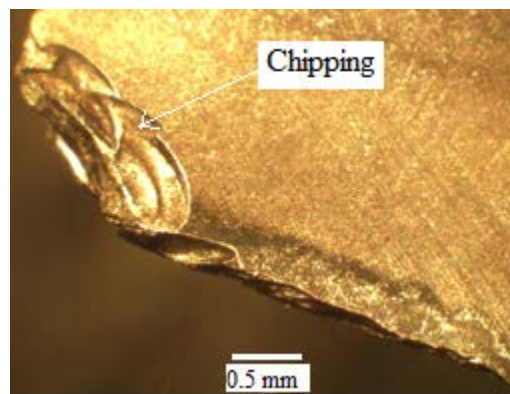


Figure 50: Optical micrograph of tool rake for treatment 100 SFM and 0.003 IPT.

Figure 51, shows the cutting tool for treatment 80 SFM and 0.005 IPT, which exhibited catastrophic failure. The massive chipping shown in the figure 51 is the reason for the failure of the tool. Two main conditions or causes of chipping are mechanical shock (i.e. impact by interrupted cutting as in milling), and thermal fatigue (i.e. cyclic variation in temperature of the tool in interrupted cutting) (Kalpakjian, 1995). Chipping can also be caused by high temperatures at higher speed or higher feed rate conditions. Failure is linked to the fatigue crack promoted by cyclic variation of the tool temperature during machining. Cutting tool embrittlement takes place causing fracture under high thermo-mechanical stresses (Da Silva et al. 2011).

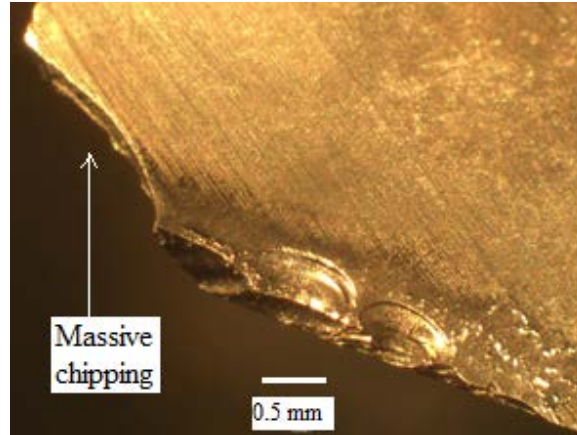


Figure 51: Optical micrograph of tool rake for treatment 80 SFM and 0.005 IPT.

SEM examinations of the cutting tool suggested that the bright oxide finish of the cutting tool has been removed at the cutting edge. SEM examination also enabled the cutting edge of the flank and the rake side of the cutting tool to be analyzed and revealed that various other micro wear mechanisms were activated at different cutting speed and feed rate levels. The cutting speed and feed rate level of 120 SFM and 0.005 IPT as well as 80 SFM and 0.003 IPT were selected for further SEM analysis. Figures 52, 53, 54, and 55, show SEM images of cutting tool edges for the cutting speed and feed rate level of 120 SFM and 0.005 IPT.

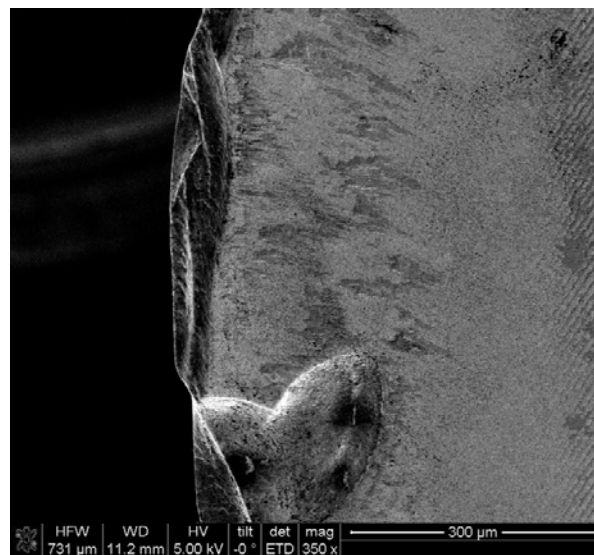


Figure 52: SEM micrograph of tool rake for treatment 120 SFM and 0.005 IPT showing sliding wear.

Figure 52 shows the occurrence of sliding wear having grooves parallel to the metal flow direction. Figures 53 (a) and (b) show non-uniform micro-abrasion for rake and the flank side, respectively. Micro grooves are formed which remove the tool coating and expose the tool substrate. This is partly due to the high temperature resulting from the high cutting speed and feed rate levels of 120 SFM and 0.005 IPT. Other reason can be high stresses exerted on the tool during the cutting process.

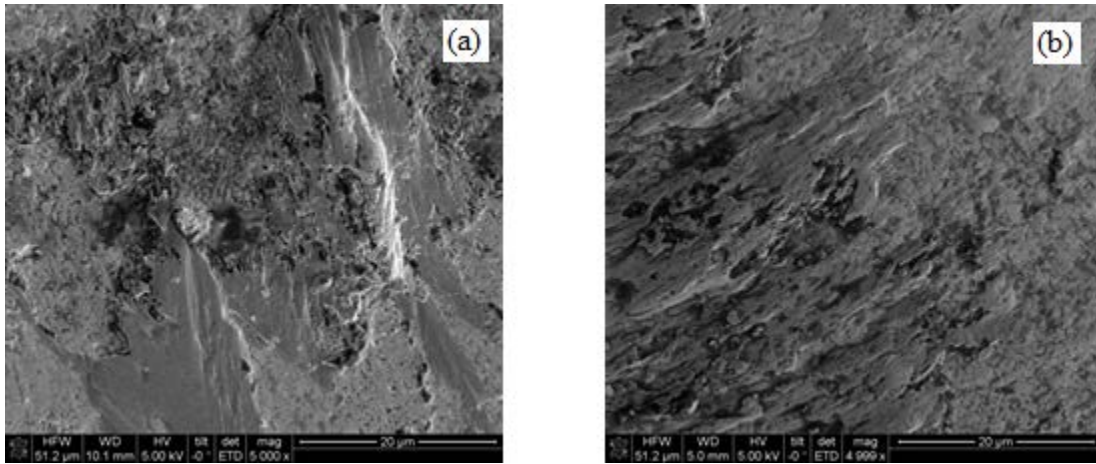


Figure 53: SEM micrograph of tool for treatment 120 SFM and 0.005 IPT showing non-uniform micro-abrasion (a) Rake (b) Flank.

Figure 54 shows development of micro-fatigue crack near to the cutting edge resulting in the weakening of the bright oxide finish coating and decreasing the local hardness. Finally, resulting in the removal of the coating from the tool and exposing the tool substrate. Figures 55 (a) and (b), shows micro-chips being welded on rake and flank face, respectively. A higher magnification inset picture is also shown to clarify the view. It is hypothesized that chips at higher speed and feed rate level get welded to the cutting tool because of inadequate time for the metal working fluid (MWF) to reach the cutting tool-workpiece interface.

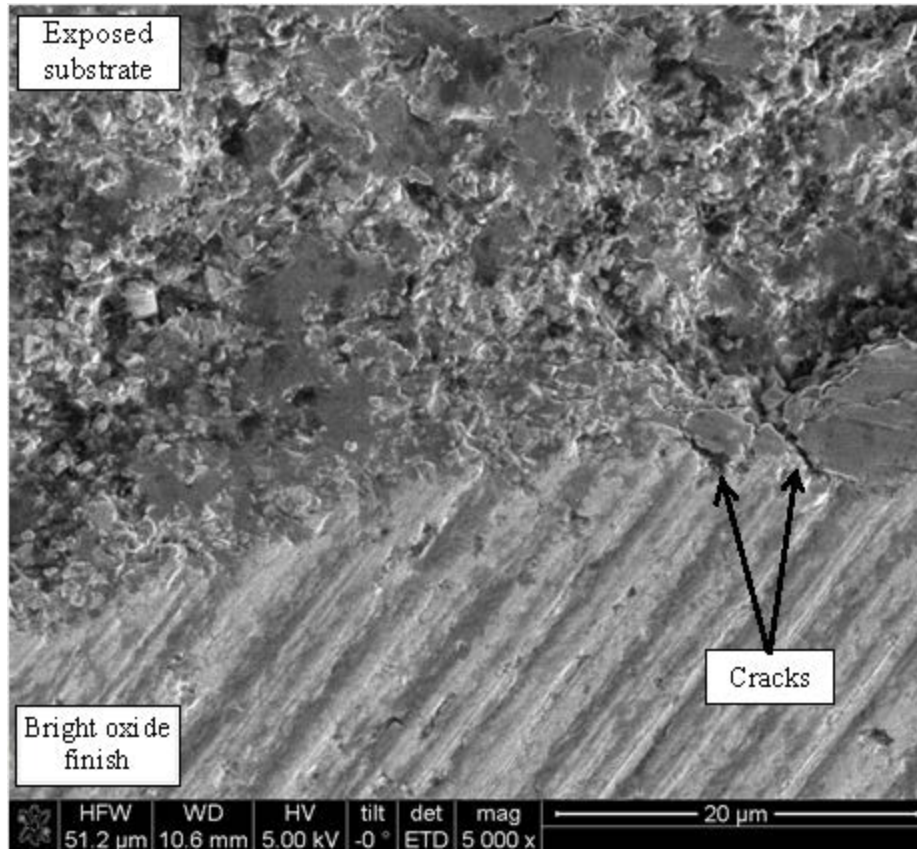


Figure 54: SEM micrograph of tool rake for treatment 80 SFM and 0.003 IPT showing micro-fatigue crack.

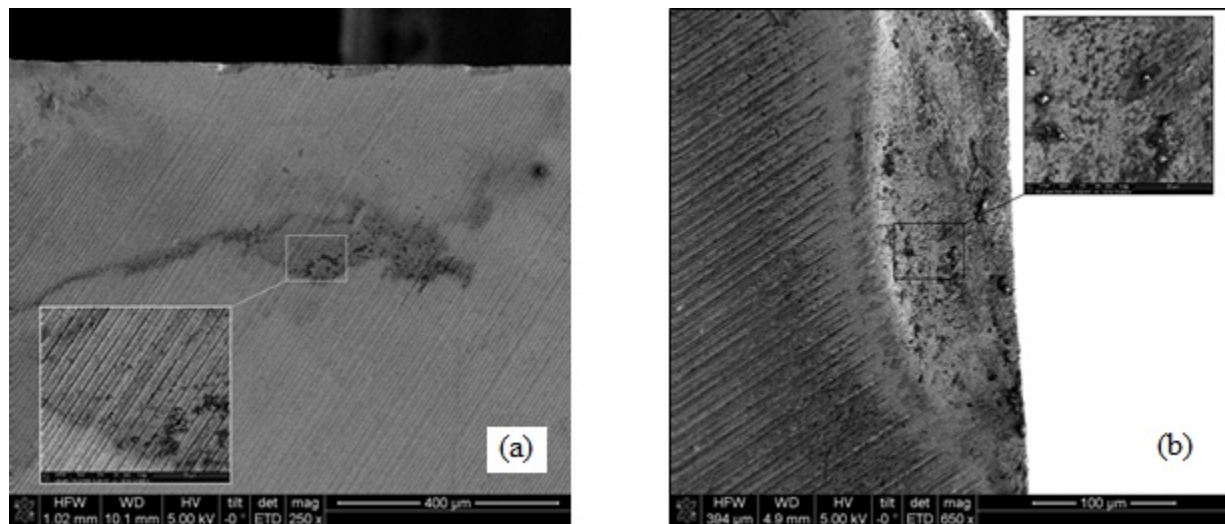


Figure 55: SEM micrograph of tool for treatment 120 SFM and 0.005 IPT showing welded micro-chips (a) Rake (b) Flank.

Figures 56, 57, 58 and 59, show SEM images of cutting tool edges for the cutting speed and feed rate level of 80 SFM and 0.003 IPT. Sliding wear and non-uniform micro-abrasion similar to high speed and feed rate level was observed for low speed and low feed rate levels (i.e. 80 SFM and 0.003 IPT).

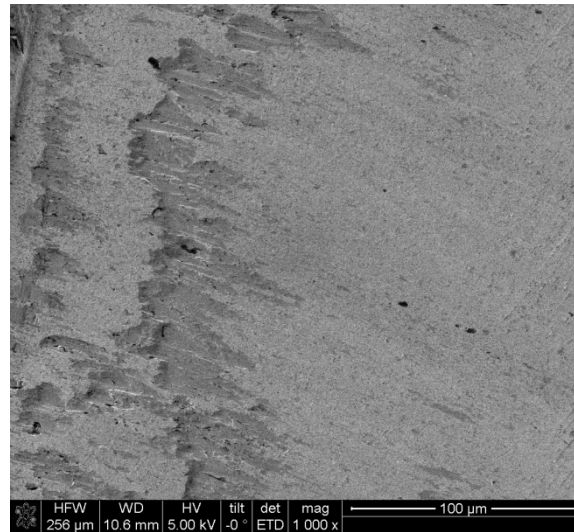


Figure 56: SEM micrograph of tool rake for treatment 80 SFM and 0.003 IPT showing sliding wear.

Figure 56 shows the occurrence of sliding wear having grooves parallel to the metal flow direction. Figure 57 (a) and (b) show non-uniform micro-abrasion for rake and the flank side, respectively. Micro-fatigue cracks were not observed at this treatment. The tool flank and rake faces showed unusual build-up edge (BUE) and adhesion of workpiece material to the cutting edges for treatment 80 SFM and 0.003 IPT, as shown in figures 58 and 59, respectively. The BUE shown in figure 59 was not a stable kind of BUE.

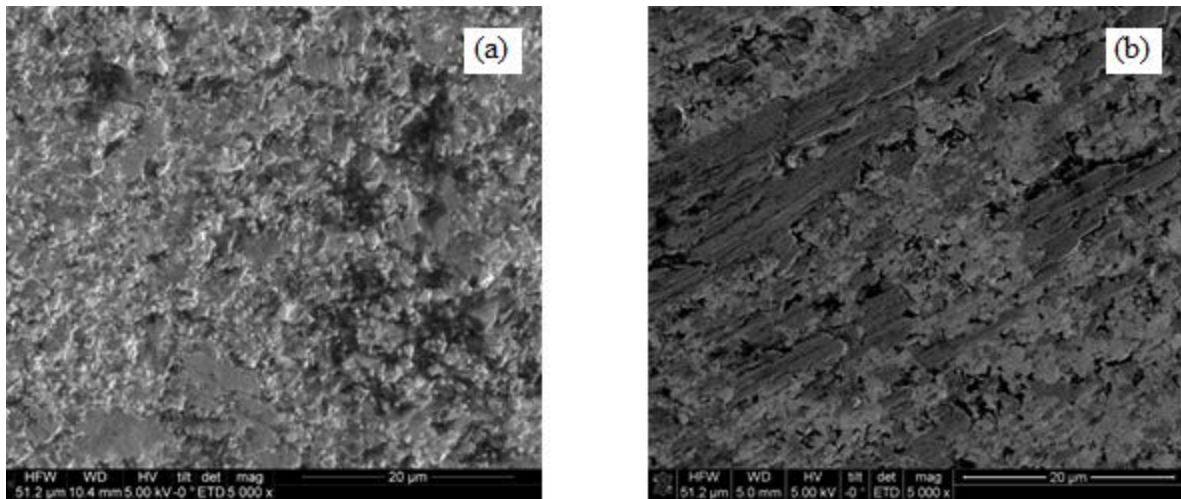


Figure 57: SEM micrograph of tool for treatment 80 SFM and 0.003 IPT showing non-uniform micro-abrasion (a) Rake (b) Flank.



Figure 58: SEM micrograph of tool flank for treatment 80 SFM and 0.003 IPT showing adhesion.

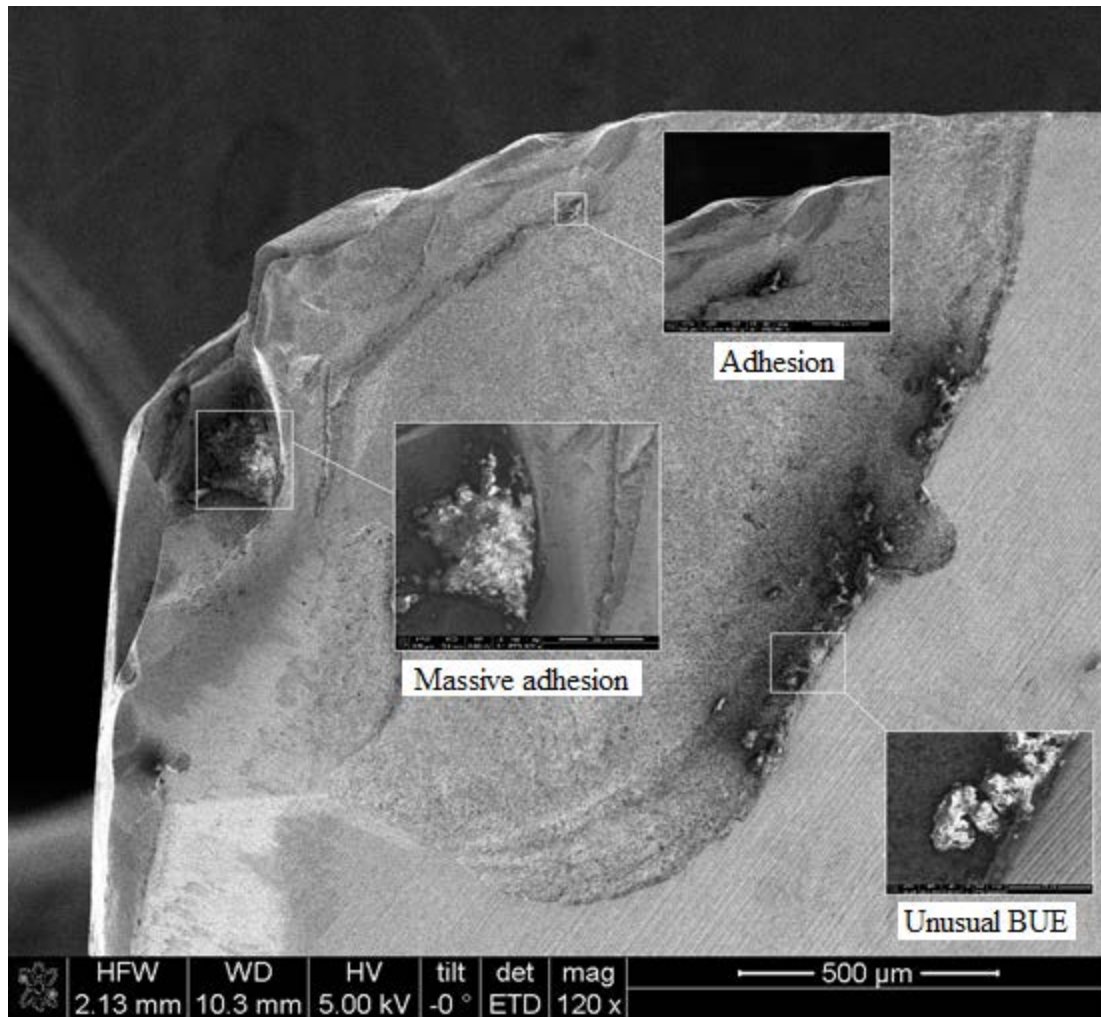


Figure 59: SEM micrograph of tool rake for treatment 80 SFM and 0.003 IPT showing adhesion and built-up edge (BUE).

Figure 60 shows the SEM image of the workpiece surface for treatment 80 SFM and 0.003 IPT. The images clearly show abrasive wear through the mechanism of plowing. It is hypothesized that these small fragments of workpiece materials have adhered to the cutting tool faces causing adhesive wear. However, it is to be noted that plowing did not happen consistently throughout the machined workpiece surface.

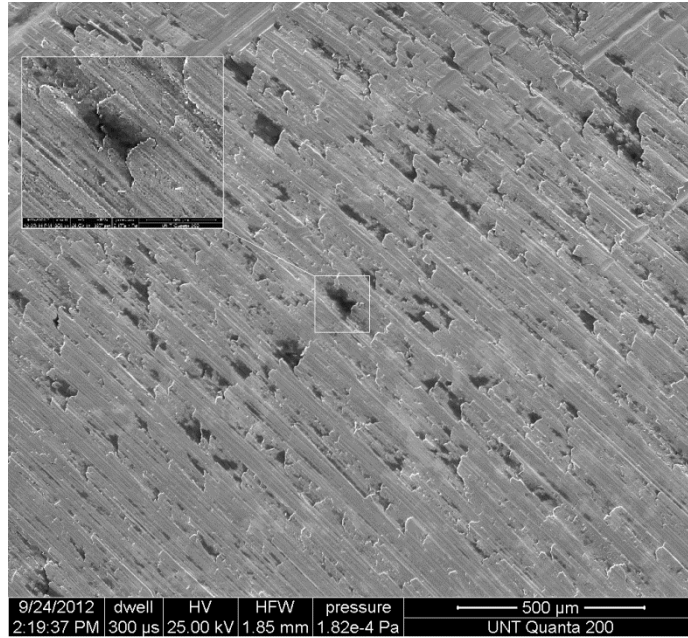


Figure 60: SEM micrograph of workpiece for treatment 80 SFM and 0.003 IPT showing abrasive wear through plowing mechanism.

Cross Sectional Hardness Analysis at Failure

Measurement of cross-sectional vickers microhardness was carried out for the cutting speed and feed rate level of 120 SFM and 0.005 IPT as well as for 80 SFM and 0.003 IPT. Figures 61 and 62, shows the graphical representation of microhardness as a function of depth below the machined surface for 120 SFM and 0.005 IPT and for 80 SFM and 0.003 IPT, respectively. The plastic deformation due to machining extends to about 150 – 180 μm for both the treatments. Figures 61 and 62 indicate that a few microns away from the cutting surface the hardness increases beyond the bulk hardness of the material. Moving further away from the machined surface, the hardness starts to decrease and reaches the bulk hardness. The strengthening mechanism can be attributed to the increase in dislocation density due to plastic deformation. The dislocation density analysis is done in the subsequent sections of this study.

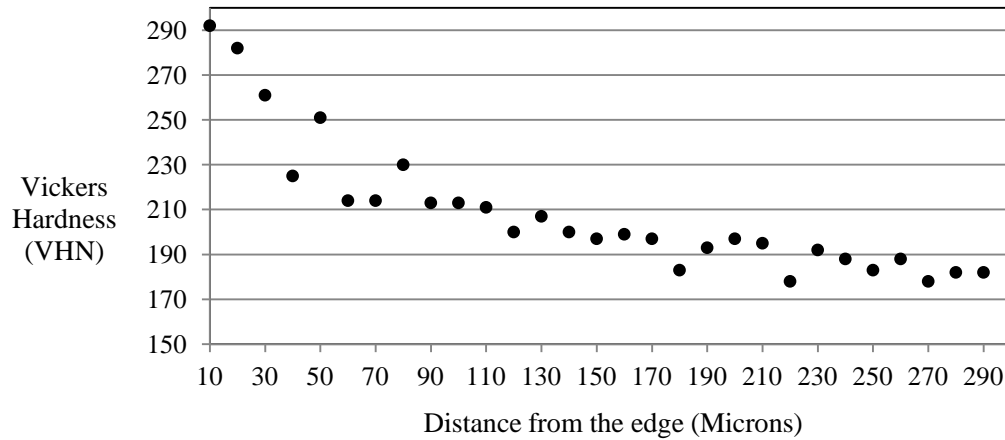


Figure 61: Microhardness depth profile of cross-section for treatment 120 SFM and 0.005 IPT.

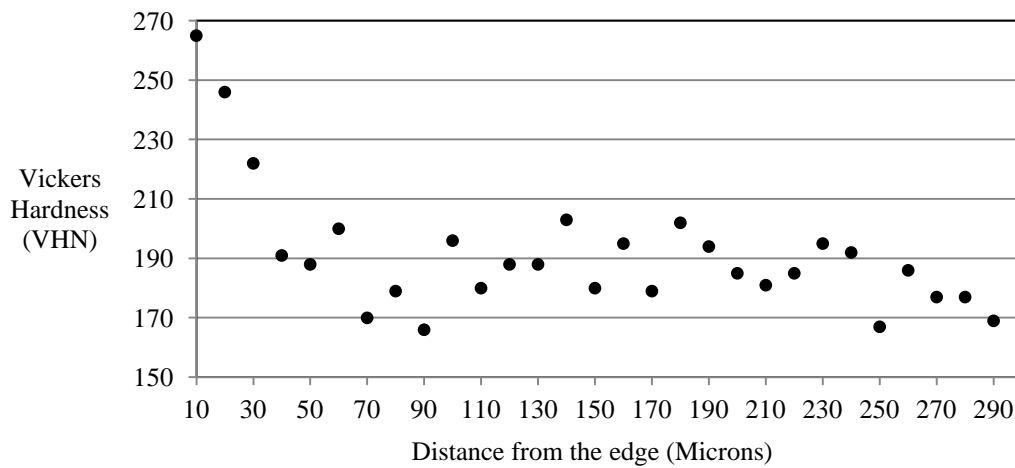


Figure 62: Microhardness depth profile of cross-section for treatment 80 SFM and 0.003 IPT.

Bearing Area Curve Calculations

Figure 63 and 64; show the surface profile of the workpiece at failure for the cutting speed and feed rate level of 120 SFM and 0.005 IPT as well as for the cutting speed and feed rate level of 80 SFM and 0.003 IPT.

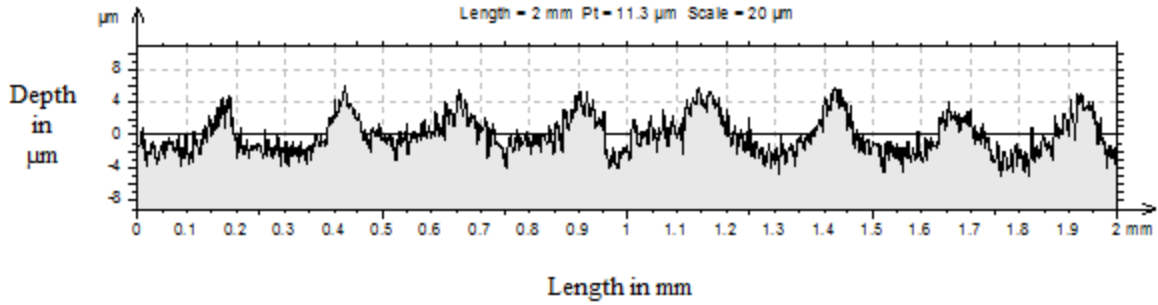


Figure 63: Surface profile at failure for treatment 120 SFM and 0.005 IPT.

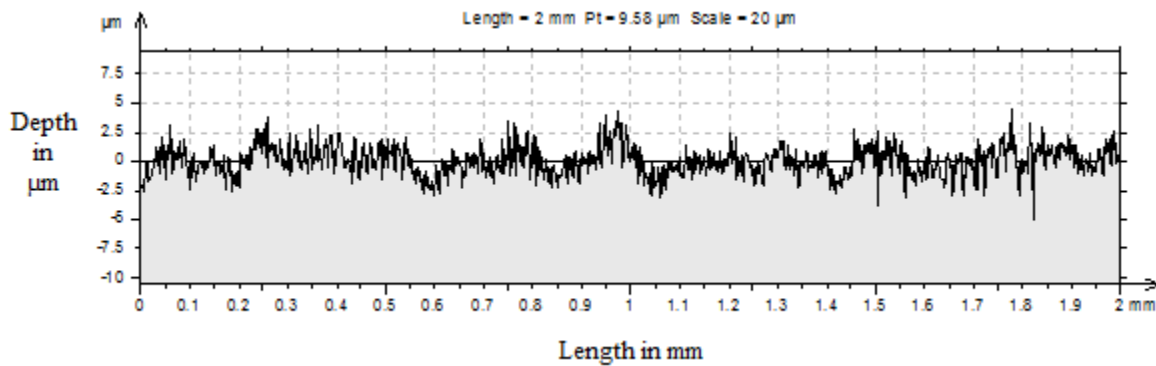


Figure 64: Surface profile at failure for treatment 80 SFM and 0.003 IPT.

Figures 65 and 66, show the depth histograms of the workpiece at failure for the cutting speed and feed rate level of 120 SFM and 0.005 IPT as well as for the cutting speed and feed rate level of 80 SFM and 0.003 IPT, respectively. The depths histogram helps us to study the density of the distribution of the data points in the profile. The vertical axis is graduated in depths; the horizontal axis is graduated in % of the whole population. Here for treatment 120 SFM and 0.005 IPT, 12% of the depth population is in between 7.35 μm and 7.92 μm as shown by the black circle in figure 65.

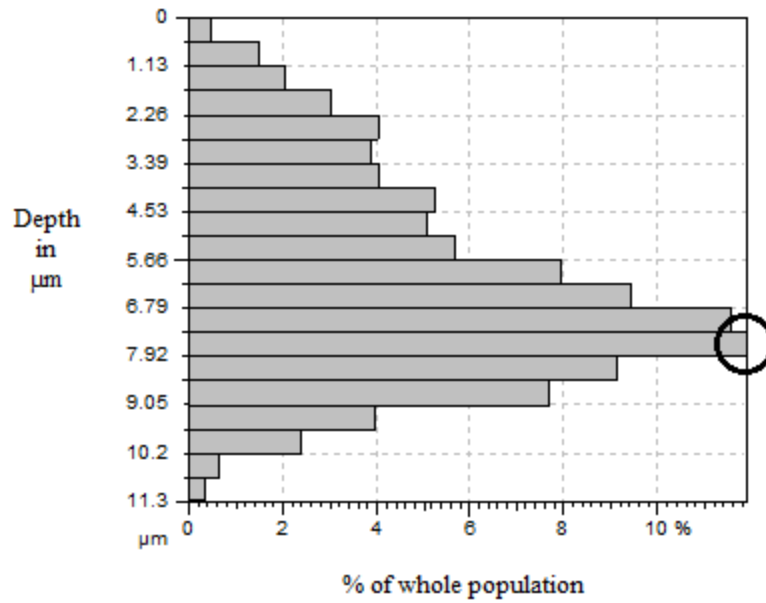


Figure 65: Histogram for treatment 120 SFM and 0.005 IPT.

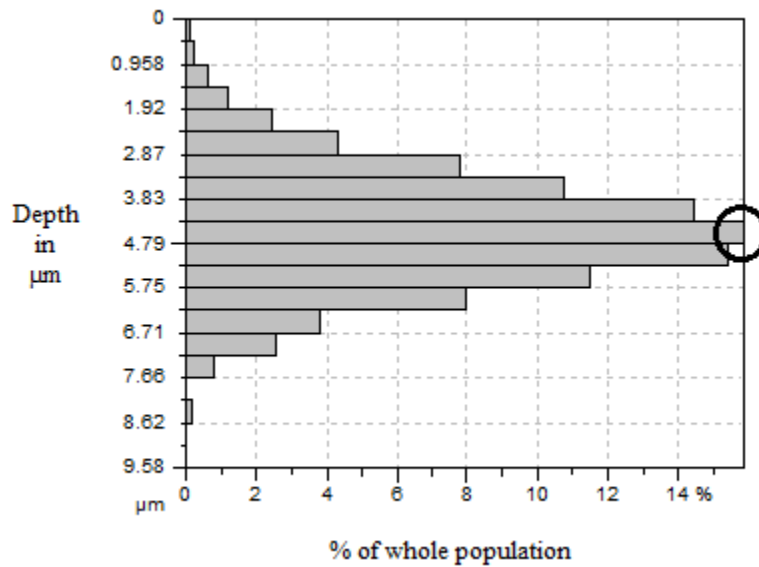


Figure 66: Histogram for treatment 80 SFM and 0.003 IPT.

For treatment 80 SFM and 0.003 IPT, 16% of the depth population is in between 4.31 μm and 4.79 μm as shown by the black circle in figure 66. Figures 67 and 68, shows the bearing area curve (BAC) of the workpiece at failure for the cutting speed and feed rate level of 120 SFM and 0.005 IPT as well as for the cutting speed and feed rate level of 120 SFM and 0.005 IPT. The

BAC presents the bearing ratio curve. For a given depth, the bearing ratio is the percentage of material traversed in relation to the area covered. This function is the cumulating function of the depth distribution function. The horizontal axis represents the bearing ratio (in %) and the vertical axis the depths in microns.

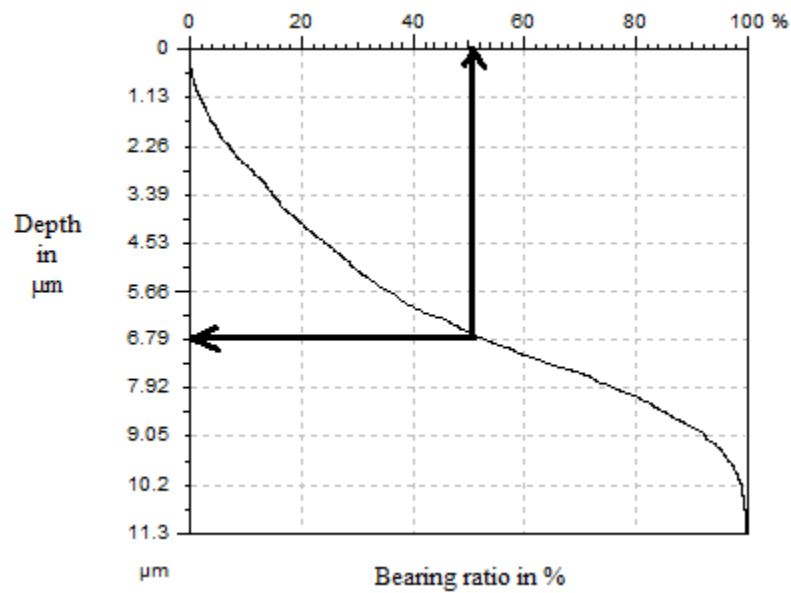


Figure 67: Bearing area curve at failure for treatment 120 SFM and 0.005 IPT.

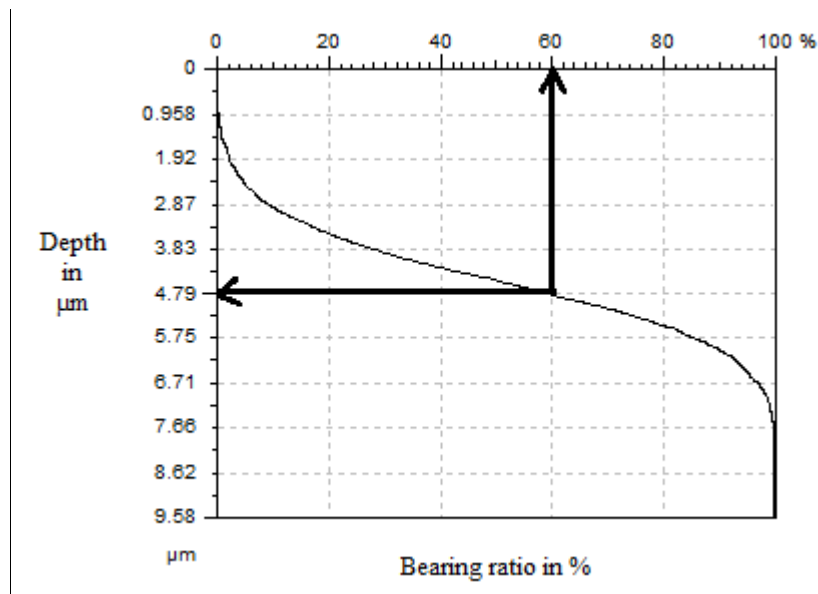


Figure 68: Bearing area curve at failure for treatment 80 SFM and 0.003 IPT.

Here, for treatment 120 SFM and 0.005 IPT, almost 50% of the points have a depth that lies between 0 and 6.79 μm as shown by the two arrows in figure 67. Similarly, for treatment 80 SFM and 0.003 IPT, almost 60% of the points have a depth that lies between 0 and 4.79 μm as shown by the two arrows in figure 68.

Table 13: Roughness parameter for different cutting speeds and feed rates combinations.

Speed (SFM) – Feed (IPT) Combination	R_a (μm)	R_q (μm)	R_{sk}	R_{ku}
80 – 0.003	0.915	1.18	0.374	3.3
120 – 0.005	1.77	2.2	0.741	2.59

Note: R_a - Arithmetic Mean Deviation, R_q - Root-mean-square deviation
 R_{sk} - Skewness of the roughness profile R_{ku} - Kurtosis of the roughness profile

Table 13, shows the R_a , R_q , R_{sk} and R_{ku} values. The R_a value for treatment 120 SFM and 0.005 IPT and treatment 80 SFM and 0.003 IPT was 1.77 and 0.915 μm , respectively. The R_q value for treatment 120 SFM and 0.005 IPT and treatment 80 SFM and 0.003 IPT was 2.2 and 1.18 μm , respectively. The R_{sk} value for treatment 120 SFM and 0.005 IPT and treatment 80 SFM and 0.003 IPT was 0.741 and 0.374, respectively. Both the treatments have positive skewness (R_{sk}) which means that the bulk of values lie on the left side of the mean. The R_{ku} value for treatment 120 SFM and 0.005 IPT and treatment 80 SFM and 0.003 IPT was 2.59 and 3.3, respectively. Kurtosis is the degree of peakedness of a distribution. A negative kurtosis means a ‘flat’ distribution. But, both the treatments have positive kurtosis (R_{ku}) which indicates a ‘peaked’ distribution

TEM Analysis at Failure

Cross sectional TEM analysis at failure was carried out for the cutting speed and feed rate level of 120 SFM and 0.005 IPT. Three samples for the TEM analysis were prepared based on

the vickers microhardness measurements. Two samples were prepared at a depth of 20 μm and 100 μm from the machined edge and one sample was prepared from the bulk of the sample. The objective was to investigate the workpiece subsurface deformation and strengthening. Focused Ion Beam (FIB) was used to produce lift-outs samples for the TEM analysis as shown in figure 69.

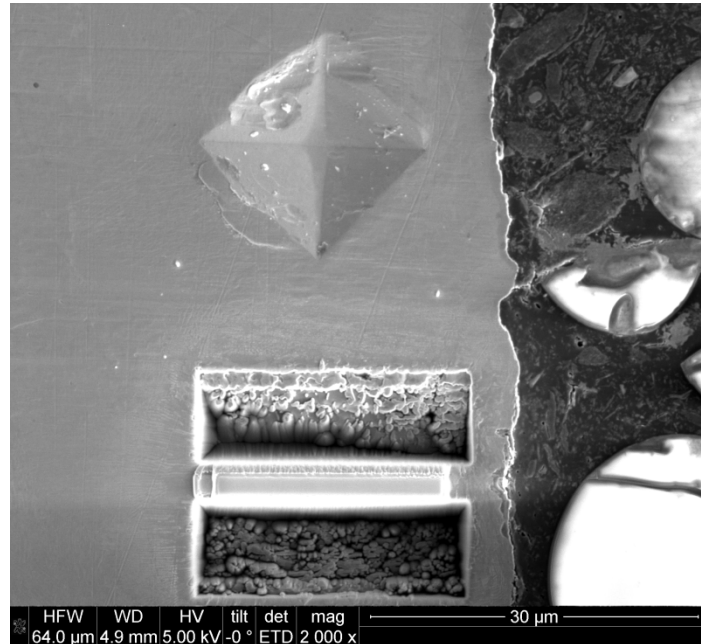


Figure 69: Lift-out area 20 μm from machined edge for treatment 120 SFM and 0.005 IPT.

Figure 70 shows the TEM image at a depth of 20 μm from the machined edge. The figure shows a high concentration of dislocation density.

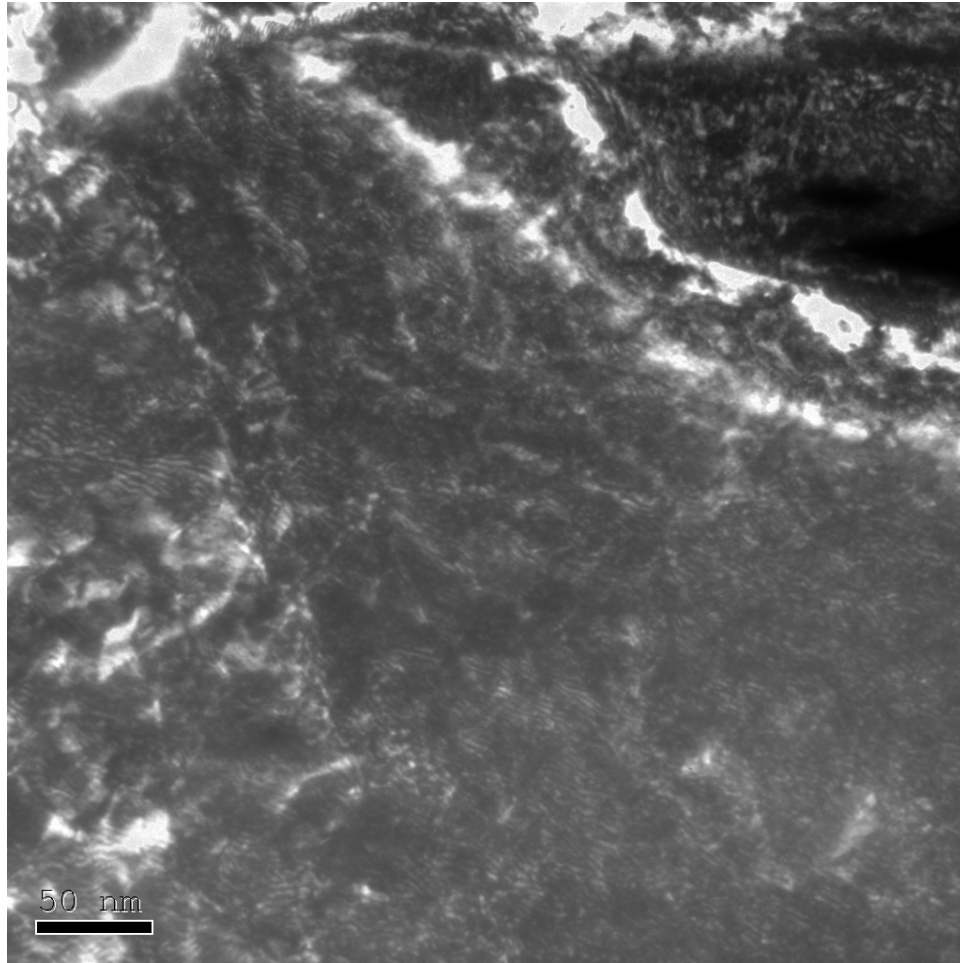


Figure 70: TEM image showing dislocations for a depth of 20 μm from machined edge for treatment 120 SFM and 0.005 IPT.

Figure 71 (a) and (b) show the TEM images having dislocation pile-ups at the grain boundaries (GB). It is hypothesized that the high concentration of dislocation density combined with the dislocation pile-ups near the grain boundary are the reason for high hardness near the cross section of the machined edge at a depth of 20 μm as shown in figure 61. Figure 72 show the TEM images at a depth of 100 μm from the machined edge. The figure shows a fewer concentration of dislocation density. The results are again in accordance with figure 61, which shows decreased hardness as we go away from the machined surface due to fewer dislocations.

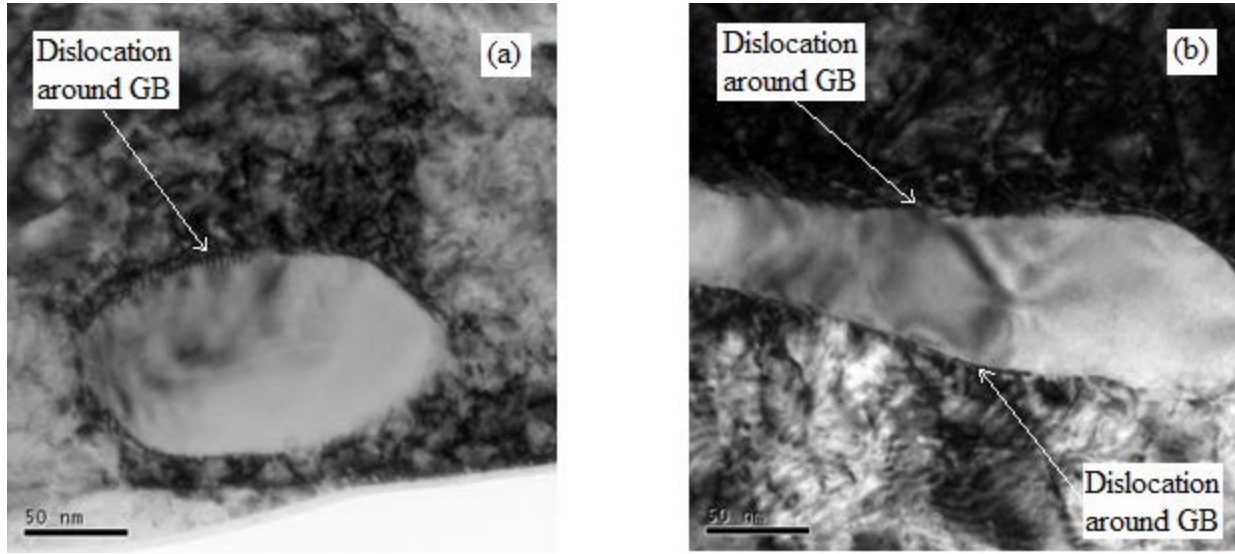


Figure 71 (a) and (b): TEM image showing dislocation pile-ups for a depth of 20 μm from machined edge for treatment 120 SFM and 0.005 IPT.

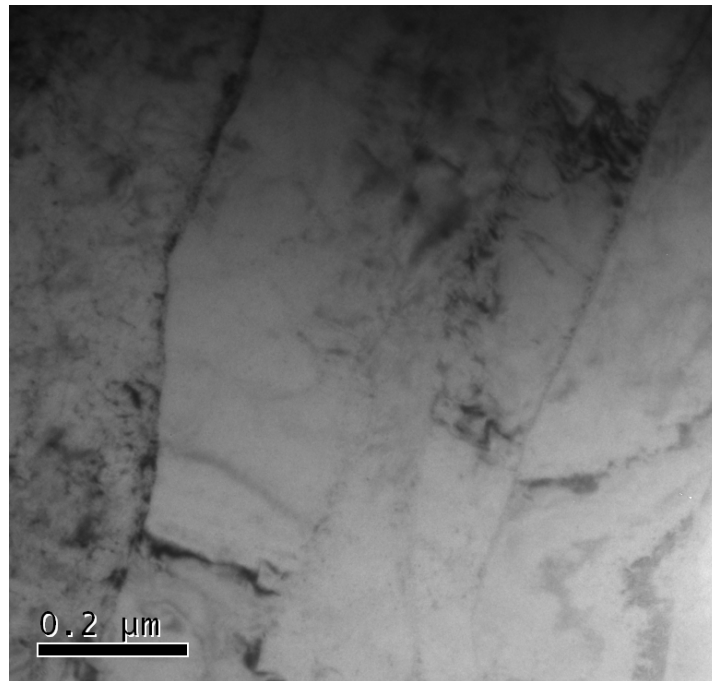


Figure 72: TEM image showing fewer dislocations for a depth of 100 μm from machined edge for treatment 120 SFM and 0.005 IPT.

Furthermore, dislocation density quantification was done to quantify the amount of dislocations present at a depth of 20 μm from the machined edge for treatment 120 SFM and

0.005 IPR. Table 14 shows the s_i , n_i and s_i^2/n_i^2 values. Figure 73 shows the graphical method used to calculate the foil thickness (t) of the sample. The intercept of the line with the ordinate is $1/t^2$. Here, $1/t^2 = 0.82 \times 10^{-4} \text{ nm}^{-2}$. Therefore, thickness of the foil (t) is 111 nm.

Table 14: CBED data for thickness determination.

$S_i \text{ (nm}^{-1}\text{)}$	n_i	$S_i^2/n_k^2 \text{ (nm}^{-2}\text{)}$
0.599×10^{-2}	1	0.35×10^{-4}
1.7×10^{-2}	2	0.72×10^{-4}

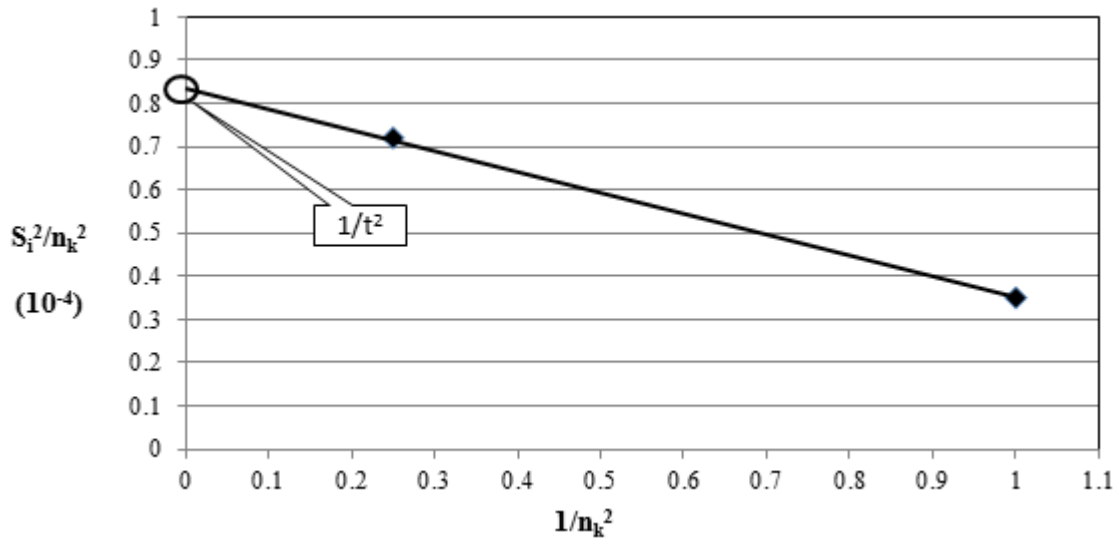


Figure 73: Intercept plot to extrapolate foil thickness value.

After calculating the foil thickness, the dislocation density (ρ) was calculated by using

Eq. 3.

$$\rho = \frac{1}{t} \left(\frac{\sum n_v}{\sum L_v} + \frac{\sum n_h}{\sum L_h} \right) \quad (3)$$

where,

$\sum n_v$ = number of intersections of vertical test lines with the dislocations

$\sum n_h$ = number of intersections of horizontal test lines with the dislocations

$\sum L_v$ = total length of vertical test lines

$$\sum L_h = \text{total length of horizontal test lines}$$

Five random sampling areas were selected on the two different images to calculate the dislocation densities as shown in figures 74 (a) and (b). Both the images show a magnified inset image with the approximate position where the grid was superimposed. Figure 75 shows the individual and average dislocation densities for image 1 and 2. The literature does not report any studies done to investigate the dislocation density by end milled American Iron and Steel Institute (AISI) 1018 steel. The closest study reported was by Yeagashi Koh. Yeagashi, 2007 investigated before and after deformation dislocation density on manganese steels having 0.18% carbon. The dislocation density (ρ) for the as-received material and material deformed in tension at 0.2% /min was reported to be $6.1 \times 10^{13} / \text{m}^2$ and $2.0 \times 10^{14} / \text{m}^2$, respectively.

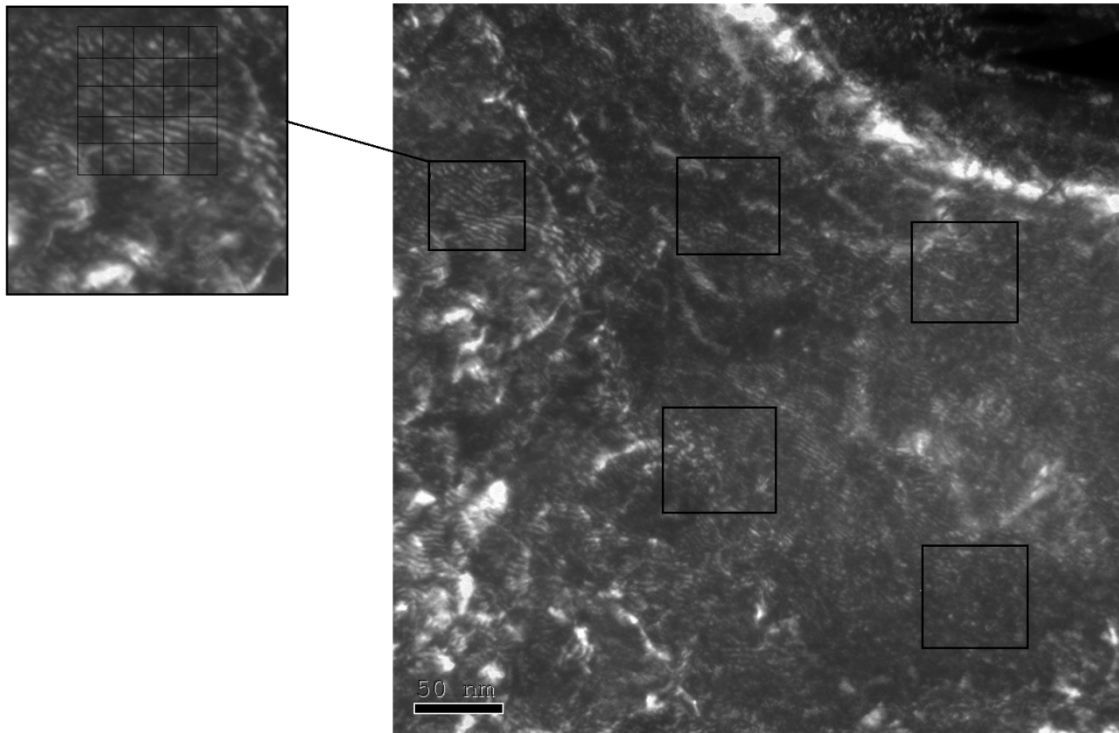


Figure 74 (a): TEM micrograph of image 1 used to determine ρ by the line intersection method at a depth of $20 \mu\text{m}$ from machined edge for treatment 120 SFM and 0.005 IPT.

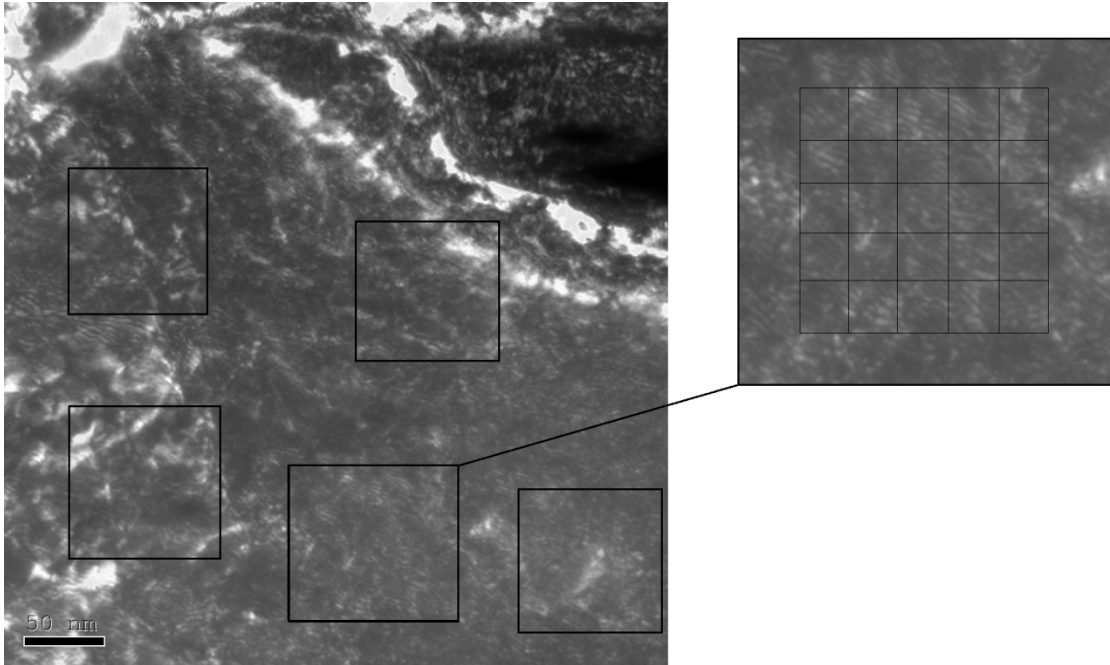


Figure 74 (b): TEM micrograph of image 2 used to determine ρ by the line intersection method at a depth of 20 μm from machined edge for treatment 120 SFM and 0.005 IPT.

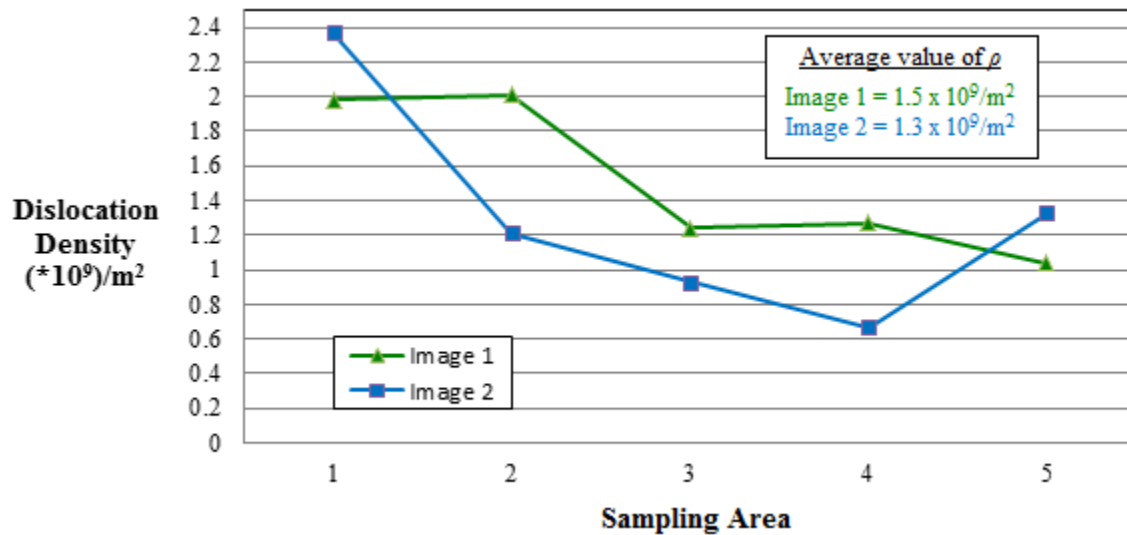


Figure 75: Dislocation density quantification at a depth of 20 μm from machined edge for treatment 120 SFM and 0.005 IPT.

Another closest study reported was by Yin et al. 2003. They investigated the dislocation density for austenitized warm-rolled 1015 phosphorus steel; water quenched to avoid the

formation of pearlite microstructure in low carbon steel and reported a dislocation density (ρ) of $1.06 \times 10^{14} / \text{m}^2$.

Some dislocation densities for low carbon steel as-received material reported in the literature are $1.0 \times 10^6 / \text{m}^2$ for transformer steel having 0.005% carbon (Vorobev and Krivisha, 1971); $1.0 \times 10^6 / \text{m}^2$ for 0.9% carbon steel (Ryufuku, 2007) and $1.0 \times 10^{12} / \text{m}^2$ for Cr-Mn steel having 0.06% carbon (Sternberk et al. 1985)

Other dislocation densities reported in the literature for low carbon steel after deformation are $1.5 \times 10^{14} / \text{m}^2$ for 0.05% carbon steel (Khodabakhshi and Kazeminezhad, 2011); $2.4 \times 10^{13} / \text{m}^2$ for AISI 1035 steel (Mohandesi et al., 2007) and $1.0 \times 10^{14} / \text{m}^2$ for AISI 4340 steel (Lee and Lam, 1996).

Increase in the dislocation density from the bulk of the material to the machined surface can also be associated with the increase in strength of the material at the surface. This increase in strength is already reported in this study. Taylor predicted that the strength of the metal crystal (τ) obeys the following equation (Taylor, 1934)

$$\tau = \mu \times b \times \alpha \sqrt{\rho} \quad (4)$$

where,

μ = shear modulus = 80 GPa (for 1018 steel)

b = Burgers vector = 0.259 nm (for 1018 steel)

α = geometric constant = 0.5

ρ = dislocation density

If it is assumed that the average dislocation density (ρ) of the bulk of the material is $1.0 \times 10^6 / \text{m}^2$. Then the shear strength of the bulk crystal (τ_{bulk}) will be 10,360 Pa or 1.50 Psi. Similarly, if we calculate the shear strength of the machined crystal, considering the average

dislocation density $1.5 \times 10^9 / \text{m}^2$ from Image 1. Then the shear strength of the machined crystal (τ_{machined}) will be 401,241 Pa or 58.19 Psi. This shows that the increase in the strength of the machined surface will be 38 times more than the bulk of the material. These results are in agreement with the vickers hardness test conducted in this study.

EBSD Analysis

EBSD analysis was carried out on two-samples each, for the as-received sample and samples at failure for the cutting speed and feed rate levels of (80 SFM – 0.003 IPT) and (120 SFM - 0.005 IPT), respectively. Figures 76 and 77 show the inverse pole figures (IPF) [001] of all the phases, ferrite and iron carbide phases for the as-received material, respectively. Figures 78, 79, and 80 show the IPF of all the phases, ferrite phase and the iron carbide phase for sample 1 and 2 at failure when machining at the cutting speed and feed rate combination of 80 SFM and 0.003 IPT, respectively. Figures 81, 82 and 83 show the IPF of all the phases, ferrite phase and iron carbide phase for sample 1 and 2 at failure when machining at the cutting speed and feed rate combination of 120 SFM and 0.005 IPT, respectively. Samples 1 and 2 were taken from the center and the edge of the machining cut on the workpiece, respectively.

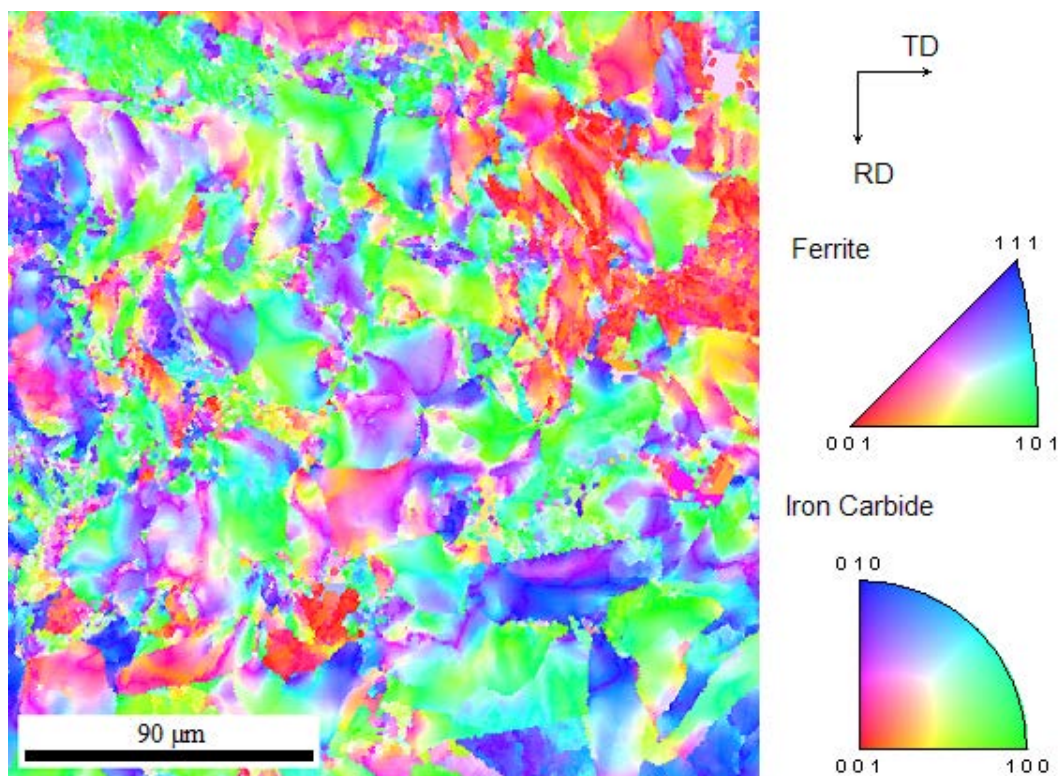


Figure 76: IPF for all phases – As received material.

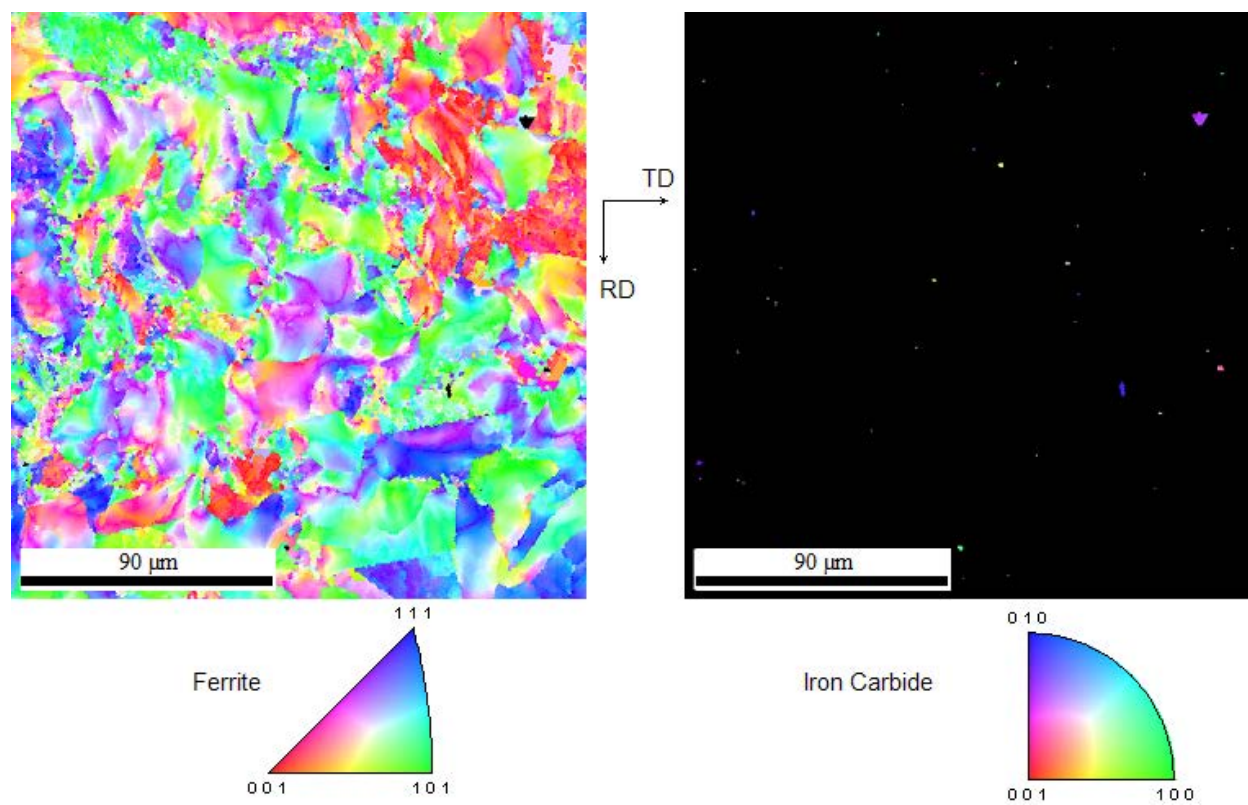


Figure 77: IPF for ferrite and iron carbide phase – As received material.

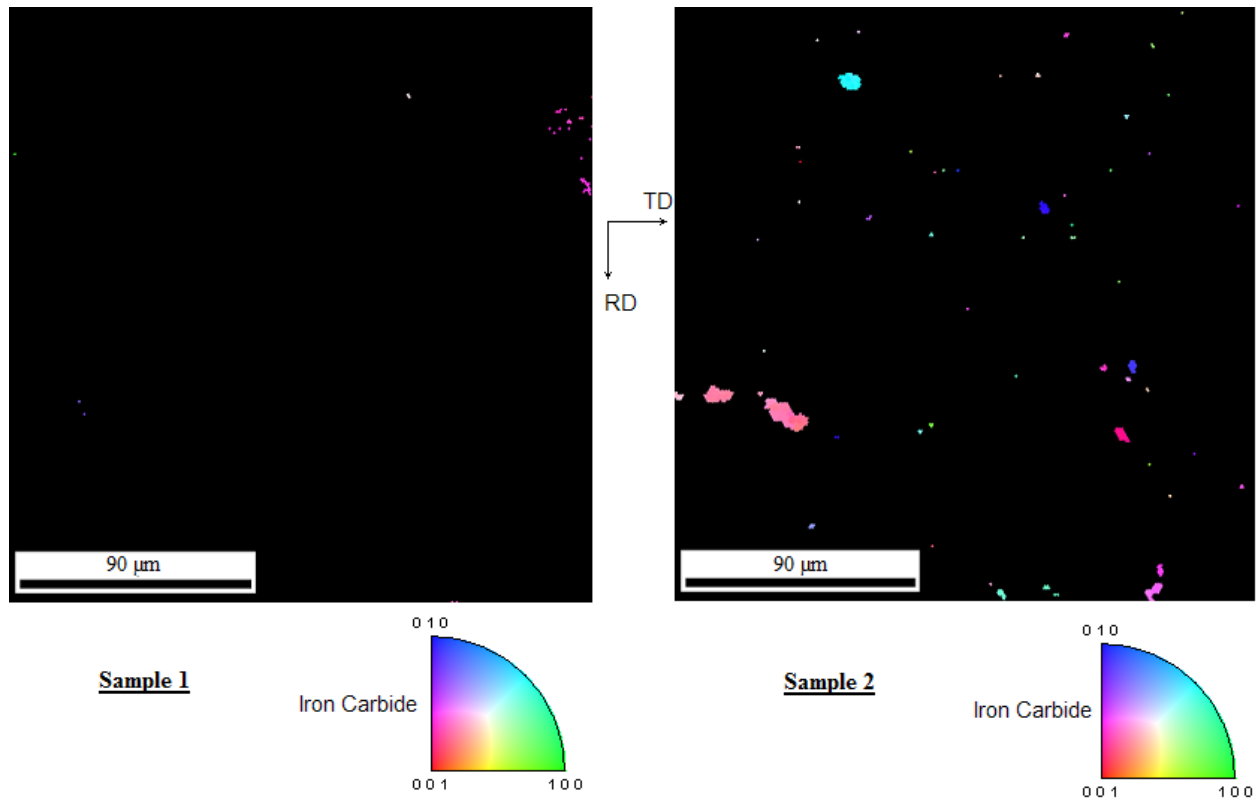


Figure 80: IPF for iron carbide phase – Sample 1 and 2 machined at 80 SFM and 0.003 IPT.

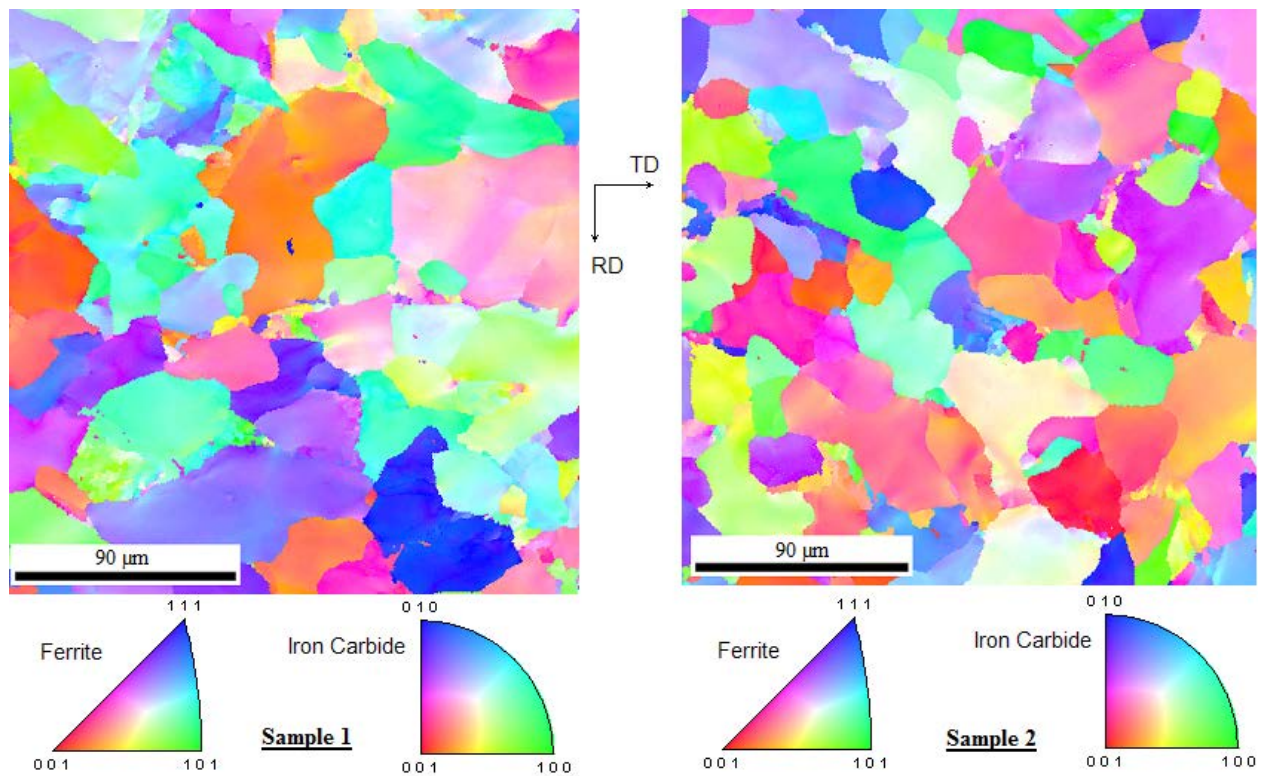


Figure 81: IPF for all phases – Sample 1 and 2 machined at 120 SFM and 0.005 IPT.

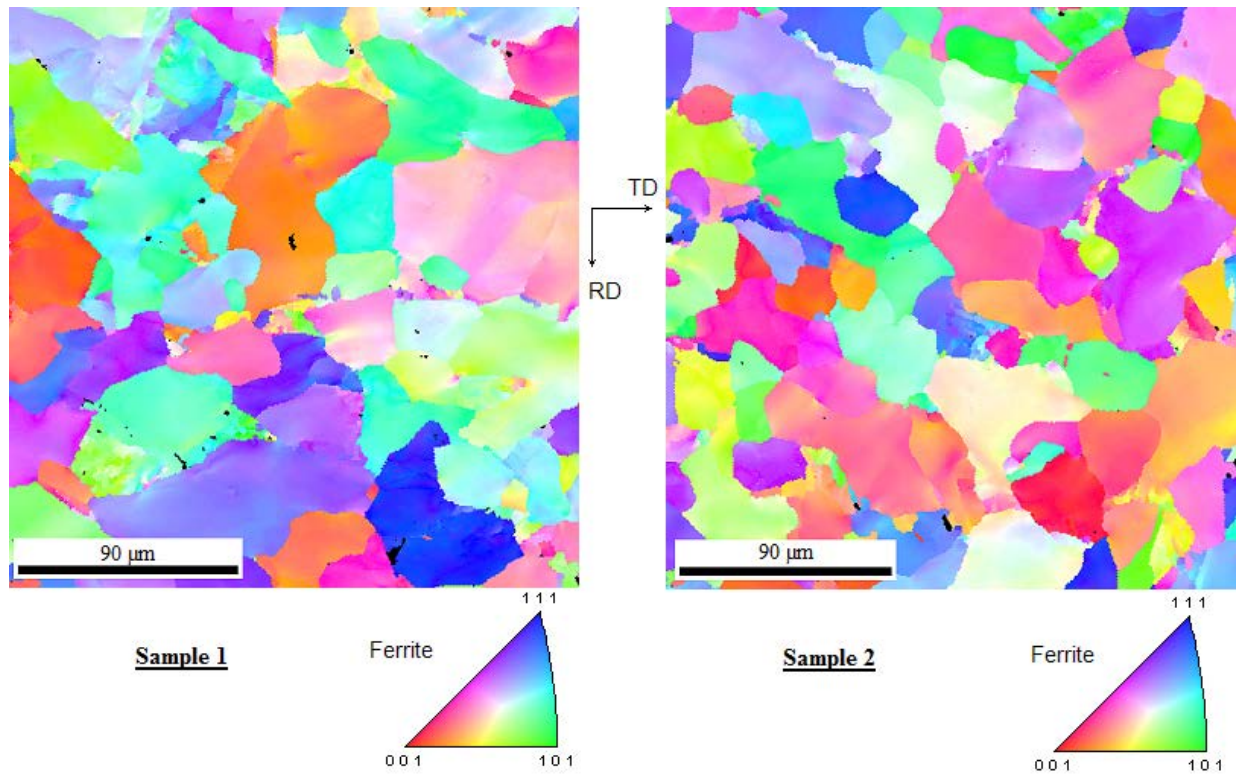


Figure 82: IPF for ferrite phase – Sample 1 and 2 machined at 120 SFM and 0.005 IPT.

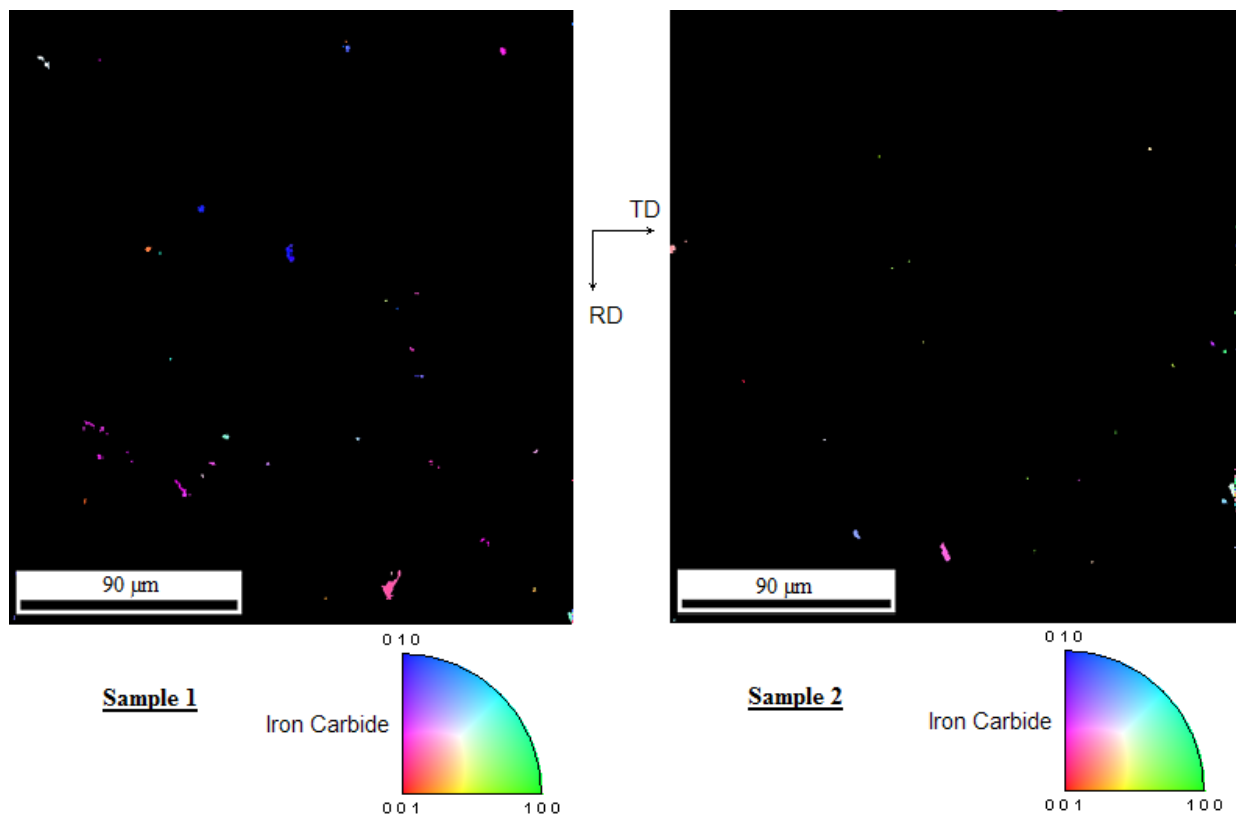


Figure 83: IPF for iron carbide phase – Sample 1 and 2 machined at 120 SFM and 0.005 IPT.

Figure 84 shows the grain size comparing between the as-received material and samples at failure after machining at 80 SFM – 0.003 IPT and 120 SFM and 0.005 IPT.

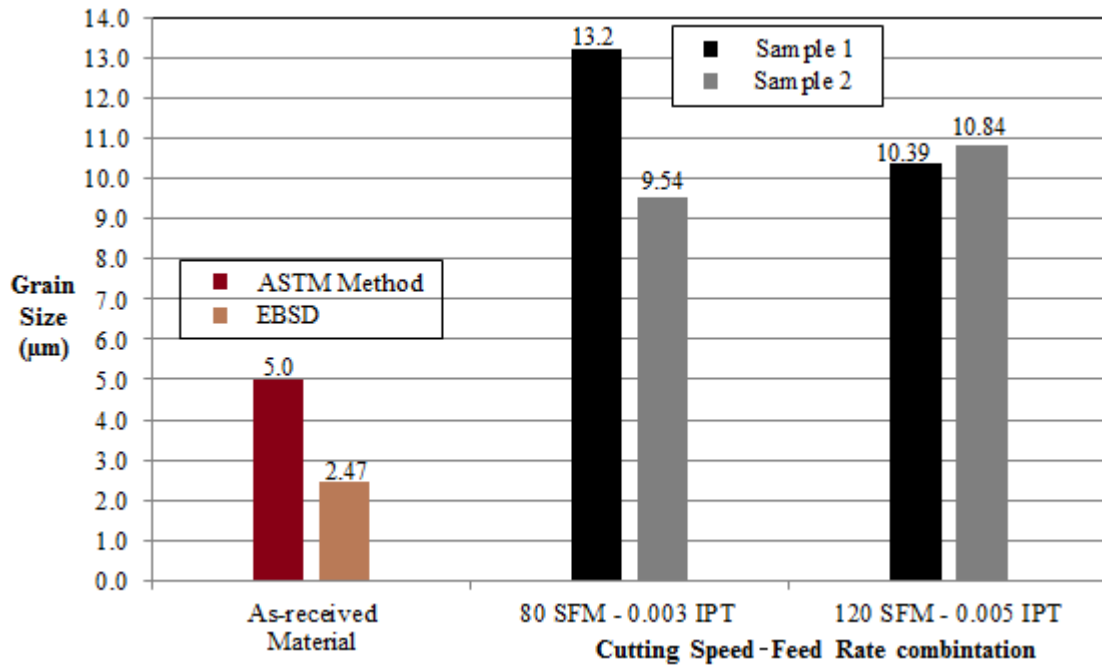


Figure 84: Grain size comparison.

The grain size for the as-received sample obtained by using the American Society for Testing and Materials (ASTM) method was 5 μm and by the EBSD was 2.47 μm. The observed grain sizes for sample 1 and 2 for the cutting speed and feed rate combination of 80 SFM and 0.003 IPT were 13.2 μm and 9.54 μm, respectively. Similarly, the observed grain sizes for sample 1 and 2 for the cutting speed and feed rate combination of 120 SFM and 0.005 IPT were 10.39 μm and 10.84 μm, respectively. The grain size distribution plot for the as-received material, sample 1 for 80 SFM – 0.003 IPT and sample 1 for 120 SFM – 0.005 IPT is shown in figures 85, 86 and 87, respectively. It was observed that there was some grain growth on the machined surface. The grain growth was about 4 to 8 μm for both the cutting combination under consideration. These grains cannot be associated with the grain growth mechanism which often occurs after recrystallization since they do not have high enough temperature/time to reach the

recrystallization temperature. Moreover, the expected tool-workpiece interface temperature during machining AISI 1018 steel is less than the recrystallization temperature under the current cutting combination of this study (Dhiman et al. 2008). But the temperature and the cutting forces are sufficient enough to impart residual stresses on the machined surface (Sadat et al. 1991; Kohler et al. 2012). These induced stresses are assumed to be the driving force for the grain boundaries motion to reduce its overall energy resulting in the slight grain growth (Cahn & Taylor, 2004; Winning et al. 2002; Winning et al. 2001; Bousfield, 1997).

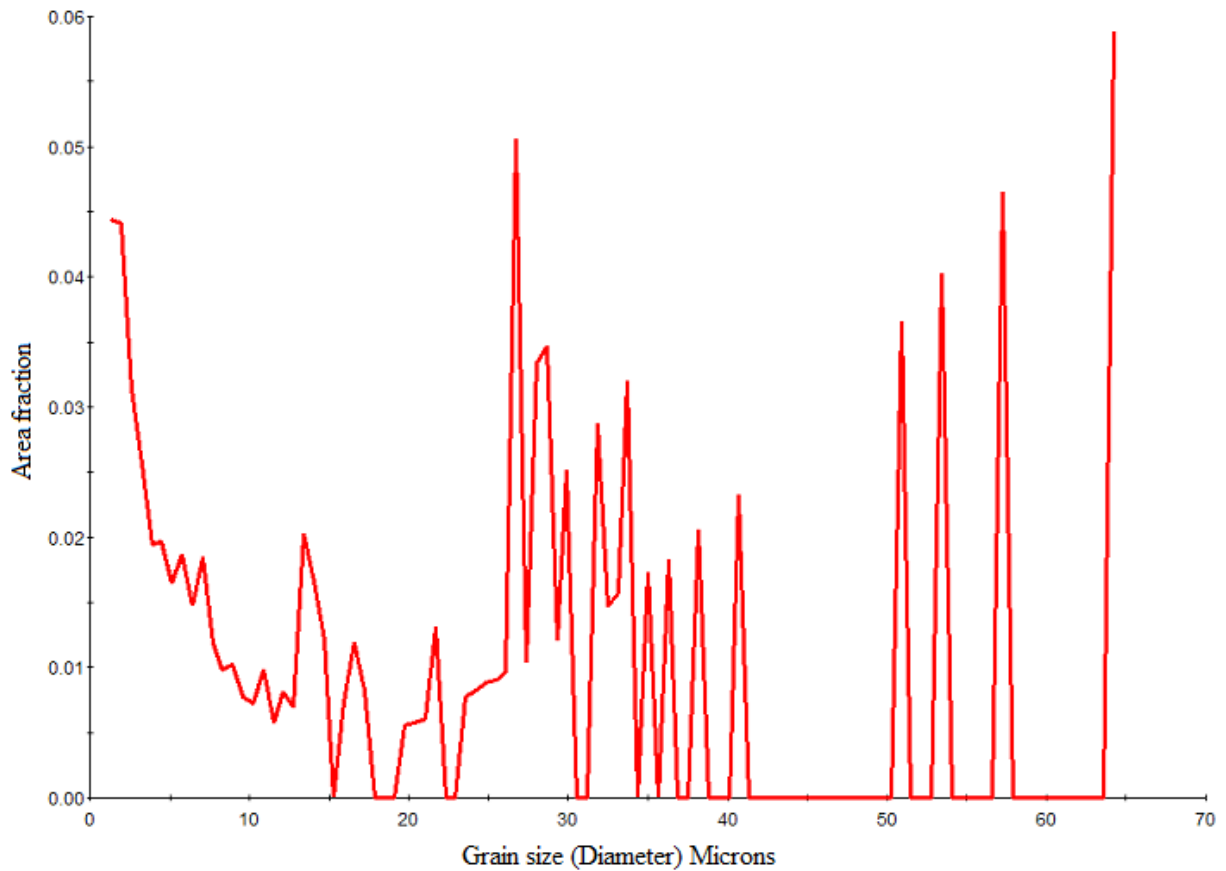


Figure 85: Grain size distribution plot – As received material

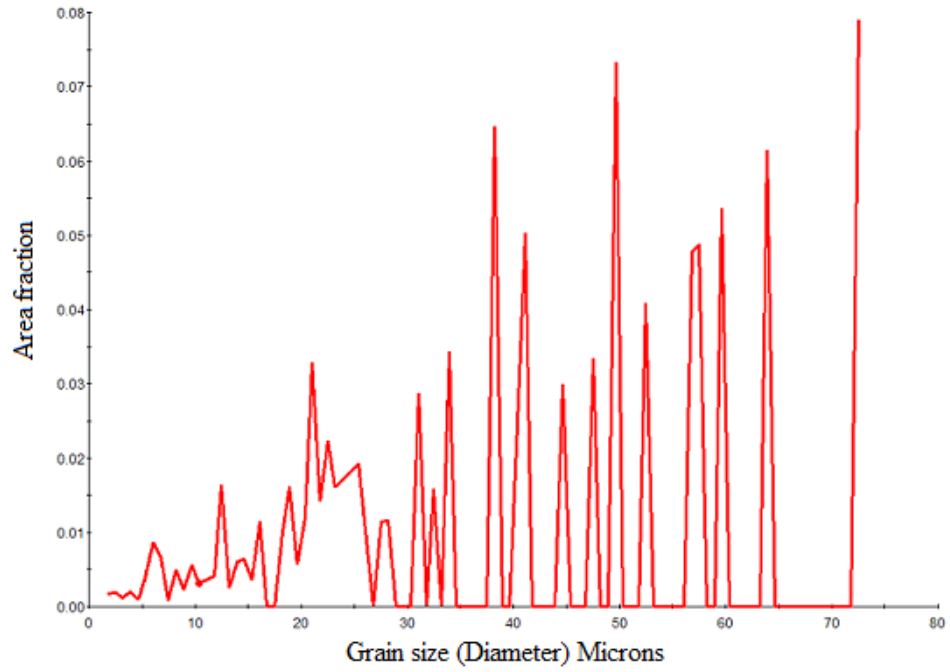


Figure 86: Grain size distribution plot for 80 SFM and 0.003 IPT – Sample 1

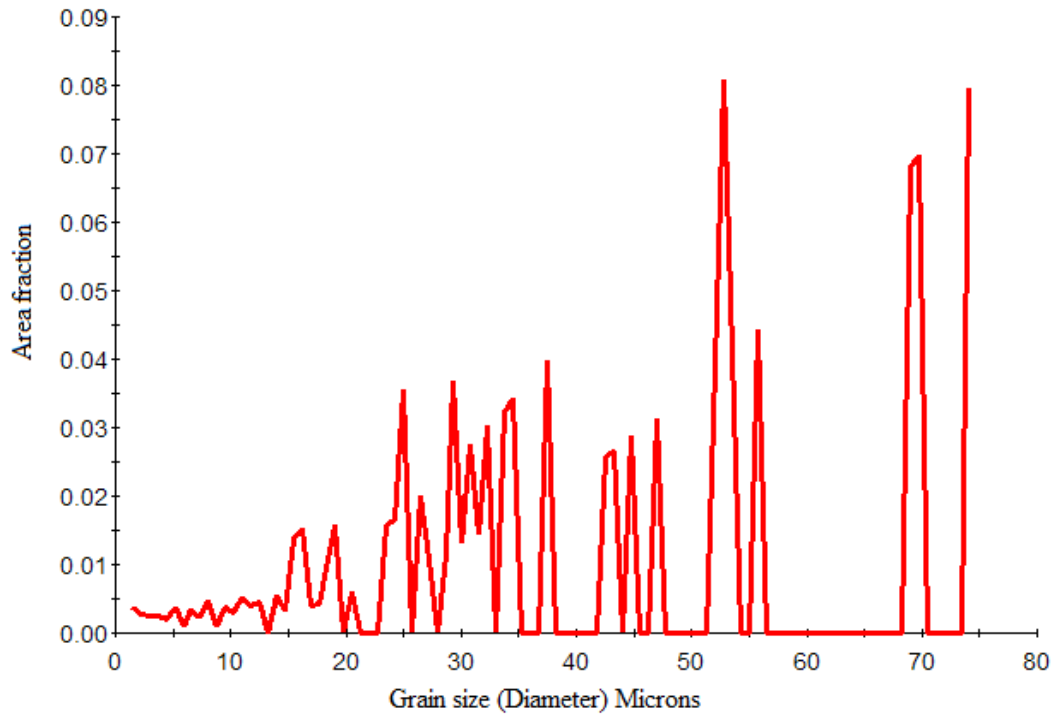


Figure 87: Grain size distribution plot for 120 SFM and 0.005 IPT – Sample 1

Also, the deformed machined surface is expected to have undergone the recovery process/stage. Dislocations become mobile due to the materials stored energy. Recovery process associated with plastic deformation is due to the annihilation of dislocations. Such annihilation can occur by the coming together of dislocation segments of opposite sign. This type of recovery process is called polygonization. In polygonization, gradual elimination of extraneous dislocations and rearrangement of remaining dislocations occur, simultaneously. The sub-grain formation is followed by sub-grain coarsening where the average grain size increases while the number of sub-grain decreases (Doherty et al. 1997). Figure 88 show the ferrite pole figure for the as-received material.

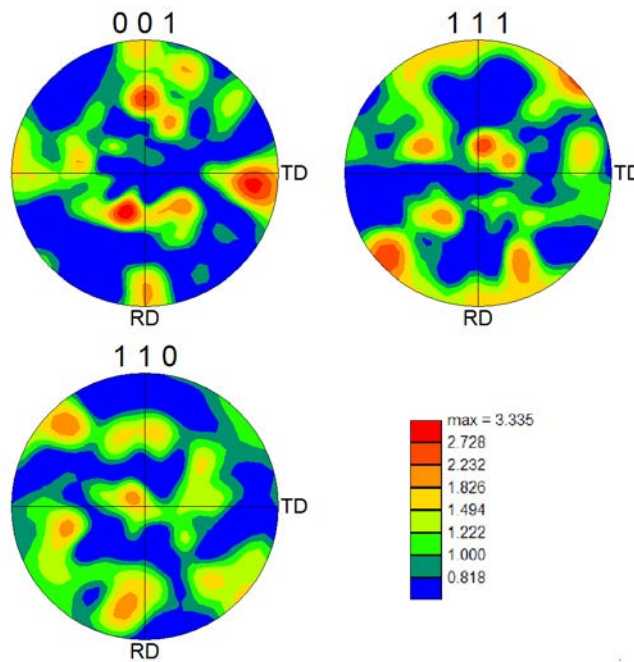


Figure 88: Ferrite pole figures – As received material.

It can be seen in figure 88, that the ferrite grains are moderately (001) textured along the transverse direction (TD), while the (110) and (111) poles show no evidence of textured grains. After machining it was observed that the ferrite maintained its c-axis texturing as seen in figure 89 and 90 for both the samples 1 and 2 at the cutting speed and feed rate combinations of (80

SFM – 0.003 IPT) and (120 SFM – 0.005 IPT), respectively. The iron carbide (Fe_3C) pole figures are not shown since the volume percent is too low to quantify texture.

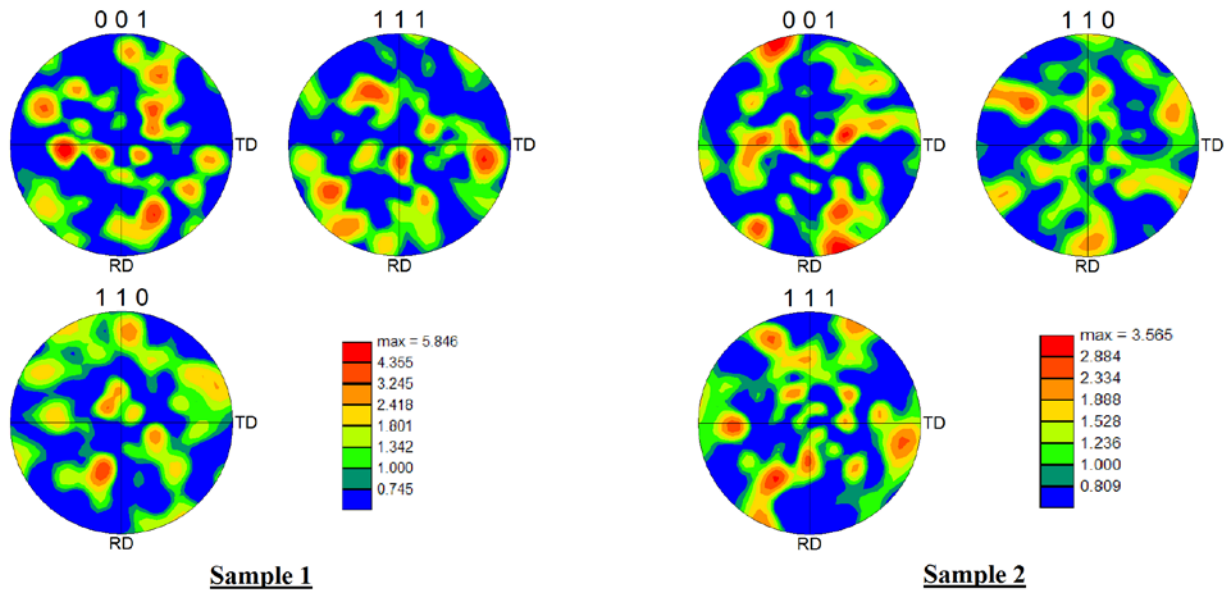


Figure 89: Ferrite pole figures – Sample 1 and 2 machined at 80 SFM and 0.003 IPT.

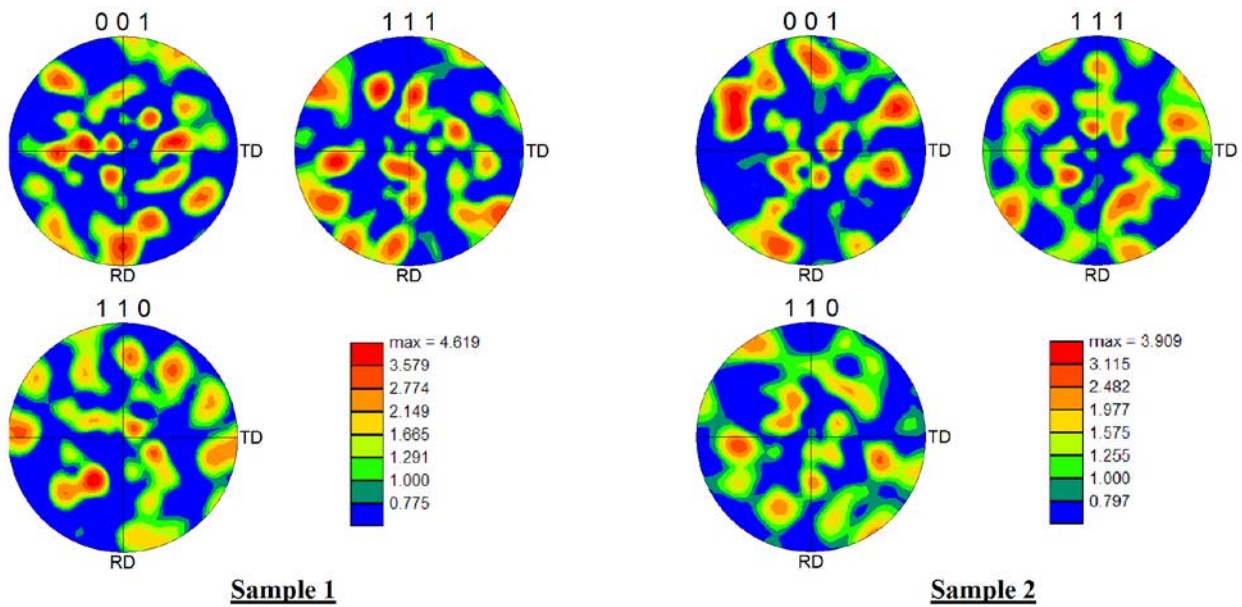


Figure 90: Ferrite pole figures – Sample 1 and 2 machined at 120 SFM and 0.005 IPT.

CHAPTER 5

SUMMARY AND CONCLUSIONS

The focus of this present study was to investigate the effects of microlubrication during end milling American Iron and Steel Institute (AISI) 1018 steel with a 1 inch solid carbide cutter under varying cutting speed and feed rate levels and a constant depth of cut using Acculube 6000 vegetable based lubricant at a constant flow rate and air pressure of 12 ml/h and 0.1 MPa, respectively. Machining experiments were carried out for a total of six combinations having cutting speeds of 80, 100 and 120 surface feed per minute (SFM) and feed rates of 0.003 and 0.005 inches per revolution (IPT). The results were based on the multivariate analysis of variance (MANOVA), parameter optimization, tool life, material removal rate (MRV), wear mechanisms, cross sectional hardness measurements, transmission electron microscopy (TEM), scanning electron microscopy (SEM) and electron backscattered diffraction (EBSD) analysis.

The MANOVA and analysis of variance (ANOVA) assumptions were found be robust. The MANOVA model indicated that the main effects for the cutting speed and the feed rate variables were significant. But, the interaction of (cutting speed*feed rate) was not significant at 95% confidence level.

The ANOVA for flank wear side 1 indicated that the cutting speed and feed rate variables main effects were statistically significant while the interaction of (speed*feed) was not statistically significant at 95% confidence level.

The ANOVA for flank wear side 2 indicated that the feed variable main effects is statistically significant while the speed variables main effect and the interaction of (speed*feed) are not statistically significant at 95% confidence level.

The ANOVA for aerosol mass concentration indicated that the feed rate variables main effects was statistically significant while the cutting speed and the interaction of (speed*feed) was not statistically significant at 95% confidence level.

The model was able to predict 69.44%, 68.06% and 42.90% of the variation in the data for both the flank wear side 1, 2 and aerosol mass concentration, respectively. An adequate signal-to-noise precision ratio of 9.54, 5.97 and 9.38 was obtained by the model for both the flank wear side 1, 2 and aerosol mass concentration, respectively, indicating adequate signal greater than 4. The model can therefore be used as a good predictor for both the flank wear sides and aerosol mass concentration.

The parameter optimization was done by setting the goal to minimize flank wear Side 1, Side 2 and aerosol mass concentration. It was observed that there was 84.2% desirability to achieve a flank wear side 1 of 0.365 mm using a cutting speed of 120 SFM and 0.003 IPT. And there was 60.7% desirability to achieve a flank wear side 2 of 0.380 mm using a cutting speed of 120 SFM and 0.0041 IPT. Also, there was 84.0% desirability to achieve a concentration of 5.91 mg/m³ using a cutting speed of 120 SFM and a feed rate of 0.005 IPT.

The highest average mass concentration of 8.32 mg/m³ was realized using treatment 80 SFM and 0.003 IPT. The lowest average mass concentration of 5.91 mg/m³ was realized using treatment 120 SFM and 0.005 IPT. Atomization was dominant at low speed and feed rate while vaporization/condensation mechanism was dominant at higher speed and feed rate combination.

Microlubrication generated low average mass concentration of aerosol for high feed rate level of 0.005 IPT as compared to low feed rate level of 0.003 IPT. On the other hand, microlubrication generated higher average particle size for lower speed rate levels as compared to higher speed rate levels. During microlubrication, the main mechanism at work might be

cooling due to evaporation of the MWF. This points out towards developing MWF which have higher latent heat of evaporation. Moreover, the aerosol concentrations during microlubrication suggest the need for the scientific assessment of the atomization properties of MWFs. The MWFs for microlubrication should be formulated in such a way that they atomize to a size range that is non-hazardous to the environment and human health. It can be concluded that though microlubrication may be effective in milling, more investigations should be carried out to lower the mass concentration of the aerosol particles to below the recommended value of 5 mg/m^3 by Occupational Safety and Health Administration (OSHA) for mineral oil mist.

The cutting performance under microlubrication is five times better in terms of tool life and two times better in terms of MRV under low cutting speed and feed rate combination (i.e. 80 SFM and 0.003 IPT) as compared to high cutting speed and feed rate combination (i.e. 120 SFM and 0.005 IPT). The highest tool life of 861 minutes was realized using treatment 80 SFM and 0.003 IPT. Due to the lower cutting speed and feed rate the mist particle produced by microlubrication easily penetrates through to the tool/workpiece interface promoting lubrication and cooling. The lowest tool life of 21 minutes was realized using treatment 100 SFM and 0.005 IPT. Due to high feed rate, the cutting fluid is unable to effectively cool and lubricate the cutting zone leading to higher temperatures and lower tool life.

All the cutting tools under consideration failed with gradual abrasive wear except for treatment 80 SFM and 0.005 IPT, which underwent a catastrophic failure due to massive tool chipping.

The treatments of (80 SFM – 0.003 IPT) and (120 SFM – 0.005 IPT) were further considered for wear mechanisms analysis, cross sectional hardness measurements, SEM and EBSD analysis. Based on SEM observation, two-body abrasion wear mode was likely dominant.

Other wear mechanisms were also active like sliding wear, adhesion and micro abrasion resulting into micro fatigue crack, welded-micro chips and workpiece plowing.

Cross sectional hardness analyses indicated that the plastic deformation due to machining extends to about 150 – 180 μm for both the treatments which was attributed to the increase in dislocation density at the machined surface.

The surface profile of the workpiece suggested that for treatment 120 SFM and 0.005 IPT, 11% of the depth population (i.e. density of the distribution of the depth data points in the profile) was in between 7.35 μm and 7.92 μm and for treatment 80 SFM and 0.003 IPT, 15% of the depth population is in between 4.31 μm and 4.79 μm . The bearing area curve suggested that for treatment 120 SFM and 0.005 IPT, almost 50% of the points have a depth that lies between 0 and 6.79 μm and for treatment 80 SFM and 0.003 IPT, almost 60% of the points have a depth that lies between 0 and 4.79 μm . The R_q value for treatment 120 SFM and 0.005 IPT and treatment 80 SFM and 0.003 IPT was 2.2 and 1.18 μm , respectively.

Cross sectional TEM analysis at failure was carried out for the cutting speed and feed rate level of 120 SFM and 0.005 IPT to investigate the workpiece subsurface deformation and strengthening. High concentration of dislocations were observed with an average dislocation density (ρ) of $1.5 \times 10^9 / \text{m}^2$ for the sample taken at around 20 μm from machined edge, the results were in accordance with cross sectional hardness measurements which showed high hardness values near the surface and decreased hardness values while moving towards the bulk.

EBSD analysis showed a slight increase in grain size from the bulk for the both the treatments. This was not due to the recrystallization process but due to the induced residual stresses resulting in grain boundary motion. It was also observed that the ferrite maintained its texture for both the treatments after machining.

Recommendation for Future Work

Future research for mist and microstructural analyses which can be done as an extension to this study using the same material, process and parameters are:

- 1) Investigating the tool-workpiece interface temperature
- 2) Investigating the cutting forces generated during machining
- 3) Conducting a comparative study using dry, minimum quantity lubrication (MQL) and flood coolant
- 4) Conducting a comparative study using different MQL flow rates
- 5) Conducting a comparative study using coated and uncoated tools
- 6) Investigating the effects of different vegetable oils
- 7) Conducting a surface roughness analysis

REFERENCES

- ACGIH. (2001). Documentation of the threshold limits values and biological exposure indices. Sixth Edition, Cincinnati, *American Conference of Governmental Industrial Hygienist*.
- Adler, D. P., Hii, W. W. S., Michalek, D. J., & Sutherland, J. W. (2006). Examining the role of cutting fluid in machining and efforts to address associated environmental/health concerns. *Machining Science and Technology*, 10, 23-58.
- American Society for Metals (ASM). (1990). *Metals Handbook: Volume 1 – Properties and Selection: Irons, Steels, and High-Performance Alloys*, ASM International, Metals Park, OH.
- Attanasio, A., Gelfi, M., Giardini, C., & Remino, C. (2006). Minimum quantity lubrication in turning. *Wear*, 260, 333-338.
- Bennett, E. O., & Bennett, D. L. (1985). Occupational airways diseases in the metal working industries. *Tribology International*, 18 (3), 169-176.
- Bhowmick, S., & Alpas, A. T. (2008). Minimum quantity lubrication drilling of aluminum-silicon alloys in water using diamond-like carbon coated drills. *International Journal of Machine Tools & Manufacture*, 48, 1429-1443.
- Boubekri, N., & Shaikh, V. (2012). Machining using minimum quantity lubrication: A technology for sustainability. *International Journal of Applied Science and Technology*, 2, 111-115.
- Bousfield, B. (1997). The metallography of deformation by material removal. *Praktische metallographie*, 43 (1), 2-22.
- Bray, J. H., & Maxwell, S. E. (1985). *Multivariate Analysis of Variance: Quantitative applications in the social sciences, Second Edition*, Sage Publications, Beverly Hills, CA.
- Brockhoff, T., & Walter, A. (1998). Fluid minimization in cutting and grinding, *Abrasives*, October-November, 38-92.
- Cahn, J. W., & Taylor, J. E. (2004). A unified approach to motion of grain boundaries, relative tangential translation along grain boundaries, and grain rotation. *Acta Materialia*, 52, 4887-4898.
- Callister, W. D. Jr. (2007). *Materials science and engineering: An introduction, Seventh Edition*, John and Wiley and Sons, New York City, NY.
- Chakraborty, P. (2008). Tool life and flank wear modeling of physical vapour deposited TiAlN/TiN multilayer coated carbide end Mill inserts when machining 4340 steel under dry and semi-dry cutting conditions. *University of Miami Scholarly Repository*, Retrieved

from http://scholarlyrepository.miami.edu/cgi/viewcontent.cgi?article=1021&context=oa_dissertations

- Chalmers, R. E. (1999). Global flavor highlights NAMRC XXVII. *Manufacturing Engineering*, 123 (1), 80-86.
- Childs, T. H.C., Maekawa, K., Obikawa, T., & Yamane, Y. (2000). *Metal Machining - Theory and Applications*, Butterworth-Heinemann, Oxford, UK.
- Clarens, A. F., Zimmerman, J. B., Keoleian, G. A., Hayes, K. F., & Skerlos, S. J. (2008). Comparison of life cycle emissions and energy consumption for environmentally adapted metalworking fluid systems. *Environmental Science and Technology*, 42 (22), 8534-8540.
- Costa, E. S., Da Silva, M. B., & Machado, A. R. (2009). Burr produced on the drilling process as a function of tool wear and lubricant coolant conditions. *Journal of the Brazilian Society of Mechanical Science & Engineering*, XXXI (1), 57-63.
- Da Silva, R. B., Vieira, J. M., Cardoso, R. N., Carvalho, H. C., Costa, E. S., Machado, A. R., & De Ávila, R. F. (2011). Tool wear analysis in milling of medium carbon steel with coated cemented carbide inserts using different machining lubrication/cooling systems. *Wear*, 271, 2459-2465.
- Davis, J. R., (1989). *Metals Handbook: Volume 16 – Machining*, ASM International, Metals Park, OH.
- Dhar, N. R., Ahmed, M. T., & Islam, S. (2006). An experimental investigation on effect of minimum quantity lubrication in machining AISI 1040 steel. *International Journal of Machine Tools and Manufacture*, 47, 748-753.
- Dhiman, S., Sehgal, R., Sharma, S. K., & Sharma, V. S. (2008). Machining behavior of AISI 1018 steel during turning. *Journal of Scientific & Industrial Research*, 67, 355-360.
- Doherty, R. D., Hughes, D. A., Humphreys, F. J., Jonas, J. J., Jensen, D. J., Kassner, M. E., King, W. E., McNelley, T. R., McQueen, H. J., Rollett, A. D., (1997). Current issues in recrystallization: A review. *Materials Science & Engineering A*, A238 (2), 219-274.
- Dosbaeva, J., Fox-Rabinovich, G., Dasch, J., & Veldhuis, S. (2008). Enhancement of wet and MQL based machining of automotive alloys using cutting tools with DLC/Polymer surface treatments. *Journal of Materials Engineering and Performance*, 17 (3), 346-351.
- Filipovic, A., & Stephenson, D. A. (2006). Minimum quantity lubrication (MQL) applications in automotive power-train machining. *Machining Science and Technology*, 10, 3-22.
- Greaves, I. A., Eisen, E. A., Smith, T. J., Pothier, L. J., Kriebel, D., Woskie, S. R., Kennedy, S. M., Shalat, S., & Monson, R. R., (1997). Respiratory health of automobile workers

- exposed to metal-working fluid aerosols: respiratory symptoms. *American Journal of Industrial Medicine*, 32, 450-459.
- Guhring Inc. (2012, September). *Tool list*. Retrieved from <http://www.guhring.com/Documents/Catalog/Tools/3146.pdf>
- Hand, D. J., & Taylor, C. C. (1987). *Multivariate Analysis of Variance and repeated measures: A practical approach for behavioural scientist*, Chapman and Hall Publishers, New York City, NY.
- Hassan, A., & Yao, Z. (2005). Optimization of cutting parameters for face milling titanium alloy using MQL. *Journal of Donghua University*, 22 (2), 9-12.
- Heisel, U., Schaal, M., & Wolf, G. (2009). Burr formation in milling with minimum quantity lubrication. *Production Engineering. Research and Development*, 3, 23-30.
- Huynh, C. K. (2009). Occupational exposure to mineral oil metalworking fluid (MWFs) mist: Development of new methodologies for mist sampling and analysis. Results from an Inter-laboratory Comparison. *Journal of Physics: Conference Series*, 151, 1-14.
- Iqbal, A., Dar, N. U., He, N., Khan, I., & Li, L. (2008). Optimizing cutting parameter in minimum quantity of lubrication milling of hardened cold work tool steel. *Proceedings of the Institution of Mechanical Engineers, Part B, Journal of Engineering Manufacture*, 223 (1), 43-54.
- Iqbal, A., He, N., Khan, I., Liang, L., & Dar, N. U. (2008). Modeling the effects of cutting parameters in MQL employed finish hard milling process using D-optimal method. *Journal of Materials Processing Technology*, 199, 379-390.
- ITW Rocol North America. (September 2012). *Acculube 6000 - Materials Safety Data Sheet*. Retrieved from <http://www.itwfpg.com/TDS/acculube/lb6000.pdf>
- Jayal, A. D., & Balaji, A. K. (2009). Effects of cutting fluid application on tool wear in machining: Interactions with tool-coatings and tool surface features. *Wear*, 267, 1723-1730.
- Jayal, A. D., Balaji, A. K., & Seseek, R. (2004). Environmentally conscious machining of a cast aluminum alloys: Investigation of cutting fluid effects in drilling. *Transaction of NAMRI/SME*, 32, 415-422.
- Jayal, A. D., Umbrello, D., Dillon, O. W., & Jawahir, I. S. (2010). An investigation of the effects of cutting conditions, tool edge geometry, and workpiece hardness on surface integrity in orthogonal machining of AISI 52100 steel. *Transaction of NAMRI/SME*, 38, 57-64.
- Kalpakjian, S. (1995). *Manufacturing Engineering and Technology, Third Edition*, Addison-Wesley Publishing Company, Boston, MA.

- Kang, M. C., Kim, K. H., Shin, S. H., Jang, S. H., Park, J. H., & Kim, C. (2008). Effect of the minimum quantity lubrication in high-speed end-milling of AISI D2 cold worked die steel (62 HRC) by coated carbide tools. *Surface & Coatings Technology*, 202, 5621-5624.
- Khan, M. M. A., & Dhar, N. R. (2006). Performance evaluation of minimum quantity lubrication by vegetable oil in terms of cutting force, cutting zone temperature, tool wear, job dimension and surface finish in turning AISI-1060 steel. *Journal of Zhejiang University, Science A*, 7 (11), 1790-1799.
- Khan, M. M. A., Mithu, M. A. H., & Dhar, N. R. (2009). Effects of minimum quantity lubrication on turning AISI 9310 alloy steel using vegetable oil-based cutting fluid. *Journal of Materials Processing Technology*, 209, 5573-5583.
- Khodabakhshi, F., & Kazeminezhad, M. (2011). The effects of constrained groove pressing on grain size, dislocation density and electrical resistivity of low carbon steel. *Materials and Design*, 32, 3280-3285.
- Köhler, J., Grove, T., Mai, O., & Denkena, B. (2012). Residual stresses in milled titanium parts. *Procedia CIRP*, 2, 79-82.
- Kurgin, S., Barber, G., & Zou, Q. (2011). Cutting insert and work piece materials for minimum quantity lubrication. *Proceedings of the SPIE - The International Society for Optical Engineering, Fourth International Seminar on Modern Cutting and Measurement Engineering*, 7997, 1-10.
- Kwon, P. (2000). Predictive models for flank wear on coated inserts, *Transaction of ASME*, 122, 340-347.
- Lee, W., & Lam, H. (1996). The deformation behaviour and microstructure evolution of high-strength alloy steel at high rate of strain. *Journal of Materials Processing Technology*, 57, 233-240.
- Liao, Y. (February 2013). Foil thickness measurement. *Practical electron microscopy and database*. Retrieved from <http://www.globalsino.com/EM/page4832.html>
- Meyveci, A., Karacan, I., Hanifi, F. E., Cahgulu, U., & Durmus, H. (2011). A study of wear and aged aluminum alloys 2XXX and 6XXX within the MANOVA statistical analysis. *Metal Science and Heat Treatment*, 53 (3-4), 173-175.
- Min, S., Inasaki, I., Fujimura, S., Wakabayashi, T & Suda, S. (2005). Investigation of adsorption behaviour of lubricants in near-dry machining. *Proceedings of the Institution of Mechanical Engineers, Part B: Journal of Engineering Manufacture*, 219, 665-671.
- Mohandesi, A. J., Rafiee, M. A., Maffi, O., & Saffarzadeh, P. (2007). Dependence of the yield and fatigue strength of the thread rolled milled steel on dislocation density. *Transaction of ASME*, 129, 216-222.

- Murakami, Y., & Yamamoto, T. (2007). Ecological deep hole drilling by novel coated and designed drill. *Key Engineering Materials*, 329, 657-662.
- Northcott, W. H. (1868). *A treatise on lathes and turning, simple, mechanical and ornamental*. Longmans Green and Company, London, UK.
- Olson, C. L. (1974). Comparative robustness of six tests in multivariate analysis of variance. *Journal of the American Statistical Association*, 69, 894-908.
- Oxford Instruments. (March 2013). *Electron Backscattered Diffraction*. Retrieved from www.ebsd.com
- Park, D. (2012). The occupational exposure limit for fluid aerosol generated in metalworking operations: Limitations and recommendations. *Safety and Health at Work*, 3, 1-10.
- Rahman, M., Senthil, K. A., & Salam, M. U. (2002). Experimental evaluation on the effect of minimal quantities of lubricant in milling, *International Journal of Machine Tools & Manufacture*, 42, 539-547.
- Roy, A. K., Bandyopadhyay, S., Suresh, S. B., Maitra, D., Kumara, P., Wells, D., & Mac, L. (2006). Relationship of residual stress to dislocation density in cold-worked martensitic alloy, *Materials Science and Engineering A*, 416, 134-138.
- Ryu, S. H., Choi, D. K., & Chong, N. C., (2006). Roughness and texture generation on end milled surface, *International Journal of Machine Tools & manufacture*, 46, 404-412.
- Ryufuku, S., Tomota, Y., Shiota, Y., Shiratori, T., Suzuki, H., & Moriai, A. (2007). Neutron diffraction profile analysis to determine dislocation density and grain size for drawn steel wires. *Materials Science Forum – Trans Tech Publications*, 539, 2281-2286.
- Sadat, A. B., Reddy, M. Y., & Wang, B. P. (1991). Plastic deformation analysis in machining of Inconel-718 nickel-base superalloy using both experimental and numerical methods. *Int. J. Mech. Sci.*, 33 (10), 829-842.
- Sandvik Coromant. (2007). Application guide: Milling methods, 2D component features, complete process solutions. *AB Sandvikens Tryckeri*, Sweden. Page: 29.
- Sanz, C., Fuentes, E., Gonzalo, O., Bengoetxea, I., Obermair, F., & Eidenhammer, M. (2008). Advances in the ecological machining of magnesium and magnesium based hybrid parts. *International Journal of Machining and Machinability of Materials*, 4 (4), 302-319.
- Shaikh, V., & Boubekri, N. (2010). Effects of minimum quantity lubrication in drilling 1018 steel, *Journal of Manufacturing Technology Research*, 2 (1/2), 1-14.

- Sharif, S., Hisyam, M. A., & Kurniawan, D. (2009). Performance evaluation of vegetable oil as an alternative cutting lubricant when end milling stainless steel using TiAlN coated carbide tools. *Transactions of NAMRI/SME*, 37, 9-14.
- Shaw, M., Pigott, J., & Richardson, L. (1951). The effect of cutting fluid upon chip-tool interface temperature. *Transaction of ASME*, 73, 45-56.
- Sheehan, M. J. (1999). Final report of the OSHA metalworking fluids standard advisory committee. *OSHA Publications*, 1-193.
- Shimadzu. (August 2012). *Shimadzu Dynamic Ultra Micro Hardness Tester DUH-211/211S*. Retrieved from http://www.shimadzu.eu/brochure/DUH-211_211S.pdf
- Sreejith, P. S., & Ngoi, B. K. A. (2000). Dry machining: machining of the future. *Journal of Materials Processing Technology*, 101, 287-291.
- Stachowiak, G. W., & Batchelor, A. W. (2005). Engineering Tribology, Third Edition, *Elsevier Inc*, Oxford, UK.
- Sternberk, J., Kratochvilova, E., Gemperle, A., Faja, V., & Walder, V., (1985). Dependence of characteristics of hysteresis loops on dislocation densities for low-alloy Cr-Mo steel. *Czechoslovak Journal of Physics*, 35 (11), 1259-1266.
- Su, Y., He, N., Li, L., & Li, X. (2006). An experimental investigation of effects of cooling/lubrication conditions on tool wear in high-speed end milling of Ti-6Al-4V. *Wear*, 261 (7-80), 760-766.
- Sutherland, J. W., Kulur, V. N., & King, N. C. (2000). An experimental investigation of air quality in wet and dry turning. *Annals of the CIRP*, 49 (1), 61-64.
- Taylor, F. W. (1906). *On the art of cutting metals*. The American Society of Mechanical Engineers, New York City, NY.
- Taylor, G. I., (1934). The mechanism of plastic deformation of crystals. Part 1. *Theoretical. Proceedings of the Royal Society of London. Series A*. 145 (855), 362-387.
- Thermo Scientific. (September 2012), *Particulate Monitor DataRam4*, Retrieved from http://www.thermoscientific.com/ecom/servlet/productsdetail_11152_L10955_89583_11961406_-1
- U.S. Department of Health and Human Services. (1998). Occupational exposure to metal working fluid. *NIOSH Publication*, 98-102.
- Vorobev, G. M., & Krivisha, L. V. (1971). X-Ray diffraction measurement of dislocation density in transformer steel. *Industrial Tribology*, 37 (9), 1392-1395.

- Wakabayashi, T., Inasaki, I., & Suda, S. (2006). Tribological action and optimal performance: Research activities regarding MQL machining fluids, *Machining Science and Technology*, 10, 59-85.
- Weinert, K., Inasaki, I., Sutherland, J.W., & Wakabayashi, T. (2004). Dry machining and minimum quantity lubrication. *CIRP Ann. Manuf. Technol.* 53, 511-537.
- William, D. B., & Carter, C. B. (2009). *Transmission electron microscopy – A textbook for materials science*, Springer, New York City, NY.
- Winning, M., Gottstein, G., & Shvindlerman, L. S. (2002). On the mechanisms of grain boundary migration. *Acta Materialia*, 50, 353-363.
- Winning, M., Gottstein, G., & Shvindlerman, L. S. (2001). Stress induced grain boundary motion. *Acta Materialia*, 49, 211-219.
- Yan, L. T., Yuan, S. M., & Liu, Q. (2009). Effect of cutting parameters on minimum quantity lubrication machining of high strength steel. *Trans Tech Publications, Materials Science Forum*, 626-627, 387-392.
- Yeagashi, Koh. (2007). Dependence of magnetic susceptibility on dislocation density in tensile deformed Iron and Mn-steel. *ISIJ International*, 47 (2), 327-332.
- Yanda, H., Ghani, J. A., Rodzi, M. N. A. M., Othman, K., & Haron, C. H. C. (2010). Optimization of materials removal rate, surface roughness and tool life on conventional dry turning of FCD 700. *International Journal of Mechanical and Materials Engineering (IJMME)*, 5 (2), 182-190.
- Yin, F., Hanamura, T., Umezawa, O., & Nagai, K. (2003). Phosphorus-induced dislocation structure variation in the warm rolled ultrafine-grained low-carbon steels. *Materials Science and Engineering A*, 354, 31-39.
- Zhang, S., Li, J. F., & Wang, Y.W. (2012). Tool life and cutting forces in end milling Inconel 718 under dry and minimum quantity cooling lubrication cutting conditions. *Journal of Cleaner Production*, 32, 81-87.
- Zhao, W., He, N., & Li. L. (2007). High speed milling of Ti6Al4V alloy with minimal quantity lubrication. *Key Engineering Materials*, 329, 663-668.